University of Alberta

Towards magnetic resonance imaging guided radiation therapy (MRIgRT)

by

Teodor Marius Stanescu 

A thesis submitted to the Faculty of Graduate Studies and Research in partial Fulfilment of the requirement for the degree of Doctor of Philosophy

in

Medical Physics

Department of Physics

Edmonton, Alberta

Spring 2008

Your file Votre référence
ISBN: 978-0-494-45608-8
Our file Notre référence
ISBN: 978-0-494-45608-8

ABSTRACT

The goal of this work is to address key aspects of the magnetic resonance imaging guided radiation therapy (MRIgRT) process of cancer sites. MRIgRT is implemented by using a system comprised of a magnetic resonance imaging (MRI) scanner coupled with a radiation source, in our case a radiotherapy accelerator (Linac). The potential benefits of MRIgRT are the real-time tracking of the tumor and neighbouring healthy anatomy during treatment irradiation leading to on-line treatment plan optimization. Ultimately, this results in an increased accuracy and efficiency of the overall treatment process. A large research effort is conducted at Cross Cancer Institute to develop a hybrid MRI-Linac system consisting of a bi-planar 0.2 T permanent magnet coupled with a 6 MV Linac. The present work is part of this project and aims to address the following key components: a) magnetic shielding and dosimetric effects of the MRI-Linac system, b) measure and correction of scanner-related MR image distortions, and c) MRI-based treatment planning procedure for intracranial lesions. The first two components are essential for the optimal construction and operation of the MRI-Linac system while the third one represents a direct application of the system. The linac passive shielding was achieved by a) adding two 10 cm thick steel (1020) plates placed at a distance of 10 cm from the structure on opposite sides of the magnet and b) a box lined with a 1 mm MuMetal™ wall surrounding the Linac. For our proposed MRI-Linac configuration (i.e. 0.2 T field and rotating bi-planar geometry) the maximum dose difference from zero magnetic field case was found to be within 6 % and 12% in a water and water-lung-water phantom, respectively. We developed an image system distortion correction method for MRI that relies on adaptive thresholding and an iterative algorithm to determine the 3D distortion field. Applying this technique the residual image distortions were reduced to within the voxel resolution of the raw imaging data. We investigated a procedure for the MRI Simulation of brain lesions which consists of a) correction of MR images for 3D distortions, b) automatic segmentation of head sub-structures (i.e. scalp, bone, and brain) relevant for dosimetric

calculations, c) conversion of MRI datasets into CT-like images by assigning bulk CT values to head sub-structures and MRI-based dose calculations, and d) RT plan evaluation based on isodose distributions, dosimetric parameters, dose volume histograms, and an RT ranking tool. The proposed MRI-based treatment planning procedure performed similarly to the standard clinical technique, which relies on both CT and MR imaging modalities, and is suitable for the radiotherapy of brain cancer.

To Lumi

TABLES OF CONTENTS

CHAPTER 4.

DOSIMETRIC CALCULATIONS AND MAGNETIC SHIELDING CONSIDERATIONS FOR AN MRI-LINAC SYSTEM 115

LIST OF TABLES

LIST OF FIGURES

LIST OF SYMBOLS

α	Radiosensitivity
$\hat{\alpha}$	Generalized radiosensitivity
B	Boltzmann factor
$\vec{B}$	Magnetic field density vector
C_+, C_-	Relative proportions of $\|\alpha\rangle$ and $\|\beta\rangle$ states
χ	Magnetic susceptibility
D	Dose
D_i	Dose fractions
δx, δy, δz	Distortion values along the x, y and z axes
δr	Total distortion
e	Unit charge
E	Electric field
E_0	Energy eigenvalue
ξ	Interaction energy - magnetic field
γ	Gyromagnetic ratio
G_x, G_y, G_z	Field gradients applied along the x, y and z axes
h	Planck's quantum constant
H	Hamiltonian
$\vec{H}$	Magnetic field vector
$\vec{i}$, $\vec{j}$, $\vec{k}$	Unit vectors along the x, y and z axes
$\vec{i}_\rho, \vec{j}_\rho, \vec{k}_\rho$	Unit vectors along the main axes in the rotating frame
$\vec{J}$	Nuclear spin angular momentum

k_B	Boltzmann constant
$\vec{\mu}$	Nuclear magnetic moment vector
μ	Magnetic permeability
V_m	Magnetic potential
m	Magnetic quantum number
M	Magnetization
$\vec{n}$	Normal vector
N_o	Initial number of clonogens
ω_0	Larmor frequency
ω_i	Energy eigenvalues
$\overline{P}$	Ensemble average probability
ψ	Energy eigenstate
s	Spin quantum number
SF_2	Survival fraction at 2 Gy
t	Time
T1	Longitudinal relaxation
T2	Transverse relaxation
V	Volume
V_i	Tumor sub-volume
x, y, z	Cartesian coordinates

LIST OF ABREVIATIONS

1D	One dimensional
2D	Two dimensional
3D	Three dimensional
ART	Adaptive radiation therapy
BC	Boundary condition
CBCT	Cone-beam computed tomography
CCI	Cross Cancer Institute
CNS	Central nervous system
CPU	Central processing unit
CSF	Cerebro-spinal fluid
CT	Computed Tomography
CTV	Clinical target volume
DICOM	Digital Imaging and Communications in Medicine
DRR	Digitally reconstructed radiograph
DVH	Dose volume histogram
EPI	Echo planar imaging
ERE	Electron return effect
FEM	Finite element method
FC	Fixed cylindrical geometry for an MRI-Linac system
fMRI	Functional magnetic resonance imaging
FOV	Field of view
G	Gauss
GE	Gradient echo
GBM	Glioblastoma multiforme

GHz	Giga hertz
GUI	Graphical user interface
Gy	Gray
HU	Hounsfield unit
ICRP	International Commission on Radiological Protection
ICRU	International Commission on Radiation Units and Measurement
IGRT	Image guided radiotherapy
IMRT	Intensity modulated radiation therapy
IR	Inversion recovery
kV	Kilovoltage
Linac	Linear accelerator
LQ	Linear quadratic
MLC	Multi-leaf collimator
MPI	Message Passing Interface
MR	Magnetic resonance
MRI	Magnetic Resonance Imaging
MRIgRT	Magnetic resonance imaging guided radiation therapy
MV	Megavoltage
MVCT	Megavoltage computed tomography
N3	Nonparametric Nonuniform Normalization
NIST	National Institute of Standards and Technology
NMR	Nuclear magnetic resonance
PDE	Partial differential equation
PIV	Portal image verification
ppm	Parts per million
PTV	Planning target volume

RBP	Rotating bi-planar geometry for an MRI-Linac system
RF	Radiofrequency
ROI	Region of interest
RT	radiation therapy
RTP	Radiation treatment planning
SE	Spin echo
SDD	Source to detector distance
SNR	Signal-to-noise ratio
SUSAN	Smallest univalue segment assimilating nucleus
T	Tesla
TCP	Tumor control probability
TE	Echo time
TFE	Turbo fast echo
TPS	Treatment planning system
TR	Repetition time
TSE	Turbo spin echo

CHAPTER 1.
INTRODUCTION

1.1 OVERVIEW

The efficiency of treatment delivery in current radiation treatment planning (RTP) procedures is limited by inherent (geometrical) uncertainties caused by the difficulty in identifying the accurate topography of the target during the course of the treatment. The main sources of error are comprised of internal organ motion, limited ability in defining the tumor extent and treatment inter-session setup variations. To account for these limitations, it is a common practice to add safety margins, which are defined considering population statistics, to the targeted anatomy.[1-5]

In recent years, advanced image guided radiotherapy (IGRT) techniques, aimed to improve the position verification process, were proposed for clinical use, specifically (a) cone-beam computed tomography (CBCT) in conjunction with a linac[6], (b) tomotherapy[7, 8], (c) ultrasound imaging[9], (d) portal image verification (PIV) based on transmission images of bony anatomy[10] or pre-treatment implanted fiducial markers,[11] generated by the linac's megavoltage (MV) beam, and (e) kilovoltage (kV) images produced by an x-ray tube mounted on the linac.[12, 13] The main benefits of using such modalities include the reduction of the safety margins leading to a higher local tumor control and reduced normal tissue complications. Ideally, it is desired that the treatment planning process be adaptive, i.e. adaptive radiation therapy (ART). This concept refers to the constant adjustment of the patient treatment based on the day-to-day evolving image data regarding local variations in tumor's shape, size and location.[3, 5] To accomplish such objectives, the imaging component is a key factor. X-ray transmission-based images (kV or MV) show great bony detail but are inherently limited in resolving soft-tissue organ structures.[14] Ideally, MRI is the preferred imaging modality for ART as it is characterized by excellent soft-tissue contrast.[15-17]

More recently, the concept of integrating an MRI unit with a source of radiation, e.g. a megavoltage (MV) radiation therapy linear accelerator (linac)[18-24] or ^{60}Co,[25-27] emerged as a feasible novel approach for real time image guidance in ART. Such a modality would benefit

from the MRI's excellent soft-tissue contrast and its ability of multi-planar data acquisition. This would permit real-time tracking of the tumor and neighbouring healthy anatomy during treatment irradiation, ultimately facilitating on-line treatment plan optimization.

At Cross Cancer Institute (CCI), we are developing a novel hybrid MRI-Linac system consisting of a bi-planar 0.2 T permanent magnet coupled with a 6 MV radiotherapy accelerator.[22, 24, 28-32] Although, the integration of the MRI scanner and linac is a challenging task due to the mutual interaction between the two components, the system designed at the CCI has resolved the issues. To operate simultaneously and independently, the design has addressed certain technical difficulties, namely magnetic interference, radio frequency (RF) interference, and dose deposition effects in magnetic field.

Magnetic interference refers to the MRI scanner's magnetic field induced effects on the operation of the linac. Specifically, the presence of a sufficiently strong external magnetic field may alter the trajectories of the electrons produced inside the linac by the gun and accelerated through the waveguide before reaching the target. Thus the linac's waveguide is to be sufficiently shielded for the MRI's fringe fields to a level that the proper behaviour of the traveling electrons is unperturbed. The magnetic shielding can be (a) passive by using strategically designed and placed pieces of different metal materials aimed to deflect the magnetic field from the spatial regions of interest or (b) active by implementing special coil configurations to cancel out the external fringe fields at the desired location.

RF interference is mutual between the MRI scanner and the linac as both components are important RF sources. Various structures of a radiotherapy accelerator, e.g. klystron/magnetron and high voltage modulator, can generate sufficient RF noise that would interfere with the operating frequency of the MRI unit. To overcome such an impediment design-dependent techniques are implied such as (a) re-location the main sources of RF noise in a different room, (b) the synchronization of the linac's RF-signal triggering and pulse shaping (each pulse is 7 μs, with a frequency of 50 pulses/s) with the MRI RF image sequence read out (e.g. for a gradient echo

sequence the pulse is less than 1 ms and the pulse frequency is 100 pulses/s), and (c) RF shielding of the linac waveguide using a Faraday cage (i.e. fine mesh of copper).

The dosimetric effects refer to the change in the local behaviour of charged particles generated in a medium by radiation (e.g. x-ray) due to the presence of an externally applied magnetic field (i.e. $\vec{B}_0$ of the MRI scanner). Specifically, the trajectories of the secondary electrons between consecutive collisions are perturbed depending on the particles' kinetic energy and the strength of the external field. As a consequence, the dose deposition patterns may vary with the magnetic field strength. The impact of such effects in clinically relevant circumstances needs to be quantified.

The implementation of a hybrid MRI-Linac system would eliminate the need for additional CT imaging sessions as the entire treatment planning process can rely on the MR images only, i.e. MRI Simulation. Although, MRI is considered to be the imaging modality of choice for the delineation of target volumes used for RTP because of its superior soft-tissue contrast[15-17], MR images (a) lack electron density information required for treatment planning dose calculations and (b) suffer from geometric distortions, i.e. system-related[33-36] and object-induced[37-39] distortions. Due to these significant limitations, the MR images are traditionally used in conjunction with CT images.[40-42] Other important advantages of MRI over CT include (a) non ionizing procedure (no additional patient irradiation), (b) ability to perform multi-planar imaging, (c) availability of both functional and biological information, and (d) wide variety of tissue contrast mechanisms.[41]

In recent years, there has been an increasing interest in developing new techniques for MRI Simulation aimed to overcome the MR image drawbacks and improve the RTP process for brain[43-46] and prostate[47-49] cancer. To compensate for the lack of intrinsic electron density data, MR images can be prepared for dose calculations by assigning bulk CT values to the voxels

corresponding to segmented volumes of interest (VOIs).[44, 47, 48] These VOIs represent certain tissue types relevant to dosimetric calculations such as bone, lung, and soft tissue. Regarding MR image distortions, extensive methods were developed to investigate and correct for distortions.[33, 34, 36, 50]

The RTP verification process, i.e. correct (re-)positioning of the patient before and during the treatment, can be performed based on the registration process between (a) digitally reconstructed radiographs from MR images (MR-DRRs) and CT/MVCT or (b) MR diagnostic images and real-time MR data (in particular for an MRI-Linac system). The MR-DRRs are usually generated by segmenting the MR data sets into dosimetric relevant VOIs (e.g. bone, soft-tissue) and assigning to them bulk electron density information.[51-53]

The goal of this work (see Fig. 1.1) is (a) to develop an MRI Simulation procedure for intracranial lesions, including the MR-distortion correction and assignment of bulk CT values, and (b) to investigate two aspects of the MRI-Linac system design, i.e. magnetic interference and dosimetric effects. Specifically, Chapter 1 (Section 1.2) along with the Appendix briefly introduces the basics of MRI. Chapter 2 presents a phantom-based method for the measurement, analysis and correction of 3D system-related distortions in MRI. Chapter 3 describes a procedure for the treatment planning of intracranial lesions based solely on MR images. Chapter 4 examines the dosimetric effects and magnetic passive shielding of an MRI-Linac system based on a 0.2 T bi-planar magnet.

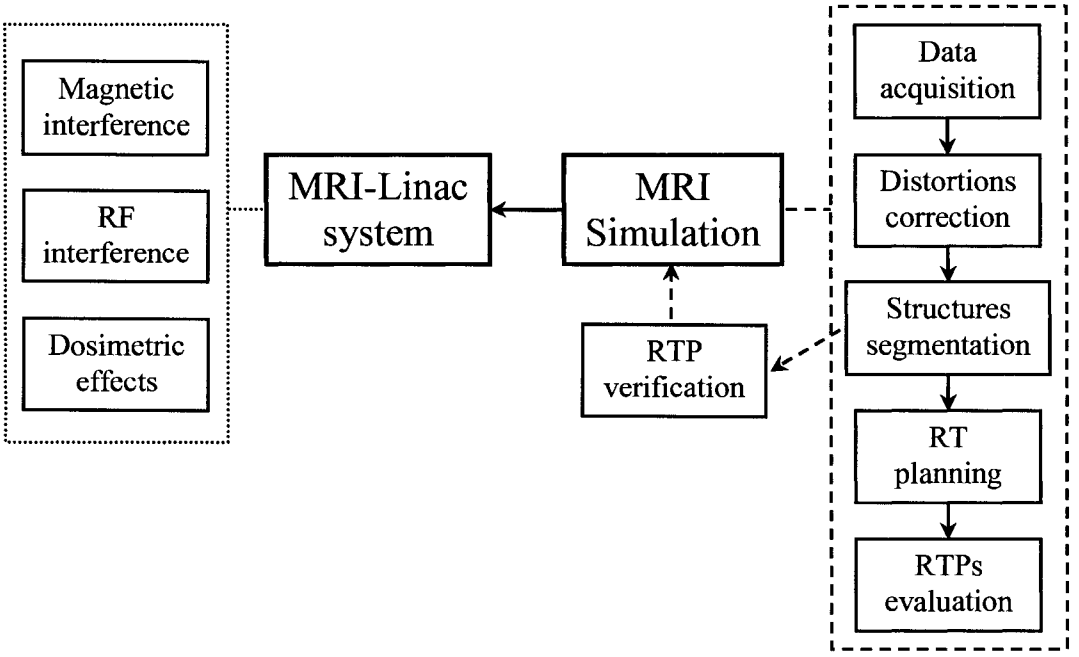

Figure 1.1 Diagram showing the workflow of the MRI Simulation procedure for intracranial lesions and the main issues that need to be addressed before implementing a hybrid MRI-linac system. The components highlighted in blue are discussed in the present work.

1.2 MAGNETIC RESONANCE IMAGING

1.2.1 Brief historical overview

MRI is an imaging modality used to acquire clinical images and to study tissue metabolism in vivo. Its mechanism is based on nuclear magnetic resonance (NMR). This phenomenon refers to certain nuclei that absorb energy in the radiofrequency (RF) limits of the electromagnetic spectrum when placed in an external magnetic field. The nuclei also emit the absorbed energy during the de-excitation process to their equilibrium state. The NMR effect was independently discovered in bulk materials by Bloch and Purcell[54-56] in mid 1940s.

In its early years, NMR was mainly applied in chemical and molecular structure analysis.[57, 58] Only in the 1970s was it proven by Damadian that normal and tumor tissues show different relaxation times.[59] This development suggested the potential of applying NMR in cancer diagnosis. During the same period, Lauterbur demonstrated for the first time the basics of MRI using small tube samples.[60] In the late 1970s, Ernst proposed the use of phase and frequency encoding for image acquisition along with the Fourier Transform method for image reconstruction.[61] Another important contribution, namely the development of echo-planar imaging (EPI) that laid the foundation of fast imaging techniques, e.g. functional MRI (fMRI), was made by Mansfield.[62]

One of MRI's first clinical applications was identified in early 1980s and was related to its ability to detect abnormalities in the brain's posterior fossa and in the upper cervical spine.[63, 64] This type of diagnostic was difficult to perform using CT, i.e. the standard head and body imaging procedure at that time, due to the presence of various bony structures in those regions.

In mid 1980s, MRI started to play an important role in central nervous system (CNS) investigations as a complementary imaging modality to CT.[65-67] However, MRI was only minimally used as a diagnostic tool for other parts of the body.[68, 69] This was mainly due to the

reduced field strength of MRI scanners available at that time. The scans were impractically long, and as a consequence the image datasets obtained from such examinations were drastically altered by the subject's respiration and heart motion. Starting in late 1980s, the development of higher field magnets and computer technology allowed the implementation of superior imaging techniques, e.g. faster scan time. Today, MRI is considered to be the preferred imaging modality for most parts of the body, e.g. CNS, musculoskeletal system, cardiovascular system, etc.

1.2.2 Magnetic properties of the materials

The dominant nucleus in most MRI studies is the proton in hydrogen, i.e. the ^{1}H species, because of its high natural concentration in the human body and its NMR sensitivity. ^{1}H is an integral component of water (H_2O), which represents roughly 60% of the human body, and fat ($-CH_2-$). Intuitively, the high sensitivity of ^{1}H is suggested by the presence of only one electron that can interfere with the magnetic properties of the proton. The lack of electron shielding is in particular more pronounced for the proton in water as the O-H bond is ionic. This tends to remove the electron from the ^{1}H atom resulting in a proton that is more sensitive to external influences.

Most objects exhibit induced magnetism and possess a magnetic field only under the influence of an externally applied magnetic field, i.e. $\vec{B}_0$. For an isotropic sample, the induced magnetic moment shares the same direction with $\vec{B}_0$ and it is given by

$$\vec{\mu} = \frac{1}{\mu_0} V \chi \vec{B}_0 \tag{1.1}$$

where μ_0 is the magnetic permeability of vacuum constant ($4\pi \cdot 10^{-7}$ N/A^2), V is the volume of the sample, and χ is the magnetic susceptibility of the sample (can be either positive or

negative). χ characterizes the magnetic properties of the material when it is exposed to $\vec{B}_0$. Substances with $\chi < 0$, i.e. diamagnetic materials, have no unpaired orbital electrons and when placed in $\vec{B}_0$ exhibit a weak magnetic field that opposes $\vec{B}_0$. As a result the net magnetic field is reduced, i.e. the diamagnetic material tends to push the magnetic field out of the sample. This is the case for most of the tissues present in the human body. In contrast, substances with $\chi > 0$, i.e. paramagnetic materials, have unpaired orbital electrons and become magnetized in the presence of $\vec{B}_0$. A weak magnetic field is induced in the sample with the same orientation as $\vec{B}_0$. In other words, paramagnetic materials tend to pull the magnetic field into the sample. As an example, gadolinium (Gd) has seven unpaired electrons and this makes it a strong paramagnetic material. Other materials, with a very large χ value, i.e. ferromagnetic substances, become permanently magnetized even after the magnetic field is withdrawn. In nature, there are only three ferromagnetic elements: iron, nickel, and cobalt. There are also three other less frequently encountered categories of magnetic properties: ferrimagnetism, antiferromagnetism, and superparamagnetism.

1.2.3 Basic considerations of MRI

Let us consider a water sample. The proton nuclei present an intrinsic magnetic property, i.e. a nuclear magnetic moment ($\vec{\mu}$). This quantity is introduced in Appendix A.1 (Eq. A.2), which describes the stationary states of a single isolated spin. $\vec{\mu}$ is characterized by the gyromagnetic ratio (γ) and the nuclear spin angular momentum ($\vec{J}$). The latter quantity is a consequence of proton's particular innate structure. Namely, a proton is built out of three quarks, i.e. fundamental particles considered to be the "bricks" of the universe along with leptons (e.g. electron) and force mediation particles (e.g. photon, gluon, etc.). Two of the quarks have charge $+2e/3$ (e being the

unit electronic charge) while the other one has charge $-e/3$, but all of them have the same spin ½. Considering that two of the quarks are in antiparallel spin configuration, the net spin of the proton is ½.

To perform an MRI experiment on our sample we need to (i) prepare the nuclear magnetic system, (ii) excite the system by transferring it a certain amount of energy, and (iii) acquire the signal released by the system during its relaxation process towards thermal equilibrium.

(i) Preparation of a nuclear magnetic system

In the absence of an external magnetic field ($\vec{B}_0$), protons have spin polarization vectors distributed almost uniformly, pointing in all directions in space. As a consequence, the net magnetic moment of the sample, i.e. the sum of all protons' magnetic moments, is approximately zero, since roughly the same number of spins point towards a particular direction as against it. If $\vec{B}_0$ is suddenly turned on, the proton spins start interacting with $\vec{B}_0$. This process is described in Appendix A.1 for the case of a single spin. There are only two energy states available for each proton, i.e. spin-up and spin-down, respectively.

The population of spin-up and spin-down energy states is described by the Boltzmann factor. This quantity is defined in Appendix A.2 (Eq. A.13) which introduces the Maxwell-Boltzman statistics for an ensemble of spins ½. The Maxwell-Boltzmann distribution accounts for the fact that the lower energy eigenstates (spin-up) are slightly more populated than the higher energy eigenstates (spin-down). At room temperature and for nuclei with $\gamma > 0$ the number of protons found in the spin-up state exceeds the ones in the spin-down state by approximately $1{:}10^5$. Therefore, the net magnetization vector of the ensemble ($\vec{M}$) points in the same direction as $\vec{B}_0$ (usually z-axis). This quantity is also called net longitudinal magnetization and represents the sum

of all proton magnetic moments in the sample, i.e. $\vec{M} = \sum_n \mu_n$. In addition, the expectation value of the net transverse magnetization, i.e. the component of $\vec{M}$ in the (*x,y*)-plane, is zero.

$\vec{J}$ can be located with equal probability anywhere on the surface of a cone around z-axis (see Appendix A.1). The classical interpretation of this process is that $\vec{M}$ precesses (rotates on the surface of a cone) around $\vec{B}_0$.

(ii) Excitation of a nuclear magnetic system

A nucleus can be excited, i.e. moved from a lower to a higher energy state, through the absorption of a photon carrying an energy that corresponds to the energy difference between the two states. The nucleus can also de-excite by emitting a photon transporting the energy difference of the two transition states. In MRI, the protons are excited by using certain electromagnetic pulses which correspond to the radio frequency window of the electromagnetic spectrum, i.e. radiofrequency (RF) pulses. The frequency of such a pulse falls in the range of 3-100 MHz, with a corresponding wavelength and energy of 6-60 m and 20-200 MeV, respectively. A specially designed coil is typically used to transmit/receive RF pulses, i.e. excitation/receiver coil, through the brief application of an alternating electric current.

Once an RF pulse is applied, the thermal equilibrium of the spin system is perturbed. The protons experience two different magnetic fields, i.e. the static field generated by the magnet ($\vec{B}_0$) and a new field ($\vec{B}_1$) produced by the excitation coil. To affect $\vec{M}$ precession, $\vec{B}_1$ has to be a time dependant and circularly polarized magnetic field rotating about $\vec{B}_0$. Comparing the two fields, the magnitude of $\vec{B}_0$ is much larger than the strength of $\vec{B}_1$. However, if the RF pulse is applied for long enough $\vec{B}_1$ can give rise to a significant change in the spin system behaviour. Specifically, $\vec{M}$ can be tipped from *z*-axis leading to the generation of a non-zero value of $\vec{M}_{xy}$.

Immediately, $\vec{M}_{xy}$ starts to experience a torque $\vec{M}_{xy} \times \vec{B}_0$ equal to the rate of change of spins ensemble angular momentum.

Appendix A.3 describes the spin excitation process by using the concept of the rotating frame, i.e. a new system of reference which is attached to the time dependant and circularly polarized magnetic field $\vec{B}_1$. The equation of motion in the rotating frame has a similar form as the one corresponding to the laboratory frame. The main difference between the two is that the net magnetic field $\vec{B}$ is replaced by a static effective field $\vec{B}_{eff}$ (defined in the rotating frame). In this case, $\vec{M}$ precesses around $\vec{B}_{eff}$ with the frequency $\omega_{eff} = \gamma B_{eff}$. Considering Eq. (A.22),

$$\vec{B}_{eff} = B_1 \cdot \vec{i}_\rho + (B_0 + \omega_1 / \gamma) \cdot \vec{k}_\rho \tag{A.22}$$

the second term $(B_0 + \omega_1 / \gamma) \cdot \vec{k}_\rho$ is removed by applying the resonance condition $|\omega_1| = \omega_0 = \gamma B_0$, where ω_0 is the Larmor frequency (see Appendix A.1). As a result, $\vec{B}_{eff}$ becomes parallel to the RF field, along the x-axis of the rotating frame, namely $\vec{B}_{eff} = B_1 \cdot \vec{i}_\rho$. Hence, $\vec{M}$ rotates (at $\omega_1 = \gamma B_1$) in the $y_\rho z_\rho$-plane as the cone of precession corresponding to $\vec{M}$ flattens into this plane.

By applying an RF pulse with a frequency that matches the proton Larmor frequency we can modify the direction of the net magnetization vector, resulting in the perturbation of the spin ensemble. If for example $\vec{B}_1$ is turned off after a time $t = \pi / 2\gamma B_1$ (from $\omega_1 t = \pi / 2$), i.e. we apply a 90° pulse, $\vec{M}$ is placed along the y_ρ-axis. Furthermore, if $t = \pi / \gamma B_1$ (from $\omega_1 t = \pi$) we have a 180° (inversion) pulse that has the effect of placing $\vec{M}$ along negative z_ρ-axis. Both 90° and 180° pulses are routinely used in MRI as standard forms of sample excitation.

(iii) Relaxation of a nuclear magnetic system and MRI signal acquisition

Immediately after the energy transfer, when the RF pulse is turned off, the excess nuclei located in the higher energy state start to return to the lower energy state to recover the initial equilibrium. This is done through the emission of electromagnetic energy which can be detected by using an RF probe. Since the frequency of such a signal is characterized by the energy difference between the two transition states of the protons and the signal decay depends on the protons' molecular environment, the NMR signal reflects certain properties of the protons and their environment.

The process that occurs after the termination of the RF pulse, in which the thermal equilibrium is re-established through the interactions of the spin system with the molecular environment, is called relaxation. One of the simplest description of protons' relaxation behaviour is based on Bloch's equations (see Appendix A.4). In this phenomenological approach two time constants are introduced, namely T_1 as the longitudinal or spin-lattice relaxation constant and T_2 as the transverse or spin-spin relaxation constant. The recovery process takes place in such a way that the longitudinal and transverse magnetizations, characterized by T_1 and T_2, respectively, can be analyzed separately.

Longitudinal relaxation

T_1 relaxation involves an energy exchange between the spin system and its molecular environment that leads to the return of spin populations to their thermal equilibrium values. The mechanism originates in the microscopic magnetic fields present in the sample. Specifically, the protons act like magnetic dipoles generating inter-nuclear fields. In addition, the electronic system can also generate microscopic fields (due to electron's magnetic moment). The relaxation is characterized by the transfer rate of spins' excess energy to the surrounding medium (lattice) through local magnetic interactions (dipole-dipole).

In Appendix A.4, Eqs. (A.26) give the general solutions of Bloch equations. The T_1 relaxation following a 90° pulse is described by

$$M_z(t) = M_0(1 - e^{-t/T_1}) \tag{1.2a}$$

as $M_z(0) = 0$. Similarly, the longitudinal relaxation following a 180° pulse (i.e. inversion recovery) is given by

$$M_z(t) = M_0(1 - 2e^{-t/T_1}) \tag{1.2b}$$

considering $M_z(0) = -M_0$. The two cases are shown in Fig. 1.2. The realignment of the protons along $\vec{B}_0$ results in a gradual increase of M_z up to its thermal equilibrium (maximum) value.

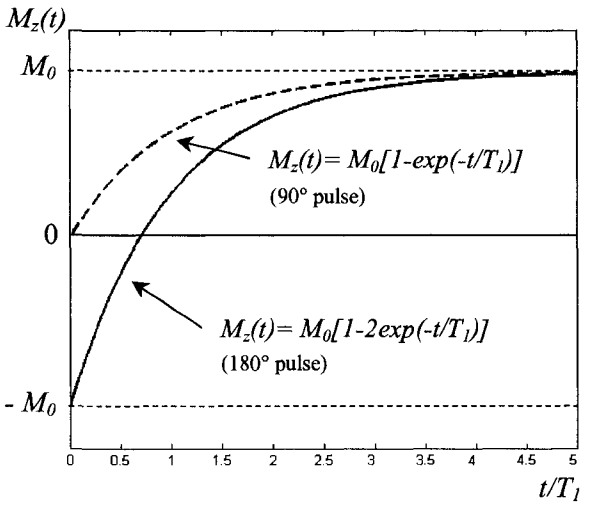

Figure 1.2 Longitudinal relaxation following an 90° (dashed line) and 180° (solid line) RF pulse, respectively.

Transverse relaxation

This relaxation process refers to the decay in spins coherence leading to the gradual decrease of M_{xy}. At resonance, following a 90° pulse, the net magnetization (M_0) is placed in the transverse plane, namely M_{xy} reaches its maximum value. Assuming that $\vec{B}_0$ is perfectly uniform and the spins do not interact with each other, all the spins rotate in the (x,y)-plane with frequency ω_0 about $\vec{B}_0$. In practice, different spins experience slightly different magnetic fields, so that they precess at slightly different frequencies causing a gradual loss of synchronization. This translates into a decay of M_{xy} from M_0 to zero. The reduction in spin coherence does not necessarily involve exchange of energy with the surroundings. The main factors responsible for the transverse relaxation process are: $\vec{B}_0$ inhomogeneities caused by magnet manufacturing shortcomings, local magnetic fields generated by protons (and unpaired electrons) dipole-dipole interactions, and magnetic susceptibility variations between neighbouring tissues.

1.2.4 Signal formation

The NMR signal is produced by the precession of the transverse magnetization following an RF pulse. Namely, a rotating magnetic moment gives rise to a rotating magnetic field. Considering Maxwell's equations, a varying magnetic field is associated with an electric field, i.e. $\vec{\nabla}\times\vec{E} = -\partial\vec{B}/\partial t$, where $\vec{E}$ is the electric field. By placing a receiver coil near the sample, $\vec{E}$ sets the electrons in the coil in motion generating an oscillating current that can be recorded using a sensitive RF probe. This induced current represents the NMR signal or free-induction decay (FID). Even though the signal is small we can detect it as it oscillates (e.g. sinusoid) at a well-defined frequency (Larmor frequency ω_0). In frequency space, the signal is represented by a spectrum representing a delta function centered on ω_0.

The transverse decay mechanism leads to a gradual vanishing of the NMR signal. The decay consists of two components: a) irreversible decay due to temporal field inhomogeneities (caused by local dipole-dipole interactions and susceptibility gradients), and b) reversible decay (e.g. generated by static $\vec{B}_0$ field non-uniformities).

The loss of spins' coherence due to static inhomogeneities, which induces a continuous drop of the NMR signal, can be reversed by applying refocusing pulses, i.e. 180° pulse along the x or y axis. For example, after a 90° pulse applied along x-axis the net magnetization lies along y-axis. Immediately, the spins start to fan out, precessing with slightly different frequencies. By applying a y-180° pulse, the motion (direction of precession and velocity) of the de-phased spins is reversed. Hence, the spins regroup back along y-axis inducing in the coil a positive echo, i.e. an NMR signal with a similar amplitude as the one detected before the spins' loss of coherence. Similarly, by applying an x-180° pulse, a negative echo (negative amplitude) is induced. However, in practice, due to the irreversible decay component, it is impossible to recover the full amplitude of the initial NMR signal. Perfect echo formation requires that the local magnetic fields experienced by the spins do not change during the pulse sequence. Over time, even after the application of repetitive refocusing pulses, the NMR signal dies out. The transverse relaxation is characterized by a time constant T_2^*, which is defined as $\frac{1}{T_2^*}=\frac{1}{T_2}+\frac{1}{T_2'}$, where T_2 and T_2' characterize the irreversible (intrinsic) and reversible decay components.

The M_{xy} intrinsic decay process can be described by using the first two rate equations from Eqs. (A.26) as follows

$$M_{xy}(t)=M_{xy}(0)e^{-t/T_2} \tag{1.3}$$

where $M_{xy}(0)=\sqrt{M_x^2(0)+M_y^2(0)}$. For example, considering a 90° pulse, $M_x(0)=0$, and $M_y(0)=M_0$ we obtain $M_{xy}(t)=M_0e^{-t/T_2}$. Similarly, Eq. (1.3) can be written for T_2^* . Figure 1.2 illustrates the transverse decay process (governed by T_2^* and T_2) through the application of repetitive 180° refocusing pulses.

In Eqs. (A.26), the case of $t\rightarrow\infty$ represents a relaxation limit, with $M_z(\infty)=M_0$ and $M_{xy}(\infty)=0$, meaning that the net magnetization vector recovers back to its thermal equilibrium value after a sufficiently long relaxation time. The decay of M_{xy} normally takes a shorter time than the recovery of M_z, i.e. $T_2<T_1$. The limiting case is when $T_2=T_1$ as the fluctuating microscopic fields are not able to tip the spins along z-axis while maintaining spins coherence in the transverse plane. For water protons, the typical values for T_1 and T_2 are roughly 1s and 100 ms, respectively.

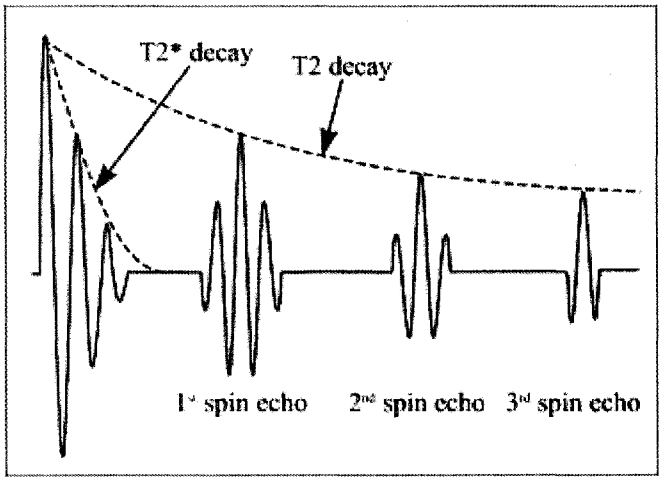

Figure 1.3. T_2^* and T_2 decay processes highlighted by applying a set of refocusing pulses.

1.2.5 Contrast mechanisms

The protons' signal response depends on their molecular environment. Namely, the T_1 and T_2 characteristics of a tissue are determined by the way the protons exchange energy with the surrounding lattice and by the dephasing rate of the spins. As a consequence, in the brain for example, structures like white and grey matter possess distinct T_1 and T_2 values. In practice, this difference in relaxation times constitutes the foundation of various tissue contrast mechanisms. Specially designed pulse sequences, i.e. series of RF pulses with one or more MR signal measurements, are used to benefit from this effect, specifically to enhance or suppress the visualization of certain tissues with respect to their surroundings. Two of the most commonly used pulse sequences are: inversion recovery (IR), based on the T_1 contrast mechanism, and spin echo (SE), based on the T_2 relaxation process.

The SE technique is one of the most common pulse sequence used in MRI. It is based on a 90° pulse, required to excite the net magnetization, followed by one or more 180° refocusing pulses, which generate signal echoes (see Fig. 1.3). The IR pulse sequence consists of a 180° pulse followed after a certain delay (TI) by a 90° pulse. The 180° pulse flips the direction of net magnetization vector from $+z$ to $-z$-axis. Once the pulse is turned off, spin populations relax back towards thermal equilibrium (T_1 curve – see Fig. 1.2). In other words, during TI, different tissues relax faster or slower depending on their intrinsic T_1. After TI, the z-magnetization of different tissues recovered in different proportions. Next, the 90° pulse tilts the partially recovered z-magnetization into the (x,y)-plane where the signal is usually rephased by means of a 180° pulse, similarly as for a SE sequence. The IR sequence provides strong contrast between tissues having different T_1 relaxation times. It can also be used for suppressing tissue signals, e.g. fluid or fat.

Comparing different tissues in the brain on a T_1 recovery curve, the white matter appears bright due to its high fat content, which is characterized by an efficient energy exchange (short T_1). The gray matter and the cerebro-spinal fluid (CSF) show intermediate and low signal values, respectively, due to their increased water content, which leads to a less efficient energy transfer (long T_1). In contrast, when considering the T_2 decay curves, CSF undergoes the smallest loss in spins' coherence (longest T_2), whereas the white matter has a shorter T_2 value than the gray matter.

1.2.6 Spatial encoding and image formation

The only presence of the external static and homogeneous magnetic field ($\vec{B}_0$) does not allow to distinguish the signals produced at different spatial locations in the imaged sample, as the spins resonate at the same frequency. The recorded signal following the RF pulse constitutes the combined signal contribution from all excited protons in a single time waveform. To be able to spatially select regions of interest and determine the source location of each signal component we need to apply gradient fields. A gradient field is defined as an inhomogeneous magnetic field that varies linearly from point to point and is produced for certain periods of time by means of specially designed coils, i.e. gradient coils. To obtain spatial information, a gradient has to be independently applied along each of the x, y, and z directions. Depending on their function, the gradients can be defined as slice-select, frequency-encoding (or readout), or phase-encoding gradients.

The slice-select gradient is normally applied along the z-axis (G_z), i.e. head-to-feet direction. As a consequence, each position in the sample has its own resonant frequency as the magnetic field varies locally. For example, in a brain study, the magnetic field gradually changes from the base of the skull to its vertex. With the slice-select gradient turned on, if we apply an RF pulse, characterized by a specific range of frequencies (i.e.

bandwidth), we can excite only a well-defined volumetric region (slice) of the sample, i.e. selective excitation. The protons located in the rest of the imaged object remain unexcited as the RF pulse's bandwidth does not match their Larmor frequencies. The thickness of the selected slice (Δz) is determined by the gradient strength (G_z) and the bandwidth of the RF pulse (BW_{rf}) as follows

$$\Delta z = \frac{BW_{rf}}{\gamma G_z} \tag{1.4}$$

The slice position can be varied by modifying the reference frequency. Once a slice of interest has been selected, we need to discriminate the in-plane signal location. This is achieved by independently encoding protons' precession parameters, i.e. phase angle and frequency. The frequency encoding is accomplished by applying a readout gradient along a fixed direction (usually x-axis - G_x) during the signal acquisition process. To obtain a proper representation of the frequency components the signal needs to be sampled in accordance with the Nyquist criterion, specifically the sampling frequency (BW_x) is given by

$$BW_x \geq \gamma G_x FOV_x \tag{1.5}$$

where $FOV_x = N_f \Delta x$ is the x-dimension of the imaged field of view, N_f is the number of data points collected during one readout (e.g. 256, 512), and Δx represents the pixel resolution in the x-direction. As an effect, N_f columns of protons precessing at the same frequency. Thus we can not distinguish between the protons of each column as they are characterized by the same phase value. To locate the protons in the other orthogonal direction we need to introduce a phase encoding gradient (G_y). This encoding normally

occurs immediately after the 90° excitation pulse and before the readout process. By varying the strength of G_y before repeating readouts, subsequent rows of protons undergo different extra precession frequency shifts. The sampling equation for G_y is given by

$$\Delta G_y \leq \frac{1}{\gamma FOV_y \tau} \tag{1.6}$$

where τ is the G_y operation time, $FOV_y = N_p \Delta y$ is the y-dimension of the imaged field of view, N_p is the number of points in the phase encode direction (e.g. 256, 512), and Δy is the pixel resolution in the y-direction. By subsequently making use of the slice-select, phase and readout gradients, we can resolve the signal corresponding to each voxel. Specifically, the protons of different voxels experience distinct frequency and phase values that are directly correlated to the spatial coordinates of the voxels.

The total signal detected (i.e. S) is given by the integral of the contributions arising from all the voxels of the imaged sample as follows

$$S(t_1, t_2) = \int\int M(x, y) e^{2\pi i [f(x)t_1 + \varphi(y)t_2]} dxdy \tag{1.7}$$

where $f(x) = \gamma G_x x$ represents the frequency corresponding to the columns along the frequency encoding direction and $\varphi(y) = \gamma G_y y \tau$ is the phase corresponding to the rows along the phase encoding axis. Equation (1.7) can be written as

$$S(k_1, k_2) = \int\int M(x, y) e^{2\pi i (k_x x + k_y y)} dxdy \tag{1.8}$$

by using the substitutions $k_x = \gamma G_x t_1$ and $k_y = \gamma G_y t_2$. Equation (1.8) suggests that the readout signal is stored in k-space, which is equivalent to a Fourier plane. In k-space the x and y spatial frequencies are replaced by k_x and k_y, respectively. Images of the imaged sample can be generated by applying 2D Fourier transform (i.e. 2D FT) analysis to the encoded signal. Specifically, by taking an inverse 2D FT of Eq. (1.8) we obtain

$$M(x,y) = \int\int S(k_x,k_y) e^{-2\pi i(k_x x + k_y y)} dk_x dk_y \,. \tag{1.9}$$

The signal is acquired as a function of the image sequence's characteristics. This results in a sequence-specific pattern of filling the k-space, e.g. a typical spin echo sequence fills the k-space line by line. K-space is characterized by special properties such as its central and periphery regions contain the information regarding to the contrast and resolution, respectively, in the reconstructed image. Depending on the application, specially designed sequences can be implied to retrieve the k-space and subsequently generate images.

1.2.7 MR image distortions

Any error occurring in the magnetic field due to either scanner system's imperfections or local magnetic properties of the imaged sample translates into an erroneous encoding of the sample's spins after the image is reconstructed. This results in image distortions. As a consequence, the accurate representation of organ structures' topography, i.e. spatial location and relative intensity, is altered to a certain degree. Depending on the desired image's spatial accuracy, the image distortions can be significant and therefore, need to be investigated and possibly, rectified.

The MR image artifacts are caused by system-related and patient-induced distortions. The system-related distortions, inherent to any MRI scanner, are due to imperfections of the magnet

and its operating system, i.e. inhomogeneities in the main magnetic field ($\vec{B}_0$) and non-linearities in the applied magnetic field gradients (G_x, G_y, G_z). In contrast, the patient-induced distortions are generated by susceptibility (χ) and chemical shift (δ) variations in the imaged sample. Both types of distortions are dependent on the operation conditions, i.e. imaging sequence parameters.

System-related distortions

Ideally, a gradient field changes linearly with position as given by the dashed line in Fig. 1.4, e.g. for a gradient applied in x-direction we have

$$B_{G_x} = G_x \cdot x \tag{1.4}$$

where x is the position, G_x is the gradient strength and B_{Gx} is the resulting magnetic field due to G_x. However, in practice non-linearities in the gradient occur due to imperfect coil winding and eddy currents. Figure 1.4 shows that the signal produced by the spins located at position x is erroneously recorded at position x_1 as a consequence of local non-linearities in the gradient. The distorted coordinate x_1 is given by

$$x_1 = x + \frac{\Delta B_{G_x}(x)}{G_x} \tag{1.5}$$

where ΔB_{G_x} represents the magnetic field error due to the non-linearities. Gradient non-linearities occur along all encoding directions.

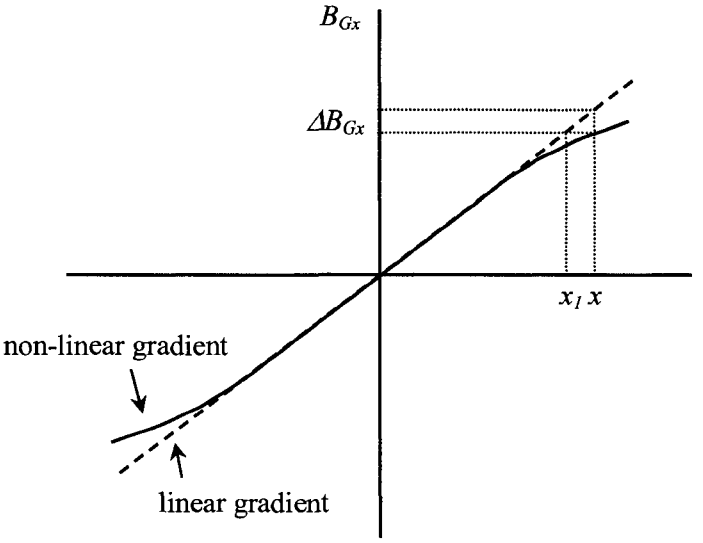

Figure 1.4. Gradient non-linearity generates geometric distortions. In the resulting MR image, the signal generated by the spins located at position x is erroneously depicted at position x_1.

Patient-induced distortions

Susceptibility-related image artifacts are produced at the boundaries between materials with significantly different susceptibility values, e.g. air-tissue interface. This effect is due to variations in the local magnetic field induced by the intrinsic properties of the materials (see Section 1.2.2).

Chemical shift-related image artifacts arise due to variations in the protons' resonant frequency in neighbouring tissues, e.g. water and fat. After being excited, the protons emit energy at a frequency depending on its molecular environment, i.e. magnetic shielding due to the electron clouds surrounding the protons.

1.2.8 MRI scanner designs for clinical applications

MRI scanners are characterized by strong, extremely uniform and stable over time magnetic fields. Different scanner designs were implied to achieve these special properties. One of the simplest approaches consists of permanent magnets made out of ferromagnetic material. A typical configuration of a permanent magnet-based MRI scanner is bi-planar, specifically two parallel opposing poles are separated by a certain air gap. The static magnetic field ($\vec{B}_0$) is established inside the magnet opening volume, having an orthogonal orientation with regard to the poles (i.e. *y*-axis). Another configuration comprises of a resistive electromagnet, which is a solenoid constructed out of copper wire wound around a cylindrical bore enclosing the imaging volume. The orientation of $\vec{B}_0$, generated by passing a current through the solenoid, is along the *z*-axis, into the bore. The most typical type of MRI scanner is represented by a superconductive electromagnet. To achieve the superconductivity properties, i.e. no resistance to electrical current flow, the coil material (e.g. niobium-titanium alloy) needs to be maintained at a very low temperature of approximately a few Kelvin (K). This is typically done by immersing the coils in liquid helium.

The advantage of building the scanner's electromagnet by using a superconductive wire is that stronger, more uniform and stable (i.e. ppm/hour) fields can be achieved. For some clinical applications, it is desired to have a high field to reduce the imaging time and achieve an improved image quality. Regarding the bore length, it is desired to have a short bore to increase patient comfort. For the permanent magnet-based scanners, the main advantage is their low post-installation maintenance costs. The field strength of such systems ranges from 0.1 T to 0.5 T. Their main disadvantage is that they are bulky systems, i.e. large and heavy structures. However, for certain clinical applications[22,49] their imaging abilities are considered to be sufficient.

1.3 REFERENCES

1. van Herk M. Errors and margins in radiotherapy *Semin. Radiat. Oncol.* 2006;14 52–64.
2. ICRU Report 62. Prescribing, Recording and Reporting Photon Beam Therapy (supplement to ICRU Report. 50). *International Commission on Radiation Units and Measurements* 1999:Bethesda, MD.
3. van Herk M, Remeijer P, Rasch C, Lebesque JV. The probability of correct target dosage: dose-population histograms for deriving treatment margins in radiotherapy. *Int J Radiat Oncol Biol Phys* 2000;47:1121-1135.
4. Balter J, Sandler HM, Lam K, Bree RL, Lichter AS, Haken RK Measurement of prostate movement over the course of routine radiotherapy using implanted markers *Int. J. Radiat. Oncol. Biol. Phys.* 1995;31 113–118.
5. Stroom J, Heijmen BJ. Geometrical uncertainties, radiotherapy planning margins, and the ICRU-62 report. *Radiother Oncol.* 2002 64:75-83.
6. Jaffray DA SJ, Wong JW, Martinez AA Flat-panel cone-beam computed tomography for image-guided radiation therapy. *Int. J. Radiat. Oncol. Biol. Phys.* 2002 53 1337-1349
7. Mackie TR HT, Swerdloff S, Reckwerdt P, Deasy JO, Yang J, Paliwal B, Kinsella T Tomotherapy: a new concept for the delivery of dynamic conformal radiotherapy *Med. Phys.* 1993 20 1709-1719.
8. Ruchala K, Olivera GH, Schloesser EA, Mackie TR Megavoltage CT on a tomotherapy system. . *Phys. Med. Biol.* 1999 44 2597-2621.
9. Serago C, Chungbin SJ, Buskirk SJ, Ezzeli GA, Collie AC, Vora SA Initial experience with ultrasound localization for positioning prostate cancer patients for external beam radiotherapy *Int. J. Radiat. Oncol. Biol. Phys.* 2002 53 1130-1138.

10. Gilhuijs K, Van de Ven PJH, Van Herk M. Automatic three-dimensional inspection of patient setup in radiation therapy using portal images, simulator images, and computed tomography data. *Med. Phys.* 1996;23 389-399

11. Nederveen A, Lagendijk JJW, Hofman P. Feasibility of automatic marker detection with an a-Si flat-panel imager. *Phys. Med. Biol.* 2001;46.

12. Drake D, Jaffray DA, Wong JW Characterization of a fluoroscopic imaging system for kV and MV radiography. *Med. Phys.* 2000 27 898-905

13. Shirato H, et al Four-dimensional treatment planning and fluoroscopic real-time tumor tracking radiotherapy for moving tumor *Int. J. Radiat. Oncol. Biol. Phys.* 2000 48 435-442

14. Groh BA SJ, Drake DG, Wong JW, Jaffray DA A performance comparison of flat-panel imager-based MV and kV cone-beam CT *Med. Phys.* 2002 29 967-975

15. Johnson P, Hunt SJ, Drayer BP. Human cerebral gliomas: correlation of postmortem MR imaging and neuropathologic findings. *Radiology* 1989;170:211-217.

16. Zawadzki M. MR imaging of the brain. *Radiology* 1988;166:1-10.

17. Sailer S, Rosenman JG, Soltys M, et al. Improving treatment planning accuracy through multimodality imaging. *Int J Radiat Oncol Biol Phys* 1996;35:117-124.

18. Raaymakers BW, Raaijmakers AJ, Kotte AN, *et al.* Integrating a MRI scanner with a 6 MV radiotherapy accelerator: dose deposition in a transverse magnetic field. *Phys Med Biol* 2004;49:4109-4118.

19. Raaijmakers AJ, Raaymakers BW, Lagendijk JJ. Integrating a MRI scanner with a 6 MV radiotherapy accelerator: dose increase at tissue-air interfaces in a lateral magnetic field due to returning electrons. *Phys Med Biol* 2005;50:1363-1376.

20. Raaijmakers AJ, Raaymakers BW, Lagendijk JJ. Experimental verification of magnetic field dose effects for the MRI-accelerator. *Phys Med Biol* 2007;52:4283-4291.

21. Raaijmakers AJ, Raaymakers BW, van der Meer S, *et al.* Integrating a MRI scanner with a 6 MV radiotherapy accelerator: impact of the surface orientation on the entrance and exit dose due to the transverse magnetic field. *Phys Med Biol* 2007;52:929-939.

22. Fallone B, Carlone M, Murray B, Rathee S, Stanescu T, Steciw S, Wachowicz K, Kirkby C. Development of a Linac-MRI System for Real-Time ART. [Abstract]. *Med Phys* 2007;34:2547.

23. Lagendijk J, Raaymakers BW, van der Heide U, Overweg J, Brown K et al. In Room Magnetic Resonance Imaging Guided Radiotherapy (MRIgRT). *Med Phys* 2005;32:2067

24. Fallone B, Carlone M, Murray B, Rathee S, Stanescu T, Steciw S, Kirkby C, Tomanek B, Sharp J. Development of a Small Bore Linac-MRI System for Real Time Image Guided Radiotherapy. [Abstract]. *Radiother Oncol* 2007;84:S3.

25. Dempsey J, Benoit D, Fitzsimmons JR, Haghighat A, Li JG et al. A Device for Realtime 3D Image-Guided IMRT. 2005;47th Annual ASTRO General Meeting, Denver, CO.

26. Yanez Y, Dempsey JF. Monte Carlo Simulations of Air Cavities in Phantoms Submerged in Magnetic Fields. *Med Phys* 2007;34:2590

27. Kron T, Eyles D, Schreiner JL, Battista J. Magnetic resonance imaging for adaptive cobalt tomotherapy: A proposal. *J Med Phys* 2006;31:242-254.

28. Fallone B, Carlone M, Murray B. Integrated External Beam Radiotherapy and MRI System. PCT International Patent. Vol WO/045076; 2007. pp. 5625-5635.

29. Fallone B, Carlone M, Murray B. Real-time Dose Reconstructed Using Dynamic Simulation and Image-Guided Adaptive Radiotherapy. PCT International Patent. Vol WO/045075; 2007. pp. 5625-5634.

30. Carlone M, Lamey M, Steciw S, Burke B, Fallone B. Study of RF Interference Between a Linear Accelerator and MRI. [Abstract]. *Med Phys* 2007;34:2621.

31. Murray B, Fallone G, Carlone M, Steciw S, Stanescu T, Rathee S. Designing a Linac to Operate Near an MRI. [Abstract]. *Radiother Oncol* 2007;84:S3.

32. Steciw S, Stanescu T, Carlone M, Fallone B. Magnetic Shielding of a Coupled MRI-Linac System. [Abstract]. *Med Phys* 2007;34:2623.

33. Doran SJ, Charles-Edwards L, Reinsberg S A and Leach M O. A complete distortion correction for MR images: I. Gradient warp correction. *Phys. Med. Biol.* 2005;50:1343-1361.

34. Wang D, Doddrell D M and Cowin G. A novel phantom and method for comprehensive 3-dimensional measurement and correction of geometric distortion in magnetic resonance imaging. *Mag. Res. Imag.* 2004;22:529-542.

35. Wang D, Strugnell W, Cowin G, Doddrell D M, Slaughter R. Geometric distortion in clinical MRI systems Part 1: evaluation using a 3D phantom. *Mag Res Imag* 2004;22:1211-1221.

36. Stanescu T, Jans H, Fallone BG. Investigation of a 3D MR Distortion Correction Protocol. [Abstract]. *Med Phys* 2006;33:2658

37. Chang H, Fitzpatrick JM. A technique for accurate magnetic resonance imaging in the presence of field inhomogeneities. *IEEE T Med Imaging* 1992;11:319-329.

38. Bakker C, Moerland MA, Bhagwandien R and Beersma R. Analysis of machine-dependant and object-induced geometric distortion in 2DDT MR imaging. *Magn. Reson. Imaging* 1992;10:597-608.

39. Reinsberg S, Doran SJ, Charles-Edwards EM, Leach MO. A complete distortion correction for MR images: II. Rectification of static-field inhomogeneities by similarity-based profile mapping. *Phys Med Biol* 2005;50:2651-2661.

40. Fraass B, McShan DL, Diaz RF, Ten Haken RK, Aisen A, et al. Integration of magnetic resonance imaging into radiation therapy treatment planning: I technical considerations. *Int J Radiat Oncol Biol Phys* 1987;13:1897-1908.

41. Khoo V, Joon DL. New developments in MRI for target volume delineation in radiotherapy. *Brit J Radiol* 2006;79:S2-S15.

42. Purdy J. Principals and Practice of Radiation Oncology. 3 ed: Lippincott-Raven; 1997.

43. Stanescu T, Syme A, Pervez N and Fallone B G. MRI-based treatment planning for radiotherapy of brain lesions. [Abstract]. *Med Phys* 2005;32:2033.

44. Stanescu T, Jans H-S, Stavrev P and Fallone B G. 3T MR-based treatment planning for radiotherapy of brain lesions. *Radiol Oncol* 2006;40:125-132.

45. Stanescu T, Jans H-S, Stavrev P, Fallone BG. A Complete MR-Based Treatment Planning Procedure for Radiotherapy of Intracranial Lesions. [Abstract]. *Med Phys* 2006;33:2271.

46. Stanescu T, Jans H, Pervez N, Stavrev P, Fallone BG. Developments in MRI Simulation of Intracranial Lesions. [Abstract]. *Radiother Oncol* 2007;84:S18.

47. Lee YK, Bollet M, Charles-Edwards G, Flower M A, Leach M O, McNair H, et al. Radiotherapy treatment planning of prostate cancer using magnetic resonance imaging alone *Radiother. Oncol.* 2003;66:203-216.

48. Chen L, Price R A Jr, Wang L, Li J, Qin L, McNeeley S, et al MRI-based treatment planning for radiotherapy: dosimetric verification for prostate IMRT. *Int. J. Radiat. Oncol. Biol. Phys.* 2004;60:636-647.

49. Chen L, Price Jr. RA., Nguyen T-B, et al. Dosimetric evaluation of MRI-based treatment planning for prostate cancer. *Phys Med Biol* 2004;49:5157-5170.

50. Baldwin L, Wachowicz K, Thomas SD, Rivest R, Fallone BG. Characterization, prediction, and correction of geometric distortion in 3 T MR images. *Med Phys* 2007;34:388-399.

51. Ramsey C, Arwood D, Scaperoth D, Oliver AL. Clinical application of digitally-reconstructed radiographs generated from magnetic resonance imaging for intracranial lesions. *Int J Radiat Oncol Biol Phys* 1999;45:797-802.

52. Chen L, Thai-Binh N, Elan MS, Chen Z, Wei L, Lu W, Price RA., Pollack A, Ma C. Magnetic resonance-based treatment planning for prostate intensity-modulated

radiotherapy: creation of digitally reconstructed radiograhs. *Int J Radiat Oncol Biol Phys* 2007;68:903-911.

53. Yin F, Gao Q, Xie H, Nelson D, Yu Y, et al. MR image-guided portal verification for brain treatment field. . *Int J Radiat Oncol Biol Phys* 1998;40:703-711.

54. Bloch F. Nuclear induction. Phys. Rev. Vol 70; 1946. p. 460.

55. Bloch F, Hansen WW, Packard M. The nuclear induction experiment. *Phys. Rev.* 1946;70:474

56. Purcell E, Torrey HC, Pound R. Resonance Absorption by Nuclear Magnetic Moments in a Solid. *Phys Rev* 1946;69:37-38.

57. Jadetzky O, Wertz JF Detection of sodium complexes by nuclear spin resonance. *Am J Physiol* 1956;187:608.

58. Odeblad K, Bhar NB, Lindstrom G. Proton magnetic resonance of human red blood cells in heavy water exchange experiments. *Arch Biochem Biophys* 1956;63:221-225

59. Damadian R. Tumor Detection by Nuclear Magnetic Resonance. *Science* 1971;171:1151-1153.

60. Lauterbur P. Image Formation by Induced Local Interactions: Examples Employing Nuclear Magnetic Resonance *Nature* 1973;242:190-191.

61. Kumar A, Welti D, Ernst R. NMR Fourier zeugmatography. *J Magn Reson* 1975;18:69-83

62. Mansfield P. Multi-planar image formation using NMR spin-echos. *J Phys C: Solid State Physics* 1977;10:L55-L58.

63. Bradley W, Waluch V, Yadley RA, Wycoff RR. Comparison of CT and MR in 400 patients with suspected disease of the brain and cervical spinal cord. *Radiology* 1984;152:695-702.

64. Bydder G, Steiner RE, Young IR, Hall AS, Thomas DJ, Marshall J, Pallis CA, Legg NJ. Clinical NMR imaging of the brain: 140 cases. *AJR* 1982;139:215-236.

65. Coffey C, Hines HC, Wang PC, Smith SL. The early applications and potential usefulness of NMR in radiation therapy treatment planning. Proc. Eighth International Conference on the Use of Computers in Radiation Therapy. Toronto, Canada; 1984. pp. 173-180.

66. Glatstein E, Lichter AS, Fraass BA, van de Geijn J. The imaging revolution and radiation oncology: Use of CT, ultrasound and NMR for localization, treatment planning and treatment delivery. *Int J Rad Oncol Biol Phys* 1985;11:1299-1311.

67. Shuman W, Griffin BR, Haynor DR, Johnson JS, Jones DC, Cromwell LD, Moss AA. MR imaging in radiation therapy planning. *Radiology* 1985;156:143-147.

68. Glazer G, Gross BH. Aisen AM, Quint LE, Francis IR, Orringer MB Imaging of the pulmonary hilum: A prospective comparative study in patients with lung cancer. *Am J Radiol* 1985;145:245-248.

69. Heelan R, Martini K, Westcott JW, Bains MS, Watson RC et al. Carcinomatous involvement of the hilum and mediastinum: Computed tomographic and magnetic resonance evaluation. *Radiology* 1985;153:111-115.

CHAPTER 2.

A 3D SYSTEM DISTORTION CORRECTION METHOD FOR MRI

2.1 INTRODUCTION

One of many applications of MRI is in radiation treatment planning (RTP) of cancer sites. RTP requires precise information about the topography, i.e. shape and location, of the tumor and the surrounding organ structures to ensure accurate delivery of radiation. Due to its remarkable soft tissue contrast MRI has proven to be the preferred imaging modality for the segmentation of anatomical structures. In particular for brain, studies[1-3] showed that the tumor definition can be improved with up to 80% by using MRI data as compared to CT data. For prostate, by comparing the organ volumes delineated on corresponding CT and MRI datasets, it was found that CT-defined volumes overestimated the MRI structures by as much as 40% due to CT images limited soft-tissue contrast.[4-6] However, it is recognized that MR images suffer from system-related and patient-induced distortions (see Section 1.2.7) that alter the accurate representation of anatomical structures, i.e. spatial location and relative intensity.

The current work is motivated by our interest in developing 3T MR-based radiation treatment planning procedures, i.e. MRI Simulation, in particular for brain[7-10] and prostate. The major limitations of MR images in this regard are the lack of electron density information and reduced spatial accuracy due to distortions. However, recent studies showed that brain[7-10] and prostate[11-13] MR images can, for the purpose of dose RTP calculations, be converted into CT-like images by assigning relevant electron density information to structure contours. In addition, the spatial accuracy of the patient MR images is a *conditio sine qua non* as the treatment planning process will rely only on the information derived from these images. To be used for MRI Simulation, the MR datasets have to be corrected to a degree that is acceptable in RTP, i.e. spatial resolution accuracy less than 2 mm.[14-17]

The MR image system-related distortions are due to inhomogeneities in the main magnetic field and non-linearities in the applied magnetic field gradients while the patient-induced artifacts are generated by susceptibility and chemical shift variations in the imaged object.

Both types of distortions are dependent on the operation conditions (i.e. imaging sequence) and ideally should be corrected before the MR images are integrated into the treatment planning process. It is common practice to independently analyze the system-related and patient-induced distortions by using distinctly different techniques. Specifically, the system-related image artifacts are determined and corrected by using a) phantom-based experimental procedures[18-26] and/or b) theoretical methods based on spherical harmonics.[18, 27] The experimental methods rely on the direct measurement of the distortion field by using a linearity object. The MR images of the linearity object embed the information regarding the distortion field, which can be extracted by analyzing the images in conjunction with a reference template, e.g. the physical dimensions of the linearity object. In contrast, the theoretical techniques are based on numerical simulations of the scanner's magnetic field local variation. The spherical harmonics are quantities that can approximate the gradient set of any MRI unit. The system-related distortions are inherent to any MRI scanner and can be determined independently of the imaged object.

The patient-induced distortions can be accounted for by using methods based on a) the measurement of the magnetic field distortion map,[28, 29] b) correlating two or more images of the same sample without calculating or measuring the local magnetic field,[30-32] and c) magnetic field calculations using one image dataset that is converted into a susceptibility distribution.[21, 33-36] The core of technique a) relies on the determination of the image phase difference between two distinct scans (e.g. relative delay in the data acquisition process) and its subsequent conversion into a local distortion field used for correcting the images. Method b) consists of acquiring two datasets of the same object under the same imaging conditions except the phase/read out gradient characteristics (e.g. polarity). The correct location of the imaged anatomy is calculated as the averaged value of the distorted positions of its constituent sub-structures in the two corresponding datasets. In Method c) the acquired dataset is converted into a magnetic susceptibility map by segmenting the images in regions characterized by significantly different susceptibility values, i.e.

air and different tissues. This is followed by the calculation of the local magnetic field and subsequent correction of the images.

In general, any system distortion correction method relies on two main components: (a) a technique for the identification and registration of the *true* (reference dataset, e.g. CT) and distorted (MR dataset) locations of the reference points, i.e. control points, used to sample the volume of interest, and (b) a procedure to determine the distortion field along with an image distortion correction algorithm. To find the accurate location of both *true* and distorted control points is vital as the distortion field is characterized by the displacement vectors of the distorted points from their *true* location.

There is a considerable amount of literature published over the last two decades on the mechanism of MR distortions and methods to correct the MR image artifacts[28, 37, 38]. However, in the last few years, there has been an increased interest in developing advanced 3D system distortion correction techniques that allow an improved control of distortions. Two of the most influential works were performed by Wang *et al*[19, 39] and Doran *et al.*[16, 18]

Wang *et al*[19, 39] investigated a method that relies on Prewitt operators, i.e. first derivatives along the main axes, by using a grid sheets phantom filled with a water-based solution. The control points were defined by the grid lattice and the water-grid interface. A typical MR image obtained with a grid sheets phantom shows a dark grid (grid sheet material – no signal) on a light background (signal from water). To extract the location of the MR (distorted) control points, as a first step, the authors generated images by determining the first derivative along z-axis (slice-selection direction). The newly generated images were convolved with an arbitrarily chosen image cross mask to highlight the grid intersection points. At this point, the images are processed by using a certain intensity threshold to produce additional images containing regions of interest that embed the control points' relative coordinates. These images are subsequently used to obtain an initial estimate of the control points location by using 1D profiles along the x and y axes. The

final location of each control point is found by determining the Prewitt operators along the in-plane axes (x and y).

Doran *et al*[18] used a rod-type phantom built from three orthogonal inter-penetrating arrays of water-filled tubes placed in an air-filled container. The control points were defined by the center of mass corresponding to the image cross-section of each rod. A typical MR image of a rod-type phantom depicts bright dot regions (water rod signal) on a dark background (no signal from air). The phantom was scanned axially and the resulting images were digitally reformatted to generate three distinct datasets, i.e. transversal, sagittal and orthogonal. To extract the MR location of the control points, the three orthogonal datasets were processed by using a certain image threshold. The distortions along the main axes corresponding to each control point were determined as the average value of the distortions measured from two orthogonal datasets. For example, the x-distortion was calculated as the average value of the x-distortions obtained from the transversal and coronal datasets, respectively.

The determination of control points for registration is not a simple task. Doran *et al*[18] manually generated the reference 3D matrix of CT control points. This is a work-intensive task for routine quality assurance, especially when using a large number of control points (~10000) to maximize the sampling accuracy of the local distortion field. Furthermore, manual identification of the control points can introduce additional user-related errors. Although Wang *et al*[19, 39] did not mention the methods used for extracting the *true* locations of the control points and the registration process of these points with the corresponding MR points, we consider them important and describe our approach in detail in Section 2.2.3.

Another important aspect of the control points identification process is related to the innate properties of 3D MR image datasets. It is recognized that the MR images suffer from various image intensity-related artifacts such as inter-slice intensity variations and smooth intensity variation across the volume.[40-42] These artifacts are due to $\vec{B}_1$ inhomogeneities caused by

variations of the MRI receiver/transmitter coil sensitivity. As a consequence, the intensity-related artifacts can reduce the ability to accurately identify the control points' location. Ideally, these image artifacts need to be corrected before the images are analyzed in the distortion evaluation process. In particular, Wang *et al*[19, 39] used the same intensity threshold to process images obtained by determining the first derivative along *z*-axis and then convolved to a cross mask. Doran *et al*[18] also applied a single intensity level to isolate the dot regions which embed the location of the control points. The use of a unique image intensity threshold might not be suitable for fast and accurate automatic extraction of the control point coordinates due to inherent spatial variation of MR signal intensity.

Doran *et al*[18] determined the local distortion field as the average value of the distortions measured from two orthogonal datasets. This approach represents only the first order approximation of the 3D distortions. Specifically, the evaluation of distortion along a certain axis is affected by the uncertainty in determining the distortion values obtained from the datasets acquired in the other two orientations. Techniques that take into account the mutual interaction among the distortion values along each axis are investigated in this work (see section 2.4).

Our work[20] describes a novel and robust phantom-based method for determining and correcting 3D system-related distortions of MR images. Our method overcomes some of the limitations of previously published works[18, 19] by introducing (a) an adaptive method for the accurate and automatic determination of the control points by compensating for MR image intensity inhomogeneities (see Section 2.2.3), (b) a polynomial fitting-based data cleaning tool that facilitates the automatic registration of the CT and MR control points (section 2.2.4), and (c) an iteration process required to determine the 3D distortion field in the case of methods[18] that rely on the analysis of multiple orthogonal 2D distortion datasets (Section 2.2.4). The algorithm consists of the following main steps: (a) identification, extraction and registration of the CT (*true* location) and MR (distorted) control points and (b) determination of the 3D distortion field by using an iterative process along with an image correction technique.

2.2 MATERIALS AND METHODS

In Fig. 2.1, the flowchart of our distortion correction method is presented. Firstly, phantom data is acquired and inputted into the algorithm. Then the MRI and CT control points are independently identified by applying a set of image processing steps (see Section 2.2.3). The two sets of reference points are registered and the distortion field is determined by using an iteration technique (see Section 2.2.4). Finally, individual images are corrected based on distortion maps.

2.2.1 MR/CT phantom

We used a phantom built similar to Wang *et al*[19] with slightly modified dimensions (see Fig. 2.2a). Specifically, seventeen styrene grid sheets were placed in a 31.8 x 31.8 x 31.5 cm^3 perspex box with a 1 cm thick wall. The grid sheets are equally distributed inside the box with a spacing of 0.9 cm. Each grid sheet is 0.76 cm thick and contains 17 x 17 grid point matrix. The spacing between control points is 1.5 cm along each of the two axes in the grid profile plane. The control points, essential for determining the 3D distortion field, are defined by the intersection of the grid crosses with the imaged plane (see Fig. 2.2b). The effective volume covered by the control points is 260 x 260 x 280 mm^3. Although we used the grid sheet-based phantom design, our distortion correction method is different than the one developed by Wang *et al*[19] (see Sections 2.2.3 and 2.2.4). Specifically, we use a combination of adaptive image thresholding along with an iteration technique to determine the 3D distortion field. In contrast, Wang *et al*[19] and Baldwin *et al*[21] use Prewitt operators to determine the distortion along the main axes. Our procedure can also easily be implemented for a rod-type phantom (e.g. Doran *et al*[18]).

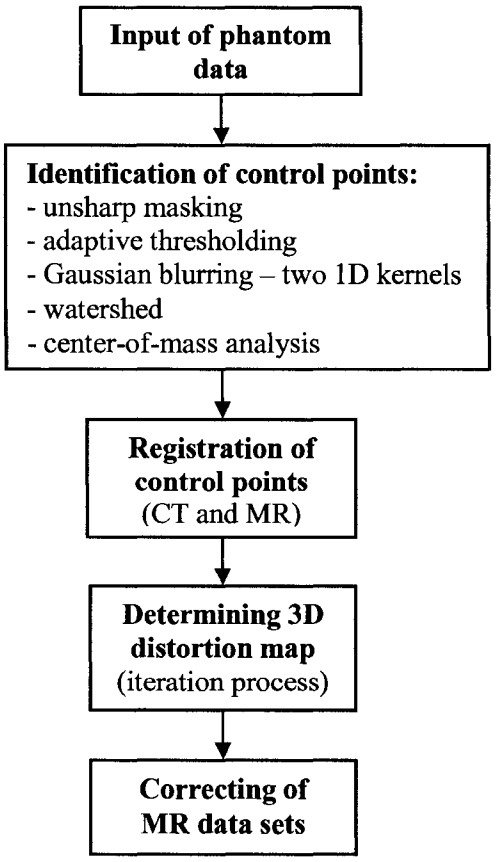

Figure 2.1. The flowchart of the distortion correction method.

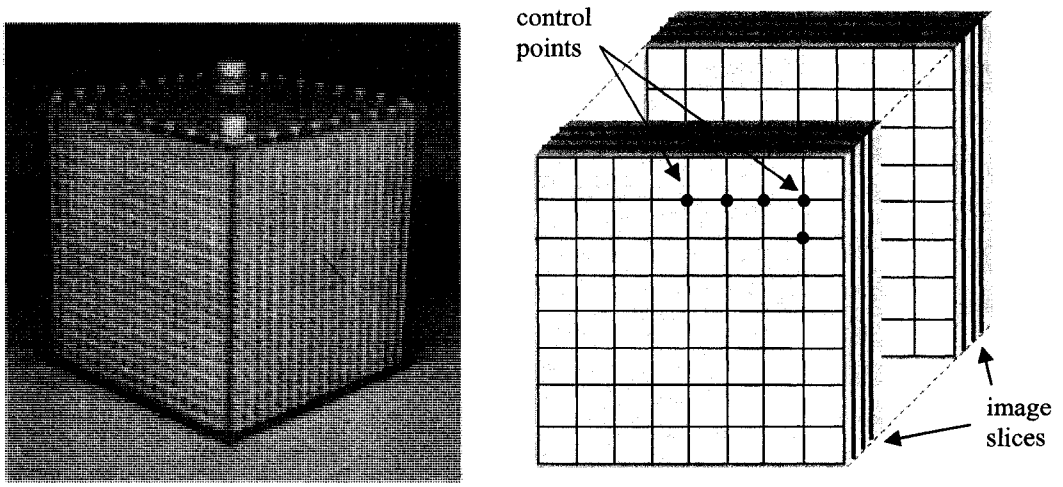

Figure 2.2. a) grid sheets-based phantom design; b) sample of two subsequent grid sheets showing sample control points, i.e. intersection of the grid crosses with the imaged plane, and image slices; the grid sheets are separated by a mineral oil gap.

2.2.2 Data acquisition

MR scanning procedure

The phantom was filled with mineral oil and scanned on a 3 T Intera (Philips Medical Systems, Cleveland, OH) scanner by using a slightly altered (i.e. larger FOV) 3D T1 turbo field echo (TFE) clinical protocol used for diagnostic and treatment planning of glioblastoma multiforme (GBM) patients. The sequence parameters are as follows: TE/TR/α 4.1 ms/8.8 ms/8°, FOV of 450 x 450 mm^2 scanned on a 512 x 512 matrix in-plane, with 251 partitions, each 1 mm thick and no gap. To accurately place the phantom in the scanner bore we built an alignment jig to resemble a flat table within which the phantom fitted tightly. The role of the jig was to minimize positioning errors ($\leq$ 1 mm) between subsequent scans (see below) and to ease the registration process of MRI and CT corresponding data (see Section 2.2.3). The center of the phantom was located near the isocenter of the scanner, i.e. center of the bore.

Our control points' identification method requires that the phantom has 3D symmetry (see Section 2.2.3), i.e. similar structures are displayed along main axes. However, the grid-sheet phantom displays control points only in two dimensions, i.e. the intersections of grid lines. The dimension orthogonal to the grid sheet does not offer control points that are easy to evaluate. Rather, the intersection of grid lines occurs in the dimension orthogonal to the grid sheets for the whole width of one grid sheet (0.76 cm). A typical image cross-section orthogonal to the grid sheets would show dark parallel stripes (grid sheets thickness – no signal) on a light background (oil signal). Therefore, distortion values along the dimension orthogonal to the grid plane were obtained by acquiring two more MR axial scans using exactly the same sequence but with the grid plane oriented in a different orthogonal direction each time. In total, the phantom was imaged three times and was positioned in such a way that the grid profile was parallel to the transverse (x,y), sagittal (y,z), and coronal (x,z) planes, respectively. The scanners' software was used to reconstruct the datasets and visualize the grid structures in the respective planes. The

same datasets were acquired again but with reversed read gradient to account for residual inhomogeneities in the main magnetic field, i.e. $\vec{B}_0$.

CT scanning procedure

For the purposes of this paper, CT scans were assumed to be distortion free. A recent study (Karger *et al*[17]) stressed that the distortions in CT images are usually smaller than 1 mm. During a phantom check CT scan it was observed that some of the grid sheets were significantly warped along the axis orthogonal to the grid profile. This is due to manufacturing imperfections in the commercially available grid sheets. The *true* locations of the control points were therefore obtained from the CT scans, rather than on the nominal design specification of the phantom (Wang *et al*[19]) which could have some construction errors. The phantom was scanned on a Philips Gemini PET/CT scanner (Philips Medical Systems, Cleveland, OH) in the slice-by-slice mode with a 370 x 370 mm^2 field-of-view (FOV), 300 partitions of 1 mm thick each and no gap. The transverse 3D CT scan was reformatted to generate three datasets that would correspond to the MR datasets. To validate the choice of using only the transversal dataset, we measured the gravitational effects on the grid sheets by a) scanning the phantom with the grids orientated in the transverse and coronal planes, and b) identifying similar structures (i.e. grid sheets edges) in the two datasets and measuring their local shift. We found that the maximum difference was within the image pixel resolution (1 x 1 mm^2).

2.2.3 CT and MR control points identification and registration

A method to accurately generate the locations of the reference and distorted control points represents the core of any distortion correction procedure. We determined the 3D distortion field by first assuming that the control points sample properly the volume of interest, and then by

finding the local displacement vector of each control point, namely the difference between its distorted and *true* locations. Any misrepresentation of local distortion values can translate into an incorrect placement of anatomical structures and thus results in a reduced accuracy in delivering treatment dose fractions in RTP.

MR images suffer from various image intensity-related artifacts, e.g. inter-slice intensity variations and smooth intensity variation across the volume[40-42], that affect the accuracy of automatically identifying the control points' coordinates. To address these issues we investigated a standard method suggested by Schmidt[43] and Morris *et al*[44] that is based on applying the Smallest Univalue Segment Assimilating Nucleus (SUSAN) non-linear noise reduction filter and the Nonparametric Nonuniform Normalization (N3)[40] intensity inhomogeneity reduction algorithm.

For our particular case, we found that the noise does not affect the ability of our procedure (see Section 2.2.3) to accurately extract the control point coordinates. By applying different noise reduction filters (i.e. mean, Gaussian, median, and SUSAN) the control points' locations did not change significantly (< 0.1 mm). However, local noise might be an issue for images acquired on scanners with a lower magnetic field strength due to their decreased signal-to-noise ratio (SNR) and/or by using procedures sensitive to this kind of image artifact, e.g. Gaussian fitting.

The MR image intensity variation across the volume decreased significantly by applying the N3 filter[40]. This technique was integrated as an image processing tool in the MNI_N3 software library (McConnell Brain Imaging Centre, McGill University), which is freely available for various flavors of UNIX. However, we chose to use a method that was simpler and easier to integrate in our software package (see below) yet, performed similarly to the N3 algorithm for our particular case of a grid profile. Specifically, either method allowed the accurate identification of the control points. The N3 filter was not used because all our DICOM (i.e. Digital Imaging and Communications in Medicine) image transfer and processing tools

were designed to run under Windows and using the N3 tool would introduce an additional step in the process.

Our method consists of a combination of an unsharp masking step with adaptive thresholding that is individually applied to each image (slice) in the 3D dataset. Once the images are pre-processed to account for image intensity-related artifacts, the control points' coordinates are given by the center of mass of each area located at the intersection of the grid lines which are determined by applying 1D Gaussian blurring kernels along the horizontal and vertical axis, respectively. Our procedure for the identification and the registration of the CT and MR control points is described in detail below. The software was developed in Matlab (The MathWorks, Inc., Natick, MA) and consists of the following steps (see also flowchart in Fig. 1):

(a) The pixel intensities in the MR images (Fig. 2.3a) only are inverted in order to display a bright grid profile on dark background, similar to the CT images. Therefore, the same analysis can be applied for both MR and CT images;

(b) An unsharp masking process which subtracts a strongly Gaussian blurred version of the image from the original one. This step removes low frequency spatial information from the images, highlighting the structures of interest, i.e. the grid pattern (see Fig. 2.3b);

(c) An adaptive intensity threshold based on the image histogram (median) is automatically determined for each image to account for intensity variations across the 3D MR volume. The threshold value was set to be low enough to depict the entire grid structure but sufficiently high to remove inutile information, i.e. background noise. Processed MR and CT sample images are displayed in Fig. 3c;

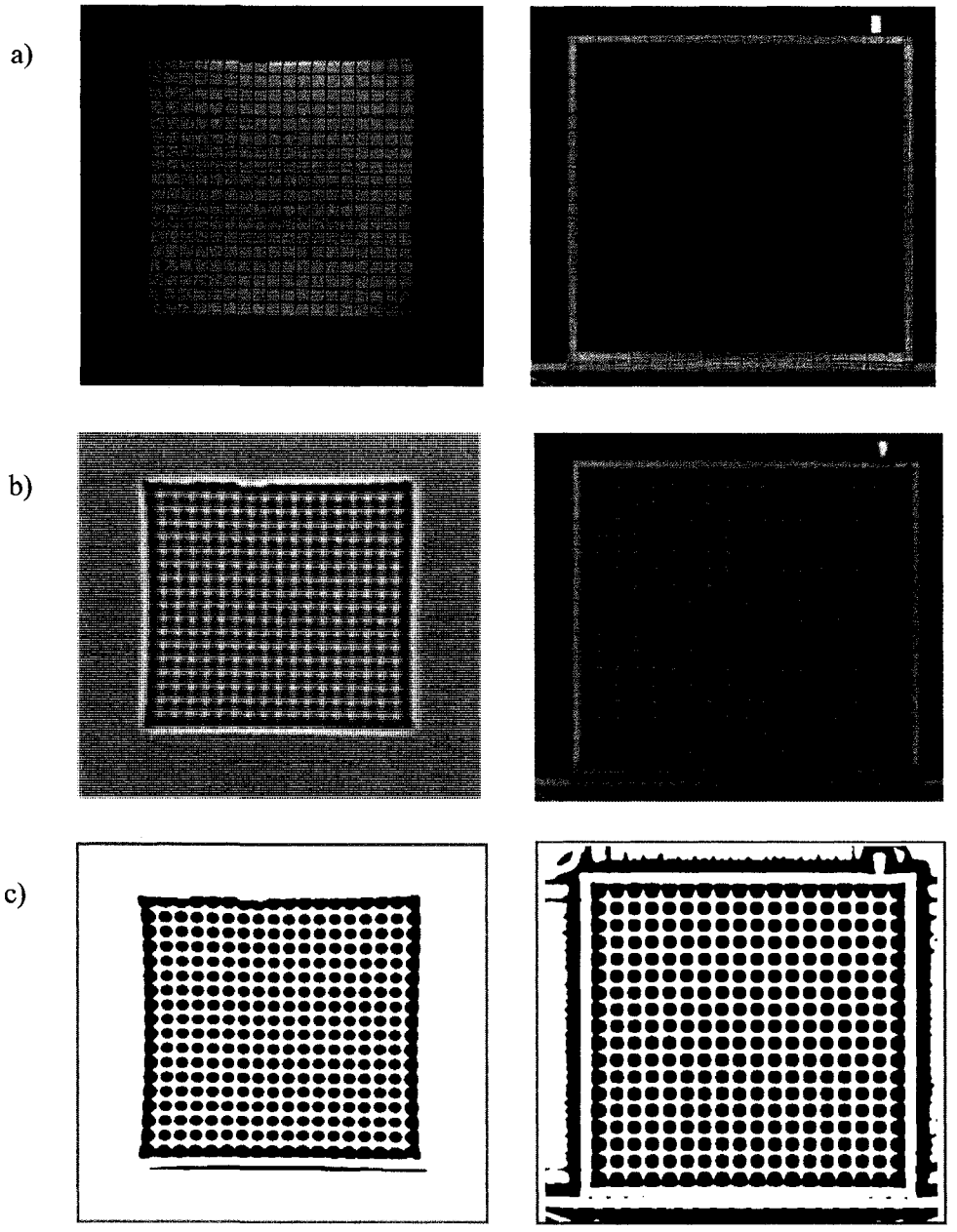

Figure 2.3. The rows present the MR (left) and corresponding CT (right) images: (a) raw images; (b) Gaussian blur and unsharp mask; (c) adaptive threshold.

(d) Once a threshold is selected, two separate image masks are generated: one by applying a 1D Gaussian blurring kernel along the horizontal axis and the other as a result of a similar 1D Gaussian blurring kernel applied along the vertical axis. The two images are summed and only the high intensity pixel areas defined by the intersection of the orthogonal lines are kept resulting in a new image which contains dots at the intersection of the horizontal and vertical lines (see Fig. 2.4);

(e) The dots embed the relative coordinates of the control points; they are separated using a watershed transform and analyzed individually. The watershed is an image segmentation technique which considers the image as being a surface. Individual local minima are regarded as points where water drains from surrounding regions. The transform uniquely index each watershed region;

(f) Areas that contain significantly more or less pixels than pre-defined limits, i.e. number of pixels corresponding to a typical dot embedding a control point (see Fig. 2.4), are discarded as artifacts. This step is particularly important for the CT datasets, which shows the phantom frame and the scanner couch;

(g) The coordinates of each control point are determined from the centre of mass of each dot area (see Fig. 2.4);

(h) As an optional step, the user can visually inspect the accuracy of the algorithm's output, namely the control points can be overlaid on the MR and CT raw images (see Fig. 2.5);

(i) Relative coordinates of the MR and CT control points' are stored and used for registration and 3D distortion field analysis;

(j) For the registration process, the origin was set to be at the isocenter of the MR scanner. The registration of the CT to MR datasets can be described as a 2-step process. First, the CT slice corresponding to slice $z = 0$ in the MR dataset is identified by determining the z-dimension of the CT scan (and/or using fiducial markers). Secondly, the x and y shifts are determined by identifying on the CT central slice ($z = 0$) the control point

corresponding to the MR control point located at the isocenter and by calculating the displacement value between the two. In this process, it was assumed that the magnitude of distortion is negligible near the isocenter of the scanner, a valid premise in the field[18]. The result of the registration process is shown in Fig. 2.6, namely the 3D matrices of both MR and CT control points are given in the system of reference.

The importance of the unsharp mask and adaptive threshold processing steps, i.e. (b) and (c), is stressed by the two sets of image slices displayed in Fig. 2.7. The columns corresponds to images processed by using a unique threshold and by applying steps (b) and (c), respectively. The unique threshold was initially set on the first image (slice *n*), where control points are readily identified by the algorithm (two control points were not resolved due to local inhomogeneities in the image intensity). When moving away from this reference slice (i.e. to slices *n+1* and *n+4*), fewer control points are identified if the same threshold as in the reference slice is used due to further varying image intensity. By subtracting a blurred version of the image (unsharp masking, step (b)) the intensity inhomogeneities are removed from each image. Applying an image-adapted threshold, which accounts for overall variations in pixel intensity between slices (step (c)), leads to accurate identification of all control points present in the images as depicted in the right column of images in Fig. 2.7. Typical image intensity inhomogeneity artifacts removed by applying unsharp masking are shown in Fig. 2.8. The image profile is darker at the center and brighter at the top and bottom edges.

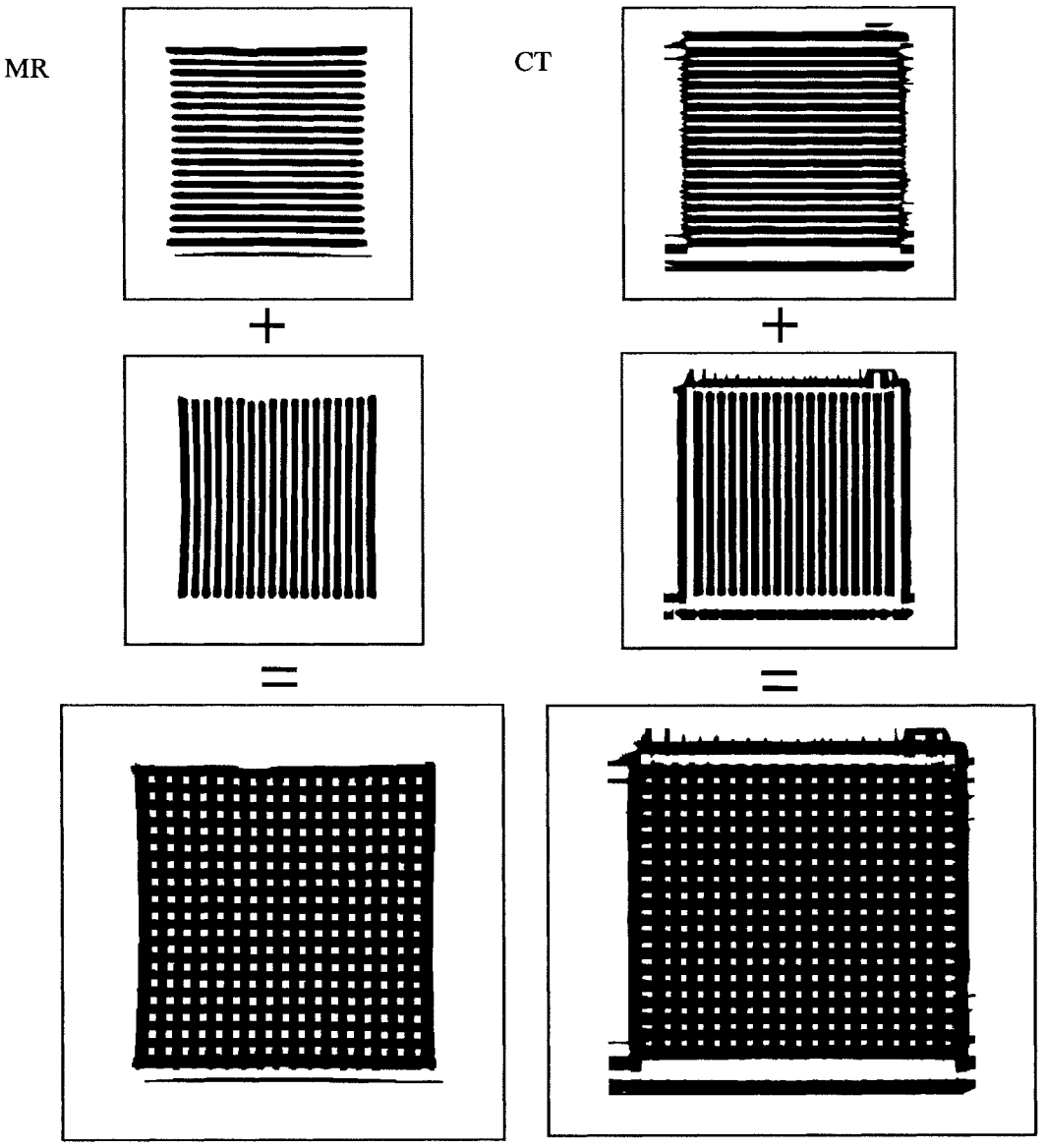

Figure 2.4. 1D Gaussian blur kernels are applied along the orthogonal axes and dot-based images are generated. Each white dot area contains the relative coordinates of the control points.

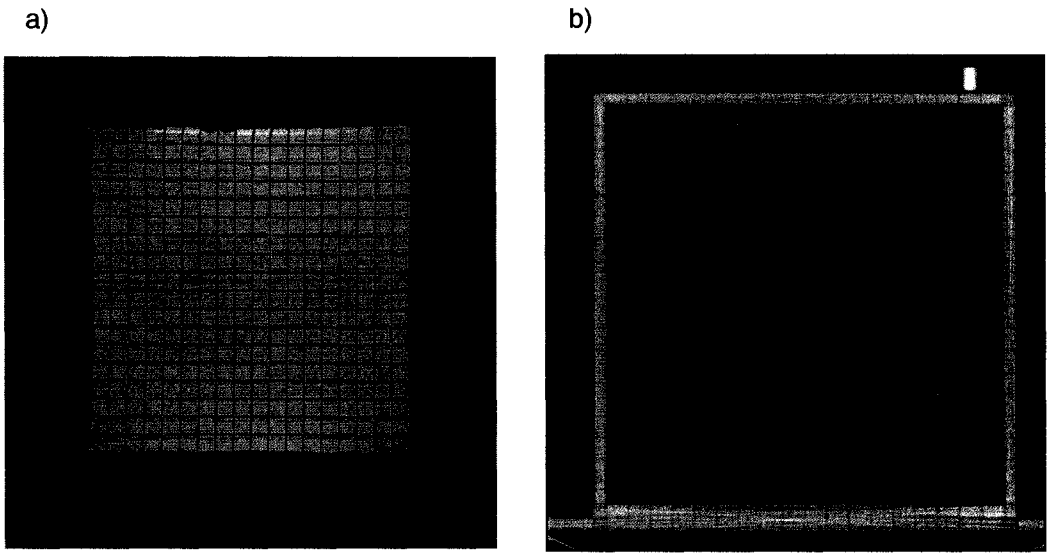

Figure 2.5. The user can visually inspect the accuracy of the algorithm's output. The control points are overlaid on the raw a) MR and b) CT images.

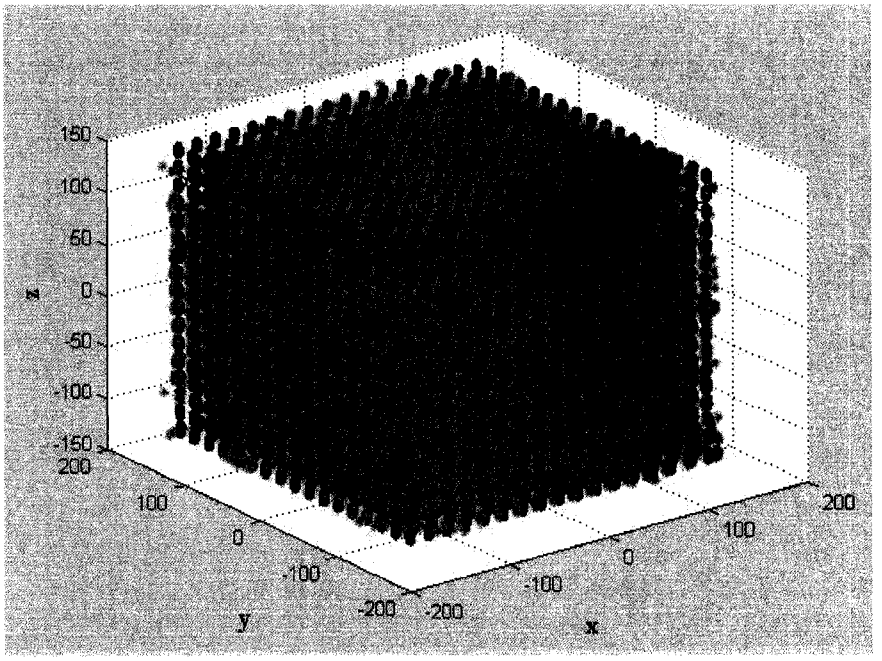

Figure 2.6. Registration of the CT and MR 3 D matrices of control points in the same system of reference; blue and cyan coloured dots correspond to the CT and MR points, respectively.

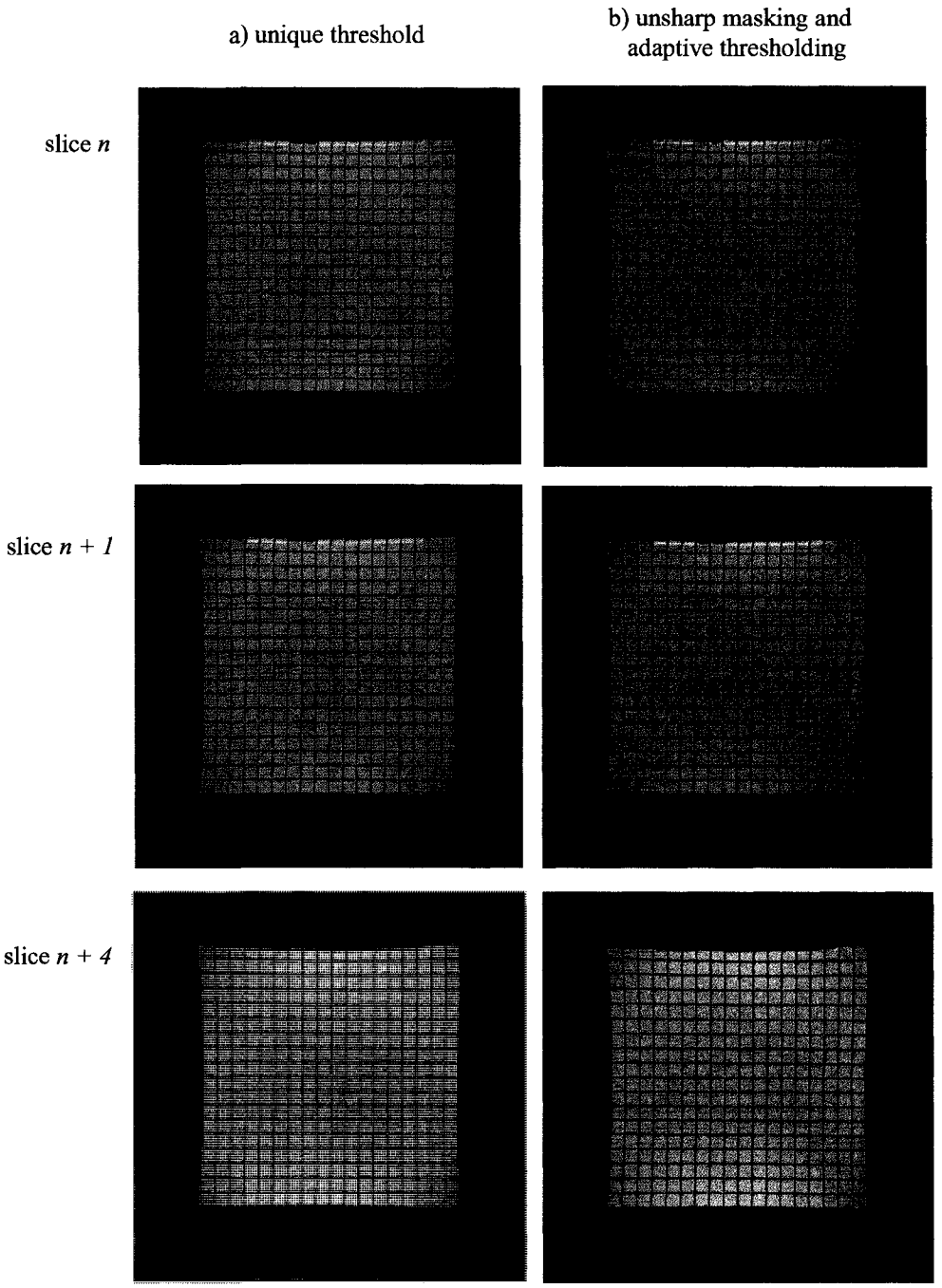

Figure 2.7. Comparison of two techniques used to identify and extract the MR control points: (a) unique threshold for all images - the threshold was set on slice *n* and used subsequently for slices *n+1* and *n+4*; (b) unsharp masking and adaptive thresholding applied to each image.

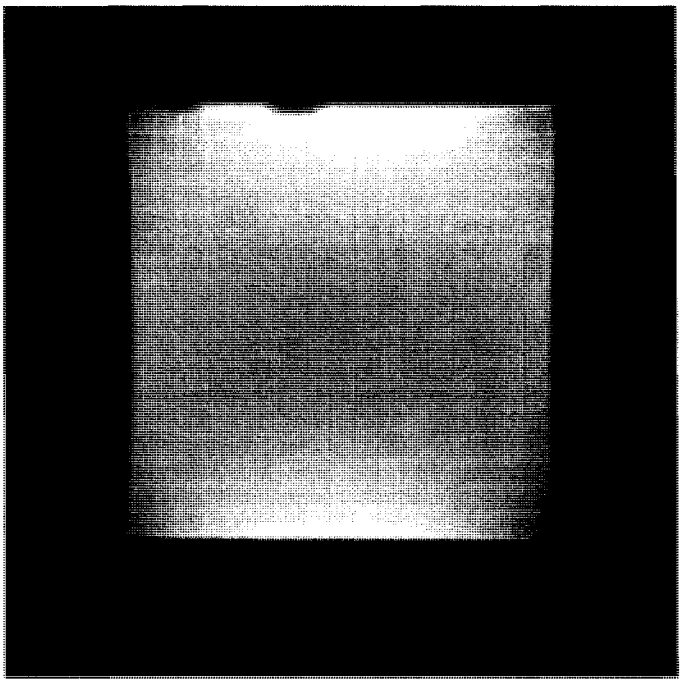

Figure 2.8. Example showing typical image intensity inhomogeneities removed from MR raw images by applying unsharp masking.

2.2.4 Determination of the 3D distortion field

Once the MR and CT 3D matrices of control points are rigidly registered into the same system of coordinates, the 3D distortion field characterized by the local displacement vectors of the distorted points (MR) from their *true* locations (CT) is determined. To accomplish the one-to-one correspondence between CT and MR control points we first considered the undistorted distribution of CT points as being the reference template and then searched in a small region centered around each of these points for corresponding MR ones. This analysis was performed slice-by-slice for the transverse, sagittal and coronal datasets.

Two preliminary steps were performed prior to determining the distortion field. The first step consisted of cleaning the data. Specifically, from the MR image processing stage, residual data (e.g. air bubbles) can generate false control points (< 1% of all control points) that would alter the accuracy of the distortion values. However, this data can be easily filtered out by applying a third order polynomial fitting technique. Several studies[22, 24] aimed to model the distortion field by using 3rd order polynomials. However, we found that the 3D distortion field had a complex behaviour, being characterized by local variations which can not be accurately modelled by using such methods. As a first step we do use the 3rd order polynomials to fit the MR data from each image slice to its corresponding CT data. This was performed by using

$$B_i \cdot A_i = C_i,\ i = 1,...,K \tag{2.1}$$

where K is the number of images, and $B = \begin{pmatrix} b & 0 \\ 0 & b \end{pmatrix}$ with

$$b = \begin{pmatrix} 1 & x_1 & y_1 & x_1y_1 & x_1^2 & y_1^2 & x_1y_1^2 & x_1^2y_1 & x_1^3 & y_1^3 \\ 1 & x_2 & y_3 & x_2y_2 & x_2^2 & y_2^2 & x_2y_2^2 & x_2^2y_2 & x_2^3 & y_2^3 \\ \cdots & \cdots & \cdots & \cdots & \cdots & \cdots & \cdots & \cdots & \cdots & \cdots \\ 1 & x_N & y_N & x_Ny_N & x_N^2 & y_N^2 & x_Ny_N^2 & x_N^2y_N & x_N^3 & y_N^3 \end{pmatrix}$$

The in-plane coordinates of the control points (i.e. CT) are given by (x_j, y_j), where $j=1,...,N$ and N is the total number of control points resolved on each image. The matrices A and C are given by $A^T = (a_{11} \quad a_{12} \quad ... \quad a_{120})$ and $C^T = (u_1 \quad u_2 \quad ... \quad u_N \quad v_1 \quad v_2 \quad ... \quad v_N)$, respectively. They contain the fitting coefficients and MRI control points coordinates, respectively. Vector A is computed from $A_i = B_i^{-1} C_i$, $i = 1,...,K$ by using the least squares method. The polynomial fitting approximates the MR control points positions. By comparing the positions of the MR control points and their corresponding approximate values obtained from the polynomial fitting, we can identify and eliminate spurious control points that lie too far away from the control points defined by the polynomials.

The second step referred to the removal of main field ($\vec{B}_0$) inhomogeneities effects.[18, 30] Namely, the coordinates of each MR control point, corrected for $\vec{B}_0$ inhomogeneities, are given by the average of its location in the corresponding forward and reverse gradient acquired datasets as follows

$$\begin{aligned} x^i &= (x^i_{forward} + x^i_{reverse})/2 \\ y^i &= (y^i_{forward} + y^i_{reverse})/2 \ , \ i = 1,...,N \\ z^i &= (z^i_{forward} + z^i_{reverse})/2 \end{aligned} \tag{2.2}$$

where N is the maximum number of control points.

The local distortion along each axis is determined as the difference between the coordinates of each corresponding MR and CT control point in their common system of reference

$$\begin{aligned}\delta x^i &= x^i_{MR} - x^i_{CT} \\ \delta y^i &= y^i_{MR} - y^i_{CT} \ , \ i = 1,...,N . \\ \delta z^i &= z^i_{MR} - z^i_{CT}\end{aligned} \tag{2.3}$$

In addition, the total distortion corresponding to each control point is given by

$$\delta r^i = \sqrt{(\delta x^i)^2 + (\delta y^i)^2 + (\delta z^i)^2} \ , \ i = 1,...,N . \tag{2.4}$$

Applying Eqs. (2.3) and (2.4) to all three orthogonal datasets (CT and MR), we can find a duplicate estimate of the distortion field along each axis:[18] (a) x and y-distortion from the scans where the grid sheets were oriented along the transverse plane (δx_{tra}, δy_{tra}), (b) y and z-distortion from the scans where the grid sheets were oriented along the sagittal plane (δy_{sag}, δz_{sag}), and (c) x and z-distortion from the scans where the grid sheets were oriented along the coronal plane (δx_{cor}, δz_{cor}). Specifically, the distortion values along the main axes for the i^{th} control point are given by

$$\begin{aligned}\delta x^i_0 &= (\delta x^i_{tra} + \delta x^i_{cor})/2 \\ \delta y^i_0 &= (\delta y^i_{tra} + \delta y^i_{sag})/2, \ i = 1,...,N . \\ \delta z^i_0 &= (\delta z^i_{sag} + \delta z^i_{cor})/2\end{aligned} \tag{2.5}$$

where N is the number of control points used to determine the distortion field. Thus from each of the three measured datasets (grid sheets oriented along the transverse, sagittal and coronal plane, respectively), we assess the in-plane distortion values, with regard to the plane orientation, and evaluate the distortion in the third direction from an orthogonal dataset. However, these quantities represent only an approximation due to the possibility of through-plane distortion.

For each control point the evaluation of distortion along one particular axis is altered by the uncertainty in determining the distortion values obtained from the datasets acquired in the other two orientations. If, for example, the grid planes are oriented in the transverse plane, the x and y distortion values can be obtained for a given MR image slice. However, the z-value (DICOM coordinate of the image slice) assigned by the scanner to that slice might not be the physically correct one, because of possible distortion in the z-direction. We therefore employed an iterative process to determine the *true* values of 3D distortion associated with each MR control point.

To stress the need for an iteration process, the case of only one measured control point (i.e. the coordinates determined as the center of mass of each dot area - Section 2.2.3, step (g)) in the transverse reconstructed dataset is considered (Fig. 2.9). If the MR control point (hollow dot) is located in the initial plane and has no *z*-distortion, then its *true* (in-plane) distortion values are given by δx_0 and δy_0. These values are defined with respect to the coordinates of the CT point (black dot). If, however, the position of the MR control point is also distorted in the *z*-direction, the values obtained initially for it's in-plane distortion might not be the true ones because they depend on the z-coordinate of the plane at which they are measured: $(\delta x_0, \delta y_0)$, $(\delta x_m, \delta y_m)$ and $(\delta x_n, \delta y_n)$ are not necessarily identical. Therefore, δx_0 is only an initial estimate and most likely needs to be re-calculated in a different image plane (*z*-coordinate), thus taking into account distortion in *z*-direction. For example, by correcting the *z*-coordinate for δz_0 in Fig. 2.9 the *x* and *y* distortions now need to be calculated on plane *n* and will likely be different from the ones in the initial plane, i.e. $(\delta x_n, \delta y_n)$. If we had not re-calculated the *x* and *y* distortion in plane *n* and applied the values $(\delta x_0, \delta y_0)$ found in the initial plane to the MR point's position in *x* and *y*-direction in plane *n*, then its new location would be incorrectly given by the gray dot instead of by the black dot in plane *n* in Fig. 2.9. The error in the distortion correction applied would then be $(\delta x_n - \delta x_0, \delta y_n - \delta y_0)$. In the same manner, the new distortion values for *x* and *y*, i.e.

($\delta x_n, \delta y_n$), will affect the corrections that result for the distortion in the (y,z) and (x,z) planes, respectively.

The iterative process we developed in order to find the 3D distortion values is applied to each MR control point. For the ith control point defined by the coordinates (x^i, y^i, z^i), the initial estimate of distortion is given by ($\delta x_0^i, \delta y_0^i, \delta z_0^i$) from Eq. (2.5). The iteration process starts with the x-coordinate. To find δx_1^i, the new estimate of x-distortion, we account for the initially found distortions in y and z, by applying the δy_0^i and δz_0^i shifts to the ith control point. These shifts generally move the control point to a location in between the measured control points coordinates. Therefore, δx_1^i is determined at the location $(x^i, y^i + \delta y_0^i, z + \delta z_0^i)$ by interpolation of the x-distortion values of neighboring measured control points. In general, the x-distortion value in the nth iteration is a function of the y and z distortions determined in the (n-1)th iteration:

$$\delta x_n^i = \delta x_n^i(x^i, y^i + \delta y_{n-1}^i, z^i + \delta z_{n-1}^i),\ i = 1,...,N,\ n > 0\,. \tag{2.6a}$$

where n is the iteration index. The value of δx_1^i is subsequently used to estimate in turn the distortions along the y and z axes. Specifically, the new estimate of y-distortion, i.e. δy_1^i, is determined using a similar relation as Eq. (2.6a) after applying the δx_1^i and δz_0^i correction shifts: $\delta y_1^i = \delta y_1^i(x^i + \delta x_1^i, y^i, z^i + \delta z_0^i)$ or in general

$$\delta y_n^i = \delta y_n^i(x^i + \delta x_n^i, y^i, z^i + \delta z_{n-1}^i),\ i = 1,...N,\ n > 0\,. \tag{2.6b}$$

Similarly, the z-distortion δz_1^i is evaluated at the location corrected for δx_1^i and δy_1^i as $\delta z_1^i = \delta z_1^i(x^i + \delta x_1^i, y^i + \delta y_1^i, z^i)$ or in general

$$\delta z_n^i = \delta z_n^i(x^i + \delta x_n^i, y^i + \delta y_n^i, z^i),\ i = 1,...,N,\ n > 0. \tag{2.6c}$$

Once the first iteration values $(\delta x_1^i, \delta y_1^i, \delta z_1^i)$ are calculated, the need for a further iteration is determined by using

$$\begin{aligned} &\left|\delta x_n^i - \delta x_{n-1}^i\right| < \varphi \\ &\left|\delta y_n^i - \delta y_{n-1}^i\right| < \varphi,\ i = 1,...,N,\ n > 0. \\ &\left|\delta z_n^i - \delta z_{n-1}^i\right| < \varphi \end{aligned} \tag{2.7}$$

where φ is the iteration cutoff threshold. If at least one of the conditions (2.7) is not fulfilled the process initiates an additional iteration. The process stops when conditions (2.7) are satisfied simultaneously. The final $(\delta x^i, \delta y^i, \delta z^i)$ distortion values are given by Eqs. (2.6), using the shifts determined in the last iteration. The convergence of the iteration process is discussed in Section 2.3. Once the distortions of each control point are determined, distortion maps can be generated at any location in the volume using interpolation methods (spline interpolation in our case). To validate our distortion correction method the residual geometric distortions were determined, i.e. the local distortion values after re-running the distortion correction algorithm by using the rectified images (Section 2.2.5) as input.

Figure 2.10 shows a sample vectorial distribution of the distortion field in the transverse plane. As expected, the distortion increases as we move further away from the isocenter.

The maximum absolute distortion along the *x*, *y*, and *z* axes are defined as

$$\begin{aligned} \delta x &= \max(\left|\delta x^i\right|) \\ \delta y &= \max(\left|\delta y^i\right|),\ i = 1,...,N \\ \delta z &= \max(\left|\delta z^i\right|) \end{aligned} \tag{2.8}$$

where δx^i, δy^i, and δz^i are given by Eqs. (2.6), and N is the total number of reference points used to determine the 3D distortion field. In addition, the total maximum absolute distortion is given by

$$\delta r = \max\left[\sqrt{(\delta x^i)^2 + (\delta y^i)^2 + (\delta z^i)^2}\right], \; i = 1,\ldots,N \tag{2.9}$$

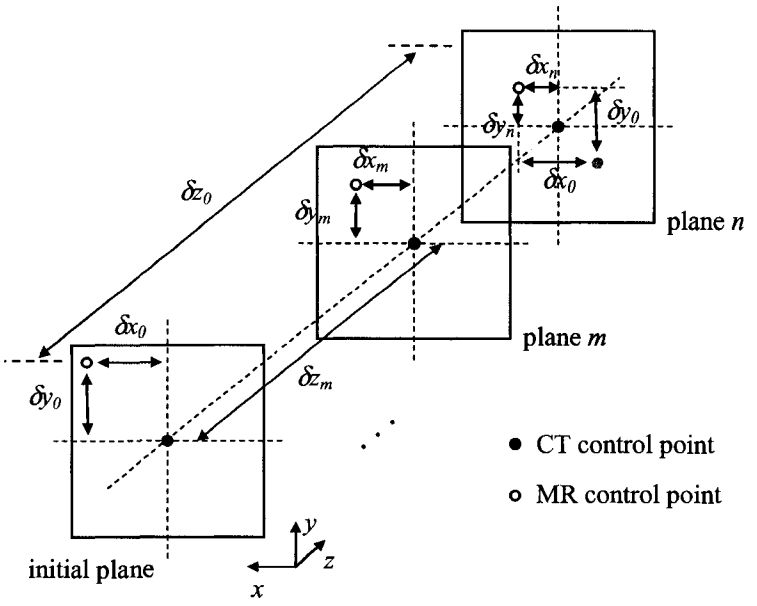

Figure 2.9. The distortion values corresponding to the MR control point (hollow dot) may vary depending on its z-location. Using the initial estimates of distortion given by Eqs. (2.5), i.e. δx_0, δy_0 and δz_0, we might end up over-correcting the position of the MR point. Specifically, the location of the MR point would be given by the gray dot (not the CT point – black dot). In our data sets, spacing between subsequent image slices (here in z-direction) was 1 mm.

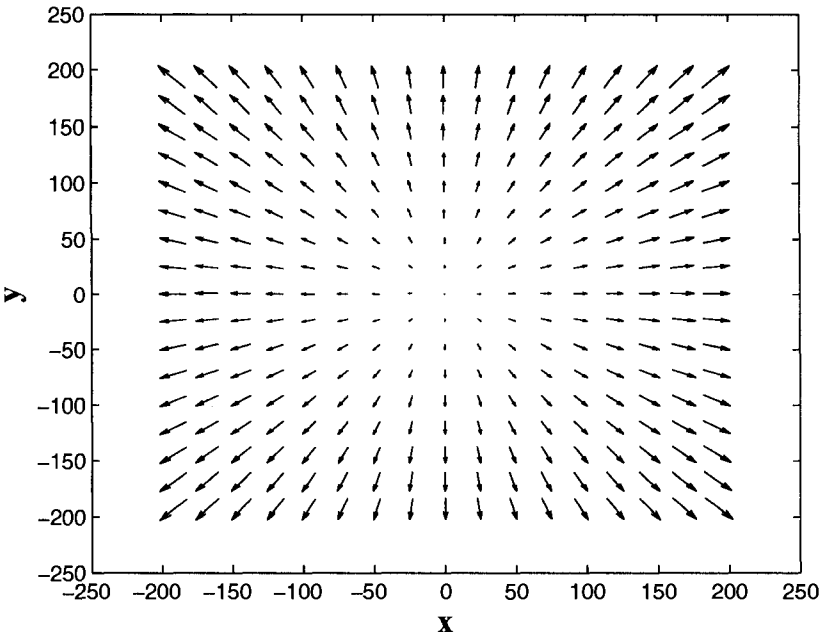

Figure 2.10. Sample 2D vectorial distribution of the distortion field.

2.2.5 Image correction

Once the distortion values along each axis (δx, δy, δz) are found, the MR images are corrected by applying spatial and pixel intensity interpolations (see Fig. 2.11). Specifically, each pixel in the distorted image is shifted to its true position as given by the measured distortion map. To accurately account for the local variation of the 3D distortion field we investigated two distinct types of image transformations available in Matlab, namely (a) global, including polynomial (i.e. 3^{rd} and 4^{th} orders), and (b) local, given by piecewise linear and local weighted mean methods. In the global transformations a single mathematical expression is applied to the entire image whereas for the local transformations different expressions are applied to distinct regions within the same image. It was found that the local weighted mean-based transformation performed best. This technique relies on inferring a 2^{nd} order polynomial to each control points pair by using the closest 12 neighboring control points. The local mapping depends on the weighted average of these polynomials, which is automatically performed in Matlab. Appendix A.5 gives a brief presentation of the local weighted mean (lwm) technique. The lwm method was implied as a faster alternative of the point-by-point image transformation given by the MRI-CT pairs of control points. Once the lwm mapping is performed it is subsequently used to unwarp the images by applying a bicubic convolution interpolation algorithm (see Appendix A.6).

In the process of correcting patient images we have to consider that the center of the images (when data is acquired) does not necessary coincide with the isocenter of the scanner. Therefore, we first determine the shift between the two before generating distortion maps. This can be found, for our 3 T Intera scanner, from the DICOM header of the patient dataset as follows

$$
\begin{aligned}
x_{shift}^{iso} &= \frac{FOV}{2} - x_{DICOM} \\
y_{shift}^{iso} &= \frac{FOV}{2} - y_{DICOM} \\
z_{shift}^{iso} &= z_{DICOM}
\end{aligned}
\tag{2.10}
$$

where x_{shift}^{iso}, y_{shift}^{iso} and z_{shift}^{iso} represent the shift values along the main axes, FOV is the field of view used to acquire the dataset and x_{DICOM}, y_{DICOM} and z_{DICOM} are the coordinates obtained from the DICOM header.

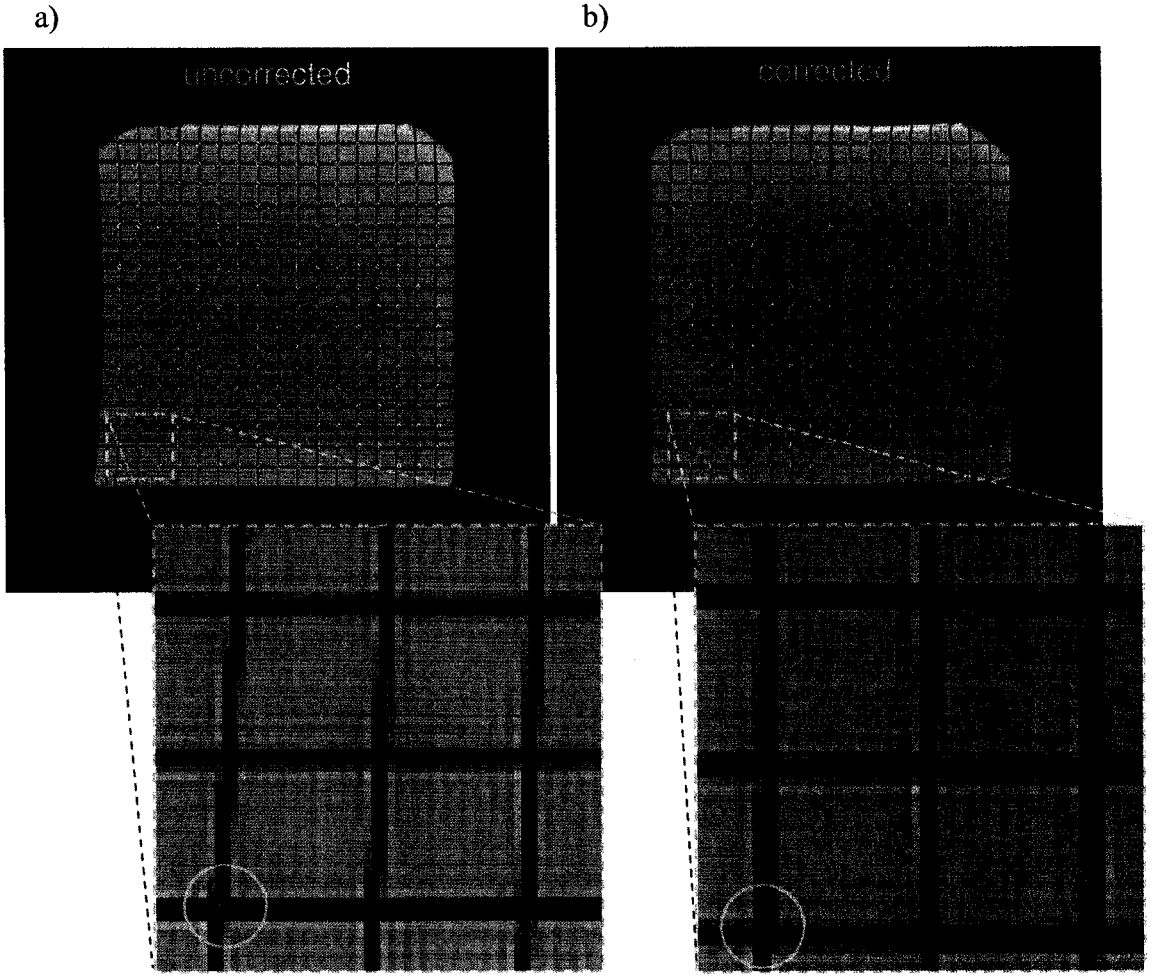

Figure 2.11. Illustration of the image correction process. Green and cyan dots represent the CT (true location) and MR (distorted) location of the control points. In a), the uncorrected image, the grid points are given by the MR control points. After corrected the image, the grid points are defined by the CT reference points as shown in b).

2.3 RESULTS AND DISCUSSION

The MR image intensity-related artifacts were overcome by applying a technique based on a combination of an unsharp masking with adaptive thresholding that was applied to all images in the 3D datasets. This is critical for automatic and accurate determination of all control points corresponding to each image. In contrast, by choosing a unique threshold to be applied to the entire dataset, the number of control points retrieved automatically is a maximum for slices close to the one used to define the threshold and decreases with increasing distance from the defining slice (Fig. 2.7). Further manual identification of control points is required, which can introduce additional user-related errors. In particular, the method developed by Wang *et al*[19, 39] is sensitive to the number of control points resolved in each image. Specifically, the magnitude of distortion along z-axis is strongly correlated to the ability of detecting the control points in all images corresponding to each grid-oil interface. Not correcting for local image intensity inhomogeneities and intensity variations across the 3D volume (by using a unique threshold) can result in missing control points that might lead to a misrepresentation of the distortion values. Doran *et al*[18] also applied a unique image intensity level to isolate pixel clusters that embed the location of the control points on a 2D grid.

The oil-filled phantom may contain air bubbles that can misrepresent the actual dot area (i.e. air bubbles next to grid points) and can also generate false control points in between subsequent grid points (air bubbles in the mineral oil). This is a common problem with fluid-filled phantoms. Techniques based only on applying a threshold to resolve the control points are likely to produce additional (spurious) control points that can corrupt the accuracy of the distortion maps. The approach we implemented in Section 2.2.3 is insensitive to the artifacts related to the presence of air bubbles as it eliminates any image data except the areas located at the intersection of the orthogonal grid lines. Over the entire volume of interest (VOI) analyzed, i.e. 260 x 260 x 240 mm^3, the CT and MR control points can be identified by our algorithm

within one voxel, i.e. 0.9 x 0.9 x 1 mm^3, from their true location. This was determined by overlaying the control points on the raw images.

The 3D distortion field was determined by using the iteration process described in Section 2.2.4. By comparison, Doran *et al*[18] method represents the first order approximation of the distortion field. Specifically, the distortion of each MR control point along the main axes was determined as the average value of the distortions measured from two orthogonal datasets as given by Eqs. (2.5). Each of the two distortions estimates along the main axes (see Eqs. (2.5)) agreed within 1 mm. In our technique Eqs. (2.5) are used as a starting point of the iteration process (see Section 2.2.4).

Sample distortion maps corresponding to the image plane located at z = 87 mm from the isocenter are displayed in Fig. 2.12. To have a better understanding of the distortion field distribution across the 3D volume, Fig. 2.13 shows as solid lines the maximum absolute distortion in each image plane along z axis. For all curves, the distortion values increased towards the edges of the FOV. The curves corresponding to the total maximum distortion before and after applying the distortion correction, i.e. $\max(\delta r)$ and $\max(\delta r_{resid})$, are also shown. The maximum distortion in the 260 x 260 x 240 mm^3 volume was found to be 5.55 mm. After correcting the images the maximum residual distortion was determined to be 0.55 mm, which is less that the image voxel (i.e. 0.9 x 0.9 x 1.0 mm^3). A detailed summary of statistical data (i.e. mean (μ), standard deviation (σ) and maximum (*max*)) of the distortion found and the residual distortion is presented in Table 2.1.

In Fig. 2.13 the dashed lines represent the difference between the maximum distortion along the main axes obtained with our iterative method and the first order approximation (Doran *et al*[18]). The maximum total difference was found to be about 1.2 mm corresponding to the FOV edges. For the central region of the FOV the maximum total difference is within 0.5 mm. Furthermore, the data in Table 2.1 show that the maximum residual distortion after applying only

the first order approximation is 1.54 mm, which is significantly greater than the image voxel size. This implies that the iterative method needs to be applied for a more accurate characterization of the 3D distortion field. It should be noted that the iterative method shows its greatest advantage compared to the method of Doran *et al*[18] at the edges of the FOV. It can be reasonably expected that this advantage is even more pronounced for larger volumes (e.g. prostate studies) because the accuracy of the initial distortion estimate decreases as the distortion field gradient increases with distance from isocenter[18] and the correction of through plane distortion (with regard to each orthogonal plane) becomes more important. We are planning to further investigate this issue by using a new, wider phantom that can sample the MRI bore more completely and eventually allow the MRI-based RTP of larger volumes.

Regarding the behavior of our iteration process, it converges due to a slow local variation of the distortion values $(\delta x, \delta y, \delta z)$ corresponding to each control point. With every iteration step, the difference between two consecutively determined distortion values decreases until this difference is comparable to the iteration cutoff threshold, which was chosen to minimize the residual distortion (i.e. $\varphi = 0.2$ mm). We determined that a further reduction in the φ value does not result in an improvement of the residual distortion. To detect lack of convergence of our algorithm we monitor the residual distortion. Lack of convergence is defined as a residual distortion greater than the values obtained from the initial estimation (Eqs. (2.5)). If the iteration results had exceeded those values, the iterative method had failed and the algorithm would then use those initial values as the resulting distortion values. However, this case was never observed in our tests. For our particular case (scanner type, imaging sequence, VOI size, etc), the maximum number of iterations required for the algorithm to converge was 4. Near the periphery of the VOI, depending on the magnitude of distortions, certain amount of data is required from outside the mapped field (VOI). This data can be easily obtained through interpolation (in our case - spline interpolation).

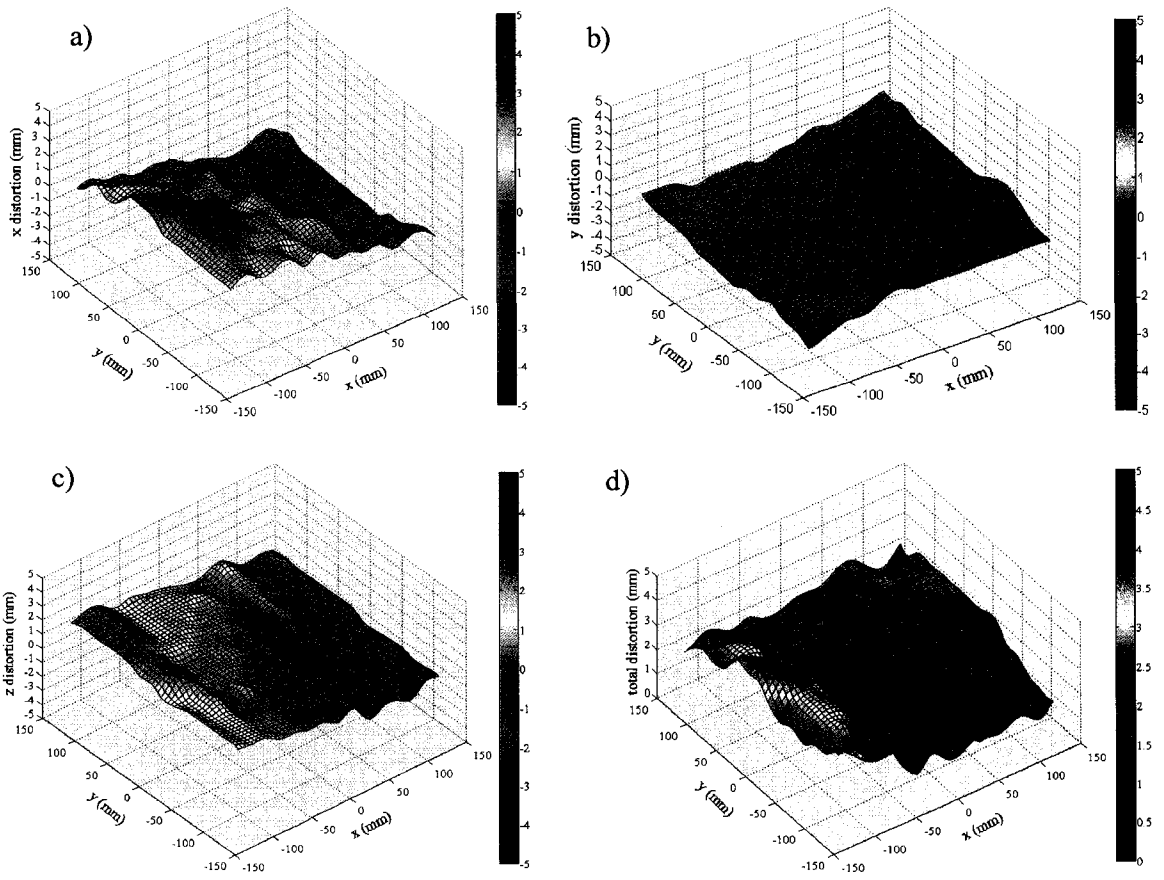

Figure 2.12. Sample distributions of (a) δx, (b) δy, (c) δz, and (d) δr corresponding to slice z = 87 mm (Note that the total distortion plot has a different colour bar scale.)

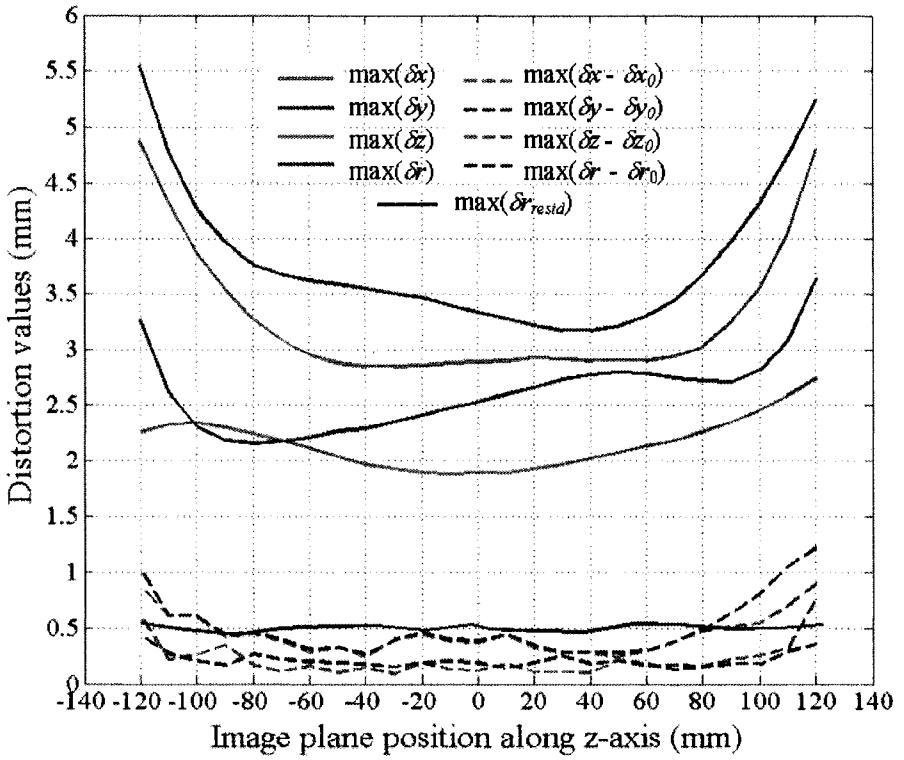

Figure 2.13. Distortion as a function of image plane location along z-axis - solid lines give the maximum absolute distortion along the main axes ($\max(\delta x), \max(\delta y), \max(\delta z)$). The effect of our distortion correction procedure is evident by comparing the total maximum distortion before and after applying the distortion correction ($\max(\delta r)$, $\max(\delta r_{resid})$). The dashed lines show the advantage of our iteratively found distortion values over the ones found by using only an initial estimation of the distortion according to Eqs. 2.5; the absolute difference between the two methods is displayed.

Distortion correction method	axis	Distortion found for the MR data set			Residual distortion after correcting the MR data set		
		Mean μ (mm)	Standard deviation σ (mm)	max (mm)	Mean μ (mm)	Standard deviation σ (mm)	max (mm)
1st order estimation (Doran *et al*[18])	*x*	1.45	0.43	5.84	0.15	0.08	0.96
	y	1.13	0.34	4.49	0.91	0.04	0.53
	z	1.10	0.13	3.55	0.21	0.09	1.22
	r	2.25	0.56	6.70	0.25	0.14	1.54
Iterative process (our work)	*x*	1.31	0.32	5.07	0.07	0.03	0.36
	y	0.76	0.26	4.05	0.04	0.02	0.20
	z	0.76	0.07	2.65	0.07	0.03	0.38
	r	1.86	0.41	5.55	0.14	0.05	0.55

Table 2.1. Summary of statistical data. The average, standard deviation and maximum values refer to the displacement of the MR control points relative to the CT control points. The values quoted are the ones obtained by applying the 1st order distortion (Eqs. (2.5)) and using our iterative approach to finding the distortion map. The volume covered by our phantom was 260 x 260 x 240mm^3. The maximum difference between the case of applying the iterative method as compared to using only the initial distortion estimate (Eqs. (2.5)) is 1.2mm. This difference is expected to increase for larger volumes (e.g. prostate studies) as the distortion field gradient increases with distance from isocenter.

Therefore, in these regions, the algorithm does not diverge due to lack of information. The outcome of the iteration process is not significantly dependent on the spatial coordinate used as a starting step (x, y or z): the maximum difference between different scenarios (e.g. x, y or z first) was within 2%.

It is useful to evaluate the maximum absolute deviations corresponding to various spherical volumes as it is shown in Fig. 2.14. This is of particular interest for our MR-based treatment planning procedure applied to intracranial lesions[7-10] as the skull volume can be approximated with a sphere. The total distortion for a typical brain study, i.e. 10 cm radius, is about 4 mm suggesting that the MR brain images need to be corrected before being used in the treatment planning process.

In Fig. 2.15, the first and the second row show sample images of the phantom from the transverse and sagittal reconstructed datasets. The first two columns represent the uncorrected images and the same image after applying our image correction method. The third column displays the difference of the uncorrected and corrected images. The distortions along all three axes are clearly visible in these images. As expected, the magnitude of distortion is largest at the corners of the images. The residual geometric distortions determined after correction are negligibly small, being within one pixel resolution, i.e. < 1 mm. As an example, Fig. 2.16 shows the total residual distortion map corresponding to Fig. 2.12d, i.e. the image plane located at z = *87* mm.

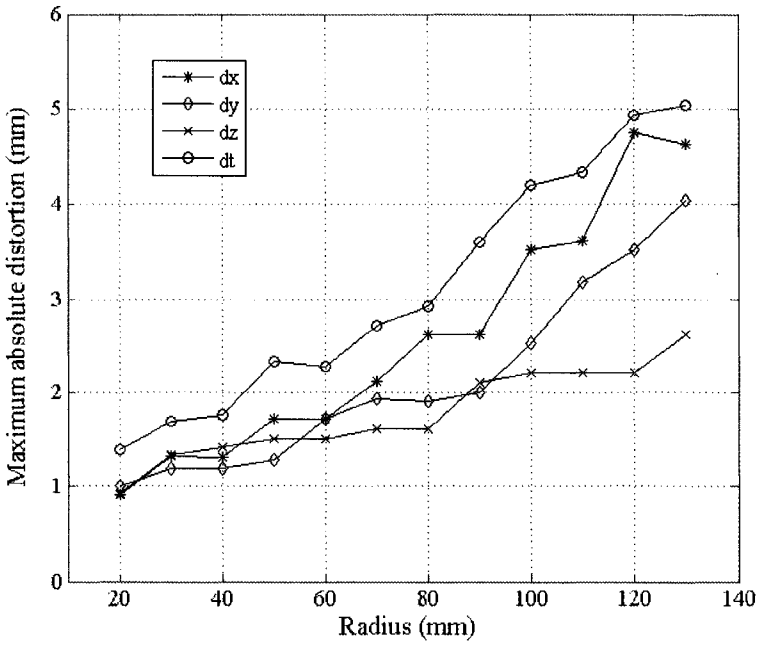

Figure 2.14. Maximum absolute distortion measured in a spherical volume with the radius varying from 20 mm to 130 mm.

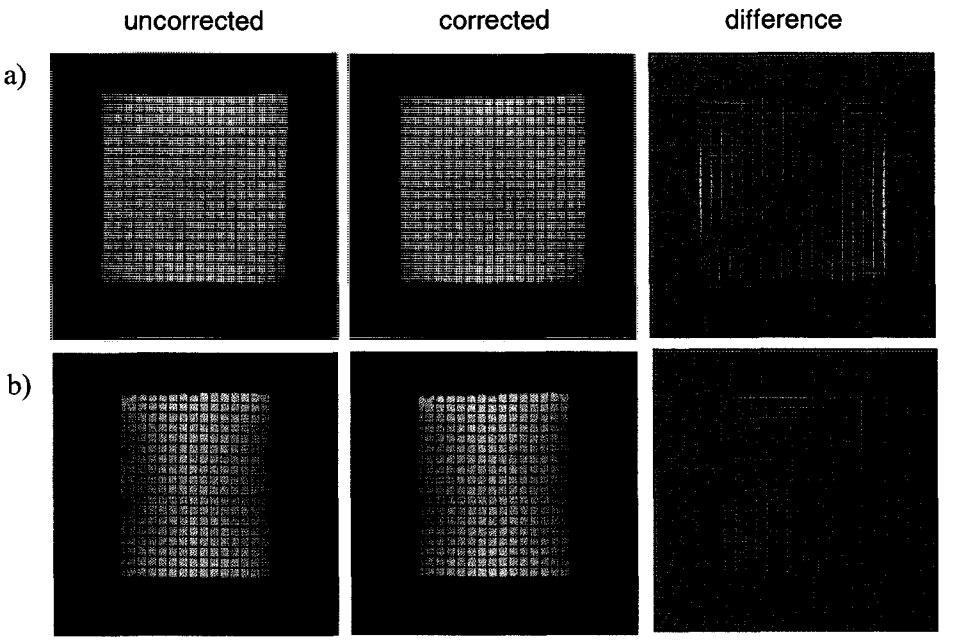

Figure 2.15. A sample image of the phantom in (a) transverse and (b) sagittal reconstructed dataset; the columns represent: uncorrected, corrected and difference of the two images.

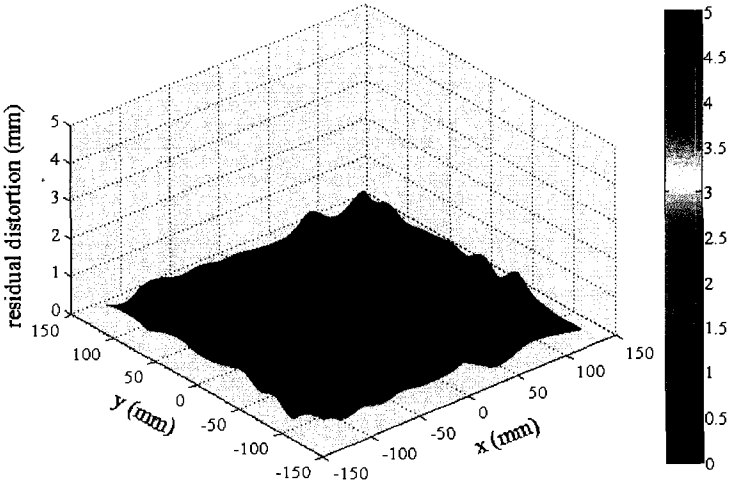

Figure 2.16. Total residual distortion for the image plane located at $z = 87$ mm. (Note: The total distortion map of this image plane is displayed in figure 2.12d.)

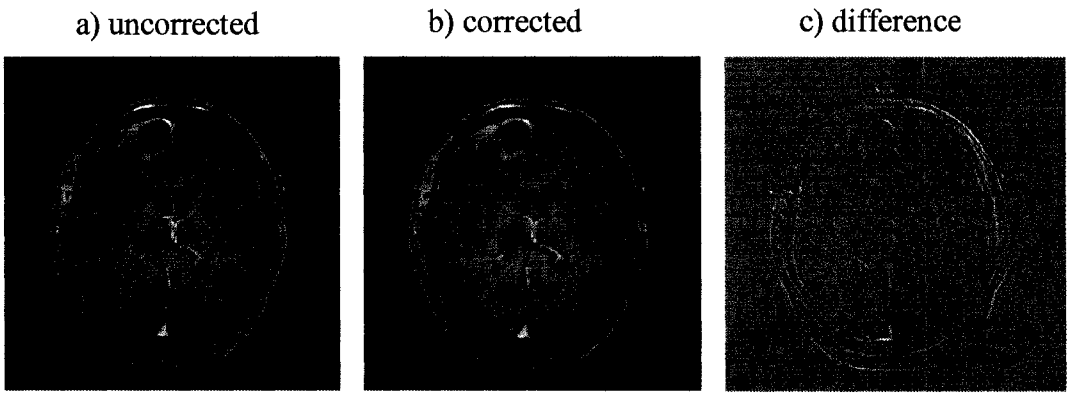

Figure 2.17. A sample MR image slice of a radiation therapy GBM patient: a) raw image, b) same image slice corrected using the distortion map determined using our procedure and c) the difference of the two.

Figure 2.17 shows a sample MR image slice of a radiation therapy GBM patient: a) raw image acquired from the scanner, b) same image slice corrected using the distortion map determined using the method presented in this work and c) the difference between the uncorrected and corrected images. The distortion correction method was implemented as a necessary step in our MRI-based treatment planning procedure.[7-10]

Wang *et al*[39] also investigated VOIs relevant to brain studies and claimed a mean residual error in the measured control points' coordinates as being between 0.1 and 0.2 mm. We obtained similar values by applying our method, i.e. 0.14 mm. In both cases, measured distortion is below the pixel resolution. However, it is difficult to compare the details of our method with the work of Wang *et al*[39] as the latter study did not address some aspects typically present in a distortion correction process such as: (a) the process of generating the 3D matrix of true (i.e. correct) location of the control points, (b) the registration of corresponding true and distorted locations of control points and (c) the correction of MR image intensity artifacts. Our results are also in good agreement with the study of Baldwin *et al*,[21] which investigated the system-related distortions by

applying the Wang *et al*[39] technique. Specifically, Baldwin *et al*[21] reported that mean residual distortion (standard deviation) was 0.28 (0.15) mm.

Doran *et al*[18] used a phantom built from three orthogonal inter-penetrating arrays of water-filled tubes placed in an empty box. One possible limitation of this design is that the tube-air interface might generate large susceptibility effects leading to an altered accuracy in determining the distortion field. Regarding the control points identification process, the reference 3D matrix of CT control points was generated manually. This is a laborious task from a routine quality assurance perspective, especially when using a large number of control points (~10000) to maximize accuracy. Manual identification of the control points might also introduce user-related errors. Furthermore, Doran *et al*[18] determined the distortion along each axis as being the average of distortion values estimated from two orthogonal planes. As discussed in Section 2.2.4, this approach represents only an approximation of the distortion values because the mutual interaction among the distortions along each spatial dimension is not accounted for. An iteration process would be needed for a complete quantification of the 3D distortion field. Also, another limitation of Doran *et al*[18] work is that the authors performed the analysis on image data with a voxel resolution of 1.88 x 1.88 x 5 mm^3. Thus, the resolution in the slice selection direction was quite large making the evaluation of the distortion field difficult. In our case, the data was acquired with a resolution of 0.9 x 0.9 x 1 mm^3. Due to this fact, we expect that our analysis was more accurate than the one of Doran *et al.*[18]

The novelty of the method developed here consists of: (a) adaptive technique for the accurate and automatic identification and extraction of the control points' location by compensating for MR image intensity inhomogeneities, (b) data cleaning tool based on polynomial fitting that facilitates the automatic registration of the CT and MR control points and (c) iteration process required to determine the 3D distortion field when applied to methods that incorporate multiple orthogonal 2D distortion datasets.[18] Our method can be implemented by

using either grid sheets or rod-type phantoms (the most common designs), unlike other approaches that are dependent on the phantom type.[39] This would allow the use of the most cost efficient phantom design. In the case of a grid sheets-based design (used in this work) three scans are required (see Section 2.2.2) due to phantom's limited 2D symmetry. However, in the case of the 3D rod type phantom[18] one scan is enough to acquire all the data. This would be the preferred approach as the distortion correction procedure would be significantly simplified, i.e. reduced data acquisition and image processing time.

2.4 CONCLUSIONS

We developed a procedure for measuring and correcting scanner-induced geometric distortions in MR images that consists of two key components: an adaptive control points' identification and registration tool and an iterative algorithm that calculates the best estimate of 3D distortion.[20]

It was found that over a volume of 260 × 260 × 240 mm^3 the 3D distortions can be successfully mapped to within the voxel resolution of the raw imaging data. Namely, the total maximum distortion was found to be 5.55 mm with a μ and σ of 1.86 mm and 0.41, respectively. After applying the image correction algorithm the residual distortion metrics were 0.55 mm/0.14 mm/0.05, respectively. The iterative approach taken in this work becomes increasingly important as the FOV is widened.

The procedure was developed and integrated as an automatic tool in our MRI-based treatment planning procedure for intracranial lesions.[7-10] Brain 3D MR image datasets need to be corrected for system-related distortions before they are converted into CT-like images and used for dose calculations. Any misrepresentation of distortion values can lead to an incorrect placement of anatomical structures and thus results in a reduced accuracy in delivering treatment dose fractions in RTP.

2.5 REFERENCES

1. Thorton A, Sandler MD, Ten Haken RK, McShan DL, Fraas BA, LaVigne ML, Yanke BR. The clinical utility of magnetic resonance imging in 3-dimensional treatment planning of brain neoplasms. *Int J Radiat Oncol Biol Phys* 1992;24:767-775.
2. Heester M, Wijrdeman HK, Strukmans H, Witkamp T, Moerland MA. Brain tumor delineation based on CT and MR imaging. *Strahlenther Onkol* 1993;169:729-733.
3. Sultanem K, Patrocinio H, Lambert C, Corns R, Leblanc R, *et al.* The use of hypofractionated intensity-modulated irradiation in the treatment of glioblastoma multiforme: preliminary results of a prospective trial. *Int J Radiat Oncol Biol Phys* 2004;58:247-252.
4. Roach M, Faillace-Akazawa P, Malfatti C, Holland J and Hricak H. Prostate volumes defined by magnetic resonance imaging and computerized tomographic scans for 3-dimensional conformal radiotherapy. *Int J Radiat Oncol Biol Phys* 1996;35:1011-1018.
5. Kagawa K, Lee WR, Schultheiss TE, Hunt MA, Shaer AH and Hanks GE. Initial clinical assessment of CT-MRI image fusion software in localization of the prostate for 3D conformal radiation therapy. *Int J Radiat Oncol Biol Phys* 1997;38:319-325.
6. Rasch C, Barillot I, Remeijer P, Tpuw A, van Herk M and Lebesque JV. Definition of the prostate in CT and MRI: a multi-observer study. *Int J Radiat Oncol Biol Phys* 1999;43:57-66.
7. Stanescu T, Syme A, Pervez N and Fallone B G. MRI-based treatment planning for radiotherapy of brain lesions. [Abstract]. *Med Phys* 2005;32:2033.
8. Stanescu T, Jans H-S, Stavrev P and Fallone B G. 3T MR-based treatment planning for radiotherapy of brain lesions. *Radiol Oncol* 2006;40:125-132.

9. Stanescu T, Jans H-S, Stavrev P, Fallone BG. A Complete MR-Based Treatment Planning Procedure for Radiotherapy of Intracranial Lesions. [Abstract]. *Med Phys* 2006;33:2271.

10. Stanescu T, Jans H, Pervez N, Stavrev P, Fallone BG. Developments in MRI Simulation of Intracranial Lesions. [Abstract]. *Radiother Oncol* 2007;84:S18.

11. Lee YK, Bollet M, Charles-Edwards G, Flower M A, Leach M O, McNair H, et al. Radiotherapy treatment planning of prostate cancer using magnetic resonance imaging alone *Radiother. Oncol.* 2003;66:203-216.

12. Chen L, Price R A Jr, Wang L, Li J, Qin L, McNeeley S, et al MRI-based treatment planning for radiotherapy: dosimetric verification for prostate IMRT. *Int. J. Radiat. Oncol. Biol. Phys.* 2004;60:636-647.

13. Chen L, Price Jr. RA., Nguyen T-B, et al. Dosimetric evaluation of MRI-based treatment planning for prostate cancer. *Phys Med Biol* 2004;49:5157-5170.

14. Hill D, et al. Accurate frameless registration of MR and CT images of the head; applications in planning surgery and radiation therapy. *Radiology* 1994;191:447-454.

15. Just M, Rosler HP, Higer HP, Kutzner J, Thelen M. MRI-assisted radiation therapy planning of brain tumors - clinical experience in 17 patients. *Magn Res Imag* 1991;9:173-177.

16. Tanner S, Finnigan DJ, Khoo VS, Mayles P, Dearnaley DP and Leach MO. Radiotherapy planning of the pelvis using distortion corrected MR images: the removal of system distortions. *Phys Med Biol* 2000;45:2117-2132.

17. Karger CP, Hoss A, Bendl R, Canda V and Schad L. Accuracy of device-specific 2D and 3D image distortion correction algorithms for magnetic resonance imaging of the head provided by a manufacturer. *Phys. Med. Biol.* 2006;51:N253-N261.

18. Doran SJ, Charles-Edwards L, Reinsberg S A and Leach M O. A complete distortion correction for MR images: I. Gradient warp correction. *Phys. Med. Biol.* 2005;50:1343-1361.

19. Wang D, Doddrell D M and Cowin G. A novel phantom and method for comprehensive 3-dimensional measurement and correction of geometric distortion in magnetic resonance imaging. *Mag. Res. Imag.* 2004;22:529-542.

20. Stanescu T, Jans H, Fallone BG. Investigation of a 3D MR Distortion Correction Protocol. [Abstract]. *Med Phys* 2006;33:2658

21. Baldwin L, Wachowicz K, Thomas SD, Rivest R, Fallone BG. Characterization, prediction, and correction of geometric distortion in 3 T MR images. *Med Phys* 2007;34:388-399.

22. Breeuwer M, Holden M, Zylka W Detection and correction of geometric distortion in 3D MR images. Proc of SPIE Image Processing. Vol 4322 2001. pp. 1110-1120.

23. Chen Z, Ma CM, Paskalev K, Li J, Yang J, Richardson T, Palacio L, Xu X and Chen L. Investigation of MR image distortion for radiotherapy planning of prostate cancer. *Phys Med Biol* 2006;51:1393-1403.

24. Krempien R, Schubert K, Zierhut D, Steckner MC, Treiber M et al Open low-field magnetic resonance imaging in radiation therapy treatment planning. *Int J Rad Oncol Biol Phys* 2002;53:1350-1360.

25. Mizowaki T, Nagata Y, Okajima K, et al. Reproducibility of geometric distortion in magnetic resonance imaging based on phantom studies. *Radiother & Oncol* 2000;57:237–242.

26. Moerland M, Beersma R, Bhagwandien R, Wijrdeman HK, Bakker CJG. Analysis and correction of geometric distortions in 1.5 T magnetic resonance images for use in radiotherapy treatment planning. *Phys Med Biol* 1995;40:1651-1664.

27. Janke A, Zhao H, Cowin GJ, Galloway J, Dodrell DM. Use of spherical harmonic deconvolution methods to compensate for nonlinear gradient effects on MRI images. *Mag Res Med* 2004;52:115-122.

28. Sumanaweera TS, Glover G H, Binford T O and Adler J R. MR susceptibility misregistration correction. IEEE Trans. Med. Imag. Vol 12; 1993. pp. 251-259.

29. Young I, Cox IJ, Bryant DJ, Bydder GM. The benefits of increasing spatial resolution as a means of reducing artifacts due to field inhomogeneities. *Mag Res Imag* 1988;6:585-590.

30. Chang H, Fitzpatrick JM. A technique for accurate magnetic resonance imaging in the presence of field inhomogeneities. *IEEE T Med Imaging* 1992;11:319-329.

31. Elsen P. Multimodality matching of brain images. PhD thesis, University Hospital Utrecht, The Netherlands; 1993.

32. Reinsberg S, Doran S, Charles-Edwards M, Leach MO. A complete distortion correction for MR images: II. Rectification of static-field inhomogeneities by similarity-based profile mapping. *Phys Med Biol* 2005;50:2651-1661.

33. Bhagwandien R, Moerland MA, Bakker CJ, Beersma R, Lagendijk JJ. Analysis of patient induced marker shifts in MRI. Proceedings Eleventh Annual Meeting of the Society for Magnetic Resonance in Medicine (SMRM); 1992. p. 4305.

34. Bhagwandien R. Object induced geometry and intensity distortions in magnetic resonance imaging: PhD thesis, University of Utrecht, The Netherlands; 1994.

35. Bhagwandien R, Moerland MA, Bakker CJ, Beersma R, Lagendijk JJ. Numerical analysis of the magnetic field for arbitrary magnetic susceptibility distributions in 3D. *Mag Res Imag* 1994;12:101-107.

36. Bhangwandien R, van Ee R, Beersma R and Bakker C J G. Numerical Analysis of the Magnetic Field for Arbitrary Magnetic Susceptibility Distributions in 2D. *Mag. Res. Imag.* 1992;10:299-313.

37. Bakker CJG, Moerland M A, Bhagwandien R and Beersma R. Analysis of machine-dependent and object-induced geometric distortion in 2DFT MR imaging. *Mag. Reson. Imag* 1992;10:597-608.

38. Chang H, and Fitzpatrick J M Geometrical image transformation to compensate for MRI distortions. Proc. SPIE Vol 1233; 1998. pp. 116-127.

39. Wang D, Strugnell W, Cowin G, Doddrell D M, Slaughter R. Geometric distortion in clinical MRI systems Part 1: evaluation using a 3D phantom. *Mag Res Imag* 2004;22:1211-1221.

40. Sled JG, Zijdenbos A P and Evans A C A nonparametric method for automatic correction of intensity nonuniformity in MRI data. *IEEE Trans. Med. Imag.* 1998;17:87-97.

41. Styner M, Brechbuhler C, Szekely G and Gerig G. Parametric Estimate of Intensity Inhomogeneities Applied to MRI. IEEE Trans. Med. Imag. Vol 19; 2000. pp. 153-165.

42. Wang D, Doddrell D M. Method for a detailed measurement of image intensity nonuniformity in magnetic resonance imaging. *Med. Phys.* 2005;32:952-960.

43. Schmidt M. Automatic Brain Tumor Segmentation. Computing Science. Edmonton: University of Alberta; 2005. p. 161.

44. Morris M, Greiner R, Sander J, Murtha A, and Schmidt M. A Classification-based Glioma Diffusion Model Using MRI Data. Proc. Canadian Conference of Artificial Intelligence. Quebec City); 2006.

CHAPTER 3.
PROCEDURE FOR MRI SIMULATION OF INTRACRANIAL LESIONS

3.1 INTRODUCTION

MRI is the imaging modality of choice for the delineation of target volumes used for radiation treatment planning (RTP) due to its superior soft-tissue contrast.[1-5] In MRI, the contrast of adjoining soft tissue organ structures can be widely modified by manipulating the imaging sequence parameters correlated to tissues' characteristic relaxation times (T_1 and T_2) and proton densities. Compared to CT, MRI provides a substantially better description of neighboring soft tissues even when they show very analogous x-ray attenuation properties. Such an example is represented by low grade tumors embedded in the brain, which are characterized by poorly defined boundaries or diffuse infiltration into adjacent healthy structures.[6-8]

Historically, CT is the gold standard imaging modality for RTP. This is mainly due to the reason that, in the past, MRI suffered from considerable technical limitations such as low image resolution, long acquisition times leading to substantial motion artifacts, severe spatial distortions affecting the image geometrical accuracy, and lack of electron density information. Recently, due to technological advances, most of the past impediments were overcome.

In MRI, there is no apparent correlation between tissue signal intensity and CT numbers, which are related directly to attenuation coefficients and electron densities required for dose calculations in RTP. As a consequence, different tissues may exhibit similar signal values, e.g. hard bone and air are depicted as dark regions. Due to this constraint, MR images are traditionally used in conjunction with CT images.[9, 10] Specifically, for example, the RTP process for intracranial lesions consists of (a) contouring of the target on the MR images to benefit from MRI's fine soft-tissue contrast, (b) image fusion of corresponding MR and CT datasets to transfer the volume contours onto the CT images, and (c) dose calculations on CT images based on their innate electron density information. A particular reason for image fusion is that MR images are inherently prone to geometric and intensity distortions from various sources that can

alter the accurate representation of anatomical structures, i.e. spatial location and relative intensity.

Ideally, the simulation of the treatment planning process should rely solely on the information generated by the MR imaging studies, i.e. MRI simulation. In this regard, the simulation process refers to the design of the treatment plan configuration (i.e. radiation fields' number and relative orientation, field optimizers, etc.) and the computation of the dose deposited in the targeted anatomy. In particular, the generation of MRI-DRRs along with the MRI-based RTP verification process are usually discussed separately. Using MRI Simulation, the CT imaging sessions and the image fusion process would become redundant. Also, the patient would not be exposed to unnecessary radiation (as insignificant as it may be when compared to doses received in radiation treatment). Furthermore, any incidental errors associated with the image fusion process caused by patient inter-procedure positioning and inaccuracies in identifying the correct topography of the structures investigated between CT and MRI datasets would be avoided. As a direct consequence, the improved target localization is expected to lead to a higher local tumor control and reduced normal tissue complications.

In recent years there has been an increasing interest in developing new techniques for MRI simulation aimed to improve the RTP process of brain[11-14] and prostate[15-19] cancer. In general, to perform MRI Simulation, it is required that different electron density information be correlated or assigned to MR images and the image distortions be addressed. To compensate for the lack of intrinsic electron density data MR images can be prepared for dose calculations by assigning bulk CT values to the voxels corresponding to segmented volumes of interest (VOIs).[12, 15, 18] These VOIs represent certain tissue types relevant to dosimetric calculations such as bone, lung, and soft tissue.

MR image distortions are caused by scanner-related and patient-induced effects. The scanner-related distortions are due to main magnetic field ($\vec{B}_0$) inhomogeneities and gradient

non-linearities.[20-22] In contrast, the patient-induced artifacts are sourced in susceptibility and chemical shift local variations in the imaged volume.[23, 24] The magnitude of distortions depends on the scanning parameters of the imaging sequence. As RTP requires a spatial fidelity in images of less than 2 mm,[25, 26] the distortions need to be quantified and rectified before the images are used in the clinical process. In recent years, extensive methods were developed to investigate and correct for distortions.[27-34]

The data on MRI Simulation for intracranial lesions are rather scarce. In the late nineties, Beavis *et al*[35] reported on a method based on assigning a unique electron density value, i.e. water, to the entire head volume, thus neglecting the effects of inhomogeneities. In their study, the authors also assumed that the 3D image distortions were negligible. The latter assumption was based on image distortion measurements performed on a phantom object. However, this phantom, by its design, suffered of certain limitations which prevented the accurate description of the 3D distortion field. Specifically, the reference points that sampled the volume of interest were insufficient, i.e. limited to 17 points per image slice for a typical head field of view (FOV) of 20 cm diameter. These points are used to measure the distortions in the volume of interest. Recently, more advanced distortions correction techniques showed that a significantly larger number of control points are required to precisely measure the local variations of the distortion field.[28, 29] Furthermore, the slice warp distortion, i.e. distortion along *z*-axis, was not addressed as the authors investigated the in-plane distortions only. Recent studies[30, 32, 33] showed that the scanner-related distortion levels, corresponding to a brain scan, can be up to 6 mm depending on the scanner type and imaging sequence. These findings stress the importance of implementing techniques for correcting the MR images before using them in the RTP's contouring and dose calculation processes.

MRI Simulation was also investigated for prostate patients by different authors.[15-19] The studies showed that MRI datasets that are corrected for distortion and assigned bulk densities to organ structures could successfully replace the CT images for treatment planning.

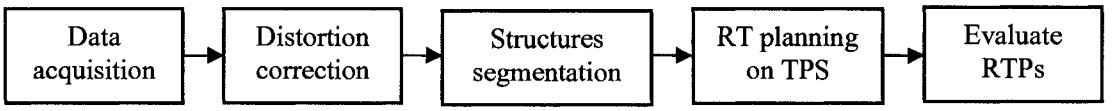

Figure 3.1. MR only based treatment planning procedure for RT of intracranial lesions

In this chapter, we describe an MRI Simulation procedure for intracranial lesions[11-14] (see diagram in Fig. 3.1) that relies on (a) image distortion correction based on an adaptive thresholding and iterative method (see Chapter 2), (b) autosegmentation of organ structures relevant to dosimetric calculations (i.e. scalp, bone, and brain) using an atlas-based non-rigid registration technique, (c) conversion of MR images into CT-like images by assigning bulk electron density values to organ contours, and dose calculations performed with a commercial treatment planning system (TPS), and (d) plan ranking based on a tumor control probability (TCP) method for heterogeneous irradiation that is independent of radiobiological parameters.[12, 36] The dosimetry accuracy of the proposed procedure is investigated by comparing MRI-only and CT+MRI-based plans.

3.2 METHODS AND MATERIALS

The flowchart of the procedure is presented in Fig. 3.1.

3.2.1 Data acquisition - CT and MRI scanning procedures

We used data from 4 glioblastoma multiforme (GBM) patients. Each individual was subjected to two subsequent scanning sessions, namely CT and 3 T MRI, following a clinical protocol approved and implemented at our institution, i.e. Cross Cancer Institute (CCI). Firstly, data was acquired on a Picker PQ 5000 CT simulator (Philips Medical Systems, Cleveland, OH) by means of a 480 mm FOV, matrix 512 x 512 (pixel resolution 0.94 x 0.94 mm^2), 83 slices with 2 mm thickness each, and slice gap of 2.5 mm. Each patient was positioned on the system couch using a head immobilization system consisting of a jig on which custom plastic shells were attached. Donut-shaped fiducial markers filled with a copper sulphate solution (IZI Medical Products, Inc.) were attached to the shells to mark the triangulation laser reference points.

A time interval of about half an hour is required to relocate the patients and to prepare them for the MRI scanning session performed on a 3 T Intera (Philips Medical Systems, Cleveland, OH) unit. To mimic the setup used in the CT room (same system of reference), the subjects were repositioned by using the scanner's lasers, an in-house built flat bed and the same head insert, plastic shells and fiducial markers. The positioning devices were used inside a head coil as its aperture was sufficiently large to house them. The imaging protocol includes (a) a standard scout sequence to select the region containing the target, (b) a 3D T1 turbo field echo (TFE) sequence with contrast enhancement administered intravenously, i.e. 0.1 mmol/kg body weight Gd-DTPA, and (c) a 3D T2 turbo spin echo (TSE) sequence. The T1-weighted image sequence was used for contouring the target and the organs at risk in the CT+MRI-based RTP process and for MRI Simulation. In contrast, the T2-weighted datasets were required for

visualization purposes only to better identify the tumor's spread. The 3D T1 TFE sequence is characterized by a TE/TR/α of 4.1 ms/8.8 ms/8°, 240 x 240 mm^2 FOV, 256 x 256 in-plane matrix (pixel resolution 0.94 x 0.94 mm^2), and 125 contiguous partitions of 1 mm each. It is assumed that the inter-modality patient positioning can be achieved with an accuracy of 1-2 mm. After the scanning process, the image datasets were recorded and subsequently transferred via a local network to Eclipse TPS (Varian Medical Systems) for virtual treatment planning simulation.

3.2.2 MR image distortion correction

In Chapter 2, we described a method for the determination and correction of image system-related distortions. In particular, we measured and corrected for the image distortions characterizing the 3D T1-weighted sequence (see Section 3.2.1), which was used to scan all GBM patients. Once the 3D system distortions are determined (see Chapter 2), they can be used to correct any subsequent clinical dataset as this type of distortion is not patient-dependant. The patient datasets were rectified by using an automatic in-house image processing tool developed in Matlab (The MathWorks, Inc., Natick, MA). Its algorithm includes the following steps:

a) Import and register image datasets to the 3D distortion field coordinates by using the DICOM information embedded in the images' headers. Specifically, the in-plane location of the scanner's isocenter is not necessarily located at the image's center. That means each patient dataset may present a different shift that has to be determined. In particular, for our 3 T Intera scanner the in-plane displacement from isocenter can be calculated by using Eq. 2.9 (see Chapter 2). The 2D image-based datasets are re-formatted into a single 3D image object;

b) Correct image data by means of spatial and pixel intensity interpolation methods.

c) Export corrected image data in DICOM format. Before the distortion correction process, the DICOM header is removed from each individual image file and recorded separately. Once the 3D image data is rectified, it is re-formatted back into 2D images. The unmodified DICOM headers are attached to their corresponding corrected images. The result is a new dataset that has the same DICOM identification parameters but different image information. The advantage of keeping an unmodified DICOM header is that the registration process between uncorrected and corrected MR datasets is done automatically, i.e. DICOM coordinates match registration in Eclipse. This simplifies the evaluation process of our MRI Simulation as it is described in detail below.

In this work, we assumed that the patient-induced distortions present in the brain datasets were negligible. Previous studies[27, 31, 35, 37, 38] showed that this type of distortions were noticeable, i.e. 2-4 mm, only in the sinuses' region at the air-tissue boundaries. In contrast, in the radiation treatment planning-relevant volumes, e.g. brain, the distortions were found to be insignificant, i.e. within the image pixel size. As a check of our assumption, we visually compared the contours of several head sub-substructures (e.g. scalp, brain, bone) segmented on the MR corrected images (system-related distortions) with their corresponding representation on the CT datasets.

3.2.3 Head sub-structures segmentation

The head image slices were segmented into scalp, bone and brain by using a freely available library of image processing tools, i.e. FSL (Analysis Group, FMRIB, Oxford, UK)[39]. Specifically, these structures were automatically extracted by using an atlas-based non-rigid registration technique which consists of a) correction for image intensity variations, b) non-linear registration to an anatomical template, and c) structures classification. In particular, the template represents a probabilistic 3D map of skull/brain sub-structures obtained by fusing a large number of patient

datasets. The output consists of binary image datasets corresponding to each structure of interest, i.e. the organs are depicted as white regions on black background. The contours of these structures can be easily obtained (e.g. in Matlab) and converted into RT structure files that are subsequently imported into Eclipse. Alternatively, the binary images converted into RT structure files can be directly imported into Eclipse and automatically outlined by setting a unique threshold value for the entire dataset (e.g. "Search Body" contouring tool). The autosegmented outlines were visually inspected by overlaying them on the original images in Eclipse. The accuracy of the segmentation process was characterized by the degree of agreement between the organ contours and their corresponding image representation. It was considered a successful segmentation when we obtained a good match between the contours and their corresponding image volumes after applying none or little manual refinement of the outlines. As an alternative to FSL, there are also other freely available tools such as MNI_ANIMAL (McConnell Brain Imaging Centre, McGill University, Canada)[40, 41] and SPM5 (University College London, UK)[42]. We chose to use FSL as it was easier to implement in our MRI Simulation procedure due to its output files portability.

3.2.4 Radiation treatment planning

We generated and compared CT+MR and MR-only based treatment plans using clinical data. The treatment planning process was performed on Eclipse.

CT+MRI-based RTP

In our institution, the standard RTP procedure for GBM subjects relies on image fusion of CT and MRI (uncorrected for distortion) datasets along with CT-based dose calculations. To register MRI to CT datasets, we initially used prominent bony landmarks located around the brain. At

least five pairs of identical and non-coplanar bony landmarks were marked on both CT and MRI datasets. As a preliminary step, to assess the accuracy of the registration process we used Eclipse's 'Mean Error Indicator'. This metric is defined by the mean error between the displacements of registration pairs of point identified in the CT and MR images. For all registrations we achieved a mean error of roughly 1-1.5 mm. However, the mean error metric is suggested to be used as a guideline only (see Eclipse manual). Additional three dimensional manual refining was performed to adjust the image registration according to brain tissue and the bone-brain interface. We avoided relying on fiducial markers or any bony landmarks located near the nasal sinuses as they are prone to artifacts due to susceptibility variations at the marker/tissue-air interface. The results were visually verified by a radiation oncologist by overlaying the CT and MR images.

The clinical target volume (CTV) and the organs at risk (i.e. eyes, eye lens, optic nerves, optic chiasm, pituitary gland, brain stem) were contoured by a radiation oncologist on the uncorrected T_1-weighted datasets by using typical contouring tools available in Eclipse. A 5 mm margin was uniformly added in all directions to the CTV to generate the planning target volume (PTV). The volume contours were copied onto the CT images (registered to MR images), which were subsequently used for virtual simulation of the treatment setup and dose calculations.

For each patient, we generated IMRT plans based on an arrangement of five beams to meet our clinical acceptance criteria, specifically 95% of the PTV has to receive the prescribed dose (D_{ref}). In addition, the maximum dose to the target (D_{max}) should not exceed 105% of D_{ref} and the minimum dose to the target (D_{min}) should not be lower than 95% of D_{ref} unless the hot and cold spot areas, respectively, are smaller than 1 cm^2. The organs at risk dose limits were: 50 Gy for eyes, 10 Gy for eye lens, 50-55 Gy for the pituitary gland, 45-50 Gy for the optic nerve/chiasm, and 55 Gy for the brain stem. The plans were verified and approved by a radiation oncologist.

MRI-based RTP (MRI Simulation)

For this procedure, firstly, the patient MR images were corrected for distortion (see Chapter 2). The following step was to generate image binary masks for scalp, bone, and brain using the FSL autosegmentation tool. The contours of these structures were recorded in Eclipse as separate organs. For this study, instead of re-drawing the CTV/PTV and structures at risk volume outlines on the corrected MR images it was easier to correct them for distortion following a similar procedure as for the MR image datasets. Specifically, the process consists of the following steps:

a) Export from Eclipse the RT structure file containing the uncorrected outlines. The RT file is written in a DICOM compatible format. It has the structure of a "cell", specifically it consists of series of multidimensional arrays following a certain architecture. The arrays enclose a miscellaneous collection of data such as contour labels, contour point coordinates, etc;

b) Access the RT structure file, i.e. read in, extract and write the coordinates of the contour points corresponding to each individual organ structure. This step was performed by using an in-house developed software tool written in Matlab. Given the complex structure of the RT file (custom to Eclipse), the path to the contour point arrays needs to be identified. Once we can access each set of contour points, we register the points into the system of reference corresponding to the 3D distortion field, i.e. the same 3D matrix utilized to rectify the raw MR images (see Section 3.2.2). The corrected location of each contour point is determined through interpolation techniques. Due to the out-of-plane distortion some control points are characterized by non-integer z-coordinate values. These quantities are rounded to the closest integer. Only the control points with z-coordinate values matching the location of the image slices are recorded and written back in the RT structure file;

c) Import in Eclipse the new RT structure file and record the corrected organ volumes.

Besides being more practical to obtain the organs at risk outlines, another important reason for using this method was to avoid intra-modality volume changes by re-drawing the structures on the corrected images. This is important for an accurate evaluation of the of the MRI Simulation procedure. In practice, for MRI-based RTPs the organs at risk volumes will be segmented directly on the corrected datasets.

Once the images and all contours of interest are available, we need to assign bulk CT values to the voxels enclosed by the scalp, bone, and brain volumes, to convert the MR images into CT-like images. For scalp and brain we assigned 0 HU (i.e. Hounsfield units) and for bone 1000 HU. These values are equivalent to electron densities of 1 g/cm^3 and 1.8 g/cm^3, respectively. For brain we performed a uniformity check regarding the distribution of electron density values. This was done by placing five regions of interest (ROIs) on each image slice containing brain information (see Fig. 3.2a). The pixel values were averaged in each ROI and converted into relative densities by using the calibration curve shown in Fig. 3.2b.

Each MRI-based plan was generated by applying its corresponding CT+MRI plan, i.e. by copying the beam arrangements and fluences. The plan transfer is done with regard to the isocenter, which was set to be at the centre of mass of the PTV volume. Before performing dose calculations in Eclipse, each MRI dataset has to be associated to an imaging device, i.e. to assign a conversion table between assigned HU values and relative electron densities (Fig. 3.2b).

Another aspect of the MRI Simulation process is related to the DICOM import of the MRI datasets in Eclipse. For RT planning purposes, the TPS was designed to successfully import and use for simulation MRI axial datasets only. Translated into DICOM information, the tag corresponding to the spatial orientation of the image slice plane of an axial dataset would be characterized by certain integer numbers, i.e. 1/0/0. Occasionally, we encountered datasets which were 'almost axial', specifically the image orientation tag would contain numbers that are slightly different than 1/0/0, e.g. 0.99999991/0/0. It was not clear if this was due to a) scanner

operation –image sequence setup or b) a bug in the MR scanner's software. However, this issue can be easily resolved by editing the DICOM header of the image dataset.

3.2.5 Comparison and evaluation of RTPs

To validate our MRI Simulation procedure we generated and compared several RTPs as follows:

a) All MRI contours including PTV, organs at risk, and dosimetrically relevant structures (i.e. scalp, bone, and brain), were transferred onto the CT images after the MR and CT images were fused. Bulk CT values were assigned to scalp, bone, and brain, thus overriding the intrinsic CT values of the images. For convenience we will name this type of plan CT+MRI (MRI contours dosimetry). This plan was compared to the standard CT+MRI-based plan in order to evaluate the accuracy of CT values assignation method;

b) To investigate the effects of MR image distortions we compared MRI (uncorrected) to MRI (corrected)-based plans. "Uncorrected" and "corrected" refer to the use of the uncorrected and corrected image datasets, respectively. For the same purpose, we also compared CT+MRI-based plans built using the uncorrected and corrected PTV volumes;

c) To determine the overall effect of image fusion, MR image distortions, segmentation of head sub-structures, and CT values bulk assignation we compared CT+MRI (uncorrected) to MRI (corrected)-based plans.

To compare the plans we used certain indicators such as isodose distributions, dose volume histograms (DVHs), source-to-surface distances (SSD) and monitor units (MUs) for each field, dose at the isocenter (D_{iso}), mean target dose (D_{mean}), D_{min}, and D_{max}.

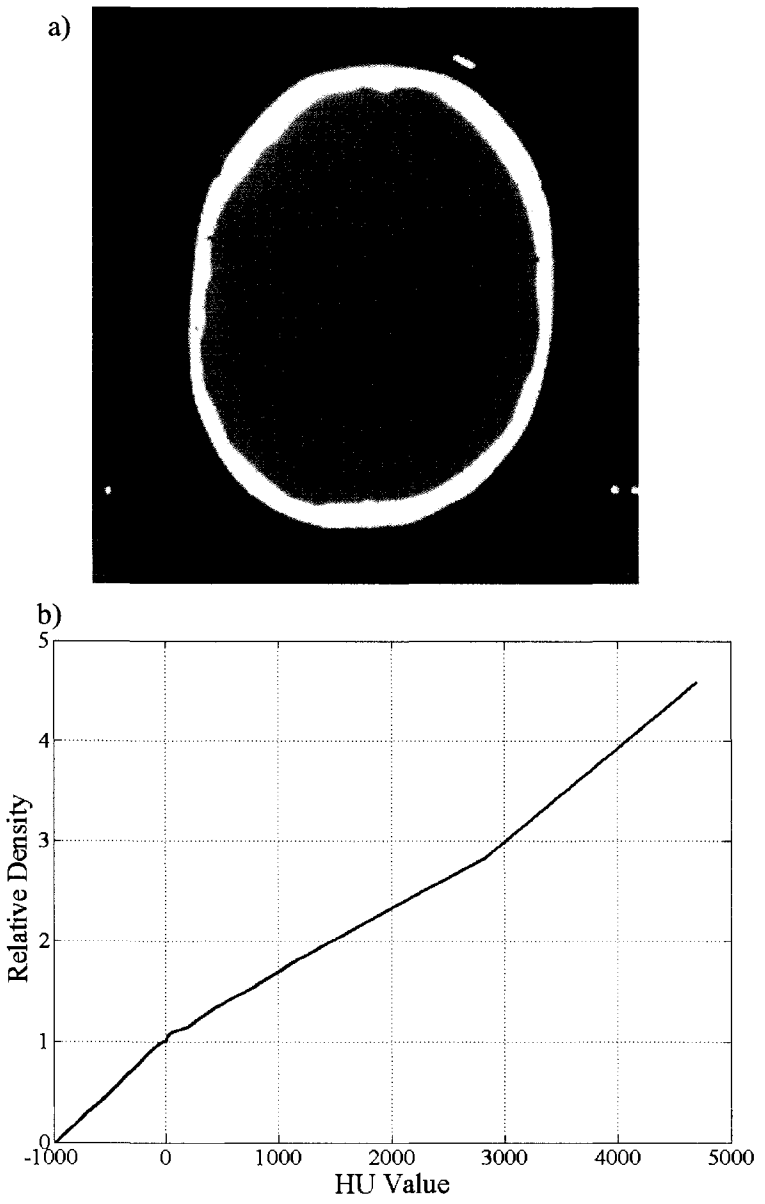

Figure 3.2. (a) Regions of interest used to assess the uniformity of the electron density values in brain; (b) calibration curve representing the correlation between relative density (with respect to water) and HU.

RTP ranking tool

To quantify the RT plan comparison process we used a TCP-based technique for heterogeneous irradiation developed by Stavrev *et al.*[1, 36] This is desired as the DVHs alone may not be sufficient to appropriately describe the clinical outcome. This technique does not require knowledge of exact radiobiological parameter values. Corresponding TCP values for the investigated MRI Simulation and MRI+CT-based plans were calculated and compared for parameter values of the entire parametric space. Here we give only a brief description of the method.

The Poisson-based TCP model $TCP = e^{-N_s}$ is used, where N_s is the number of surviving clonogens, estimated by the single hit cell dose response model as $N_s = N_o e^{-\alpha D}$ where N_o is the initial number of clonogens, α is the radiosensitivity, and D is the delivered dose. As pointed out by Brahme,[43] the mathematical form of the single hit model becomes identical to the linear quadratic (LQ) model in the case of the standard fractionation schemes (n fractions each delivering a dose d): $N_s = N_o e^{-(\alpha+\beta nd)D} = N_o e^{-\hat{\alpha}D}$, where $\hat{\alpha}$ is the generalized radiosensitivity. Recently, it was shown that the adjusted radiosensitivity takes into account the repopulation as well.[44] For plan ranking purposes, it is better to use the TCP model in terms of the survival fraction at a dose equal to 2 Gy (i.e. $SF_2 = e^{-2\hat{\alpha}}$), because this parameter is confined in the interval [0,1]:

$$TCP = \exp(-N_o e^{-\hat{\alpha}D}) = \exp(-N_o \cdot SF_2^{0.5D}) \tag{3.1}$$

In the case of heterogeneous irradiation we obtain

$$TCP = \exp(-\rho \sum V_i e^{-\hat{\alpha}D_i}) = \exp(-\rho \sum V_i \cdot SF_2^{0.5D_i}) \tag{3.2}$$

where ρ is the cell density, $\{V_i, D_i\}$ represents the differential DVH using the absolute (not the relative) tumor sub-volumes V_i irradiated to doses D_i. For simplicity, we assumed that the tumor cell density is presumed to be 10^9 cells/mm^3. In fact, this number is not very important because the plans ranked are for the same tumor site, hence having the same tumor cell density.

Essentially, a plan resulting in higher TCP values, for any value of the parameter SF_2, should be considered superior to the plan resulting in lower TCP values. Thus, if we plot the TCP curves as functions of the parameter SF_2, i.e. $TCP(SF_2 \mid DVH_1)$ and $TCP(SF_2 \mid DVH_2)$, the curve placed to the right would correspond to the better RT plan, producing higher TCPs for any value of SF_2.

The following measures can be introduced for the estimation of the closeness in TCP terms of two RT plans:

$$C = \int_0^1 \left(TCP(SF_2 \mid DVH_2) - TCP(SF_2 \mid DVH_1)\right) dSF_2 \tag{3.3}$$

$$\Delta^{\max} TCP = \max_{SF_2} \left(TCP(SF_2 \mid DVH_2) - TCP(SF_2 \mid DVH_1)\right) \tag{3.4}$$

where C is defined in the [0,1] interval and represents the area between the TCP curves corresponding to the two plans under investigation, and $\Delta^{\max} TCP$ is the maximal expected TCP difference between the two plans. The sign of these two measures indicates the better plan.

3.3 RESULTS AND DISCUSSION

3.3.1 MR image distortion impact on RTP

The MRI-based procedure suggested by Beavis *et al*[35] considered the system-related distortions in the brain as being negligible. However, the authors used a simple distortion correction technique along with a phantom object that prevented them from accurately determining the 3D distortion field. Considering the particular characteristics of our GBM MR imaging protocol, namely a 3D TFE sequence acquired on a 3 T Intera scanner, MR image distortion correction is required as suggested by Fig. 2.14. Namely, for a sphere with a diameter of 20 cm, the total maximum distortion (see Eqs. (2.8) and (2.9)) was found to be about 4 mm. In a previous study,[30] Wang *et al* investigated in detail the distortion fields of several commercially available MRI scanners and found that the magnitude of distortions can be as high as 6 mm for a typical brain study FOV. These findings stress the importance of determining the 3D distortion field, which is unique to each MR scanner, as a necessary step in the MRI Simulation process. Also, patient images need to be corrected before being used for RTP purposes. This is crucial as local distortions affect both the volume size and the spatial location of the organs. Any error in identifying the target/organs will translate into a reduced accuracy in delivering the treatment and consequently in likely reduction of the probability of tumor control.

To assess the effect of image distortion on the accuracy of the RTP process we firstly compared the effects of distortions on the PTV. Table 3.1 shows the PTV volumes corresponding to the corrected and uncorrected MR image datasets. For three out of four patients, by rectifying the images the PTVs became smaller. The maximum percent difference was 1.1% corresponding to patient 3. Table 3.2 summarizes the maximum absolute distortion corresponding to the PTV, body, bone, and brain volume outlines. For all structures of interest the distortion is less than 2 mm.

Patient number	uncorrected (cm^3)	corrected (cm^3)	Absolute difference (%)
1	102.69	103.58	0.9
2	96.58	96.12	0.5
3	85.47	84.56	1.1
4	47.34	47.21	0.3

Table 3.1. PTV volumes determined on the MRI uncorrected and corrected datasets along with their percent difference.

Patient number	PTV (mm)	body (mm)	bone (mm)	brain (mm)
1	1.56	1.84	1.69	1.68
2	1.58	1.73	1.63	1.63
3	1.25	1.67	1.63	1.59
4	1.50	1.66	1.65	1.65

Table 3.2. Maximum distortion values corresponding to several structures of interest.

Patient number	D_{mean} (%)	D_{min} (%)	$\lvert D_{max} \rvert$ (%)
1	0.0	1.7	0.2
2	0.0	1.5	0.0
3	0.0	0.0	0.0
4	0.0	0.1	0.0

Table 3.3. Percent difference of dosimetric parameters calculated for the PTV uncorrected and PTV corrected volumes on the CT+MRI-based plan.

In Table 3.3 the percent difference of dosimetric parameters calculated for the PTV uncorrected and PTV corrected structures are presented for the CT+MRI-based plan. There is practically no difference in D_{mean} and D_{max} values and a maximum change of < 2% in D_{min} values.

Table 3.4 compares the MRI (uncorrected) and MRI (corrected)-based plans in terms of percent difference of several dosimetric parameters such as D_{mean}, D_{min}, and D_{max}. The differences in terms of D_{mean} and D_{max} values between the two plans are negligible. The minimum target dose, i.e. D_{min}, between the two plans agrees within 1%. For the above plans, the isodose distributions are very similar and the changes in the DVHs, corresponding to the organs-at-risk and target, are clinically insignificant.

Analyzing the available data, we found that image distortion had a negligible impact on the RT plans' outcome. This is apparently in disagreement with our earlier results, i.e. image distortion is important for brain studies (see Fig. 2.15). However, this can be explained by considering that the clinical protocol at CCI considers the acquisition of 125 contiguous MR image slices only, with a thickness of 1 mm each (see Section 3.2.1). The data is acquired in such a way that only the target area and its close vicinity are imaged, and not the entire head as in a standard CT scan (or MRI Simulation). Furthermore, the datasets are centered at the isocenter of the MRI scanner where the magnitude of distortion is significantly lower. As a consequence, all MRI datasets will have an extension along z-axis of about ± 6.25 cm only. In such a volume, the distortion level is roughly 2 mm, in agreement with data presented in Table 3.2.

We also investigated the magnitude of patient-induced distortions by comparing the contours of several head sub-structures delineated on both CT and MR corrected images. The discrepancy between the two sets of contours was defined as a combination of several factors, specifically (a) susceptibility and chemical shift artifacts (b) residual distortion after applying the system-related image correction method (see Chapter 2), and (c) errors associated with the image fusion process. We found that the maximum shift between corresponding structures was within 2 mm, hence being acceptable for RT planning purposes.

Patient number	D_{mean} (%)	D_{min} (%)	$\|D_{max}\|$ (%)
1	0.1	0.4	0.4
2	0.1	1.0	0.2
3	0.0	0.3	0.2
4	0.0	0.1	0.0

Table 3.4. Percent difference of dosimetric parameters calculated for the PTV corresponding to the MRI (uncorrected) and MRI (corrected)-based plans.

Patient number	D_{iso} (%)	D_{mean} (%)	D_{min} (%)	$\|D_{max}\|$ (%)
1	0.9	0.1	0.6	0.2
2	0.9	0.2	0.0	0.6
3	0.9	0.3	0.4	0.5
4	1.0	0.3	0.8	0.4

Table 3.5. Percent difference of dosimetric parameters calculated for the PTV for the CT+MRI and CT+MRI (MR-contours dosimetry)-based plans.

Patient number	D_{iso} (%)	D_{mean} (%)	D_{min} (%)	$\|D_{max}\|$ (%)
1	1.0	0.2	5.5	0.5
2	1.8	0.3	12.5	0.4
3	1.2	0.3	4.7	0.5
4	1.2	0.3	6.3	0.5

Table 3.6. Percent difference of dosimetric parameters calculated for the PTV for the CT+MRI (uncorrected) and MRI (corrected)-based plans.

3.3.2 Bulk CT values effects on RTP

Brain studies[12, 45-47] showed that the difference between turning on and off the inhomogeneity correction resulted in a dose difference of about 2-3%. For the MRI-based plans, the inhomogeneities taken into account as the scalp, skull, and brain outlines were automatically obtained with the FSL software library tools. The head sub-structures contours visually agreed well with their corresponding image volume (within 1-2 mm). Using FSL, the structures' segmentation becomes significantly faster than with the manual/semi-automatic techniques.[12] Considering that a) the MR image distortions were negligible and b) for the image fusion process we used anatomical landmarks that were not affected by subject-induced image artifacts (see Section 3.2.4), the registration errors of the CT and MRI datasets were minimal, i.e. < 1-2 mm.

By performing the electron density uniformity check in the brain volume, we found that there was no significant variation from the density of water (within 2%). Therefore, we assigned to the brain a bulk value of 0 HU, which is equivalent to the electron density value of 1 g/cm^3. Table 3.5 shows the comparison between the CT+MRI plans and the CT+MRI (MRI contours dosimetry)-based plans in terms of percent difference calculated for D_{iso}, D_{mean}, D_{min}, and D_{max}. The difference in maximum and minimum dose delivered to the target is < 1%. Similarly, for all subjects the D_{iso} variation is roughly 1%. D_{mean} values change slightly from one plan to another. There is no clinically relevant difference in the DVHs. Also, by using the RT ranking tool we did not find any significant change between the plans. The dosimetric parameters shown in Table 3.5 suggest that the conversion process of MR images into CT-like images was accurate enough for RTP purposes.

3.3.3 CT+MRI (uncorrected) v. MRI (corrected)-based plans

To determine the overall effect of image fusion, MR image distortions, segmentation of head sub-structures, and CT values bulk assignation we compared CT+MRI (uncorrected) to MRI (corrected)-based plans. Figure 3.3 compares the isodose distributions, corresponding to the isocenter slice, between a typical CT+MRI (uncorrected) and MRI (corrected)-based plans (patient number 1). The PTV is depicted as the red-coloured area and the isocenter is given by the yellow dot. In particular, in Fig. 3.3b the brain, bone, and scalp contours are also displayed. The scalp outline mask coincides with the patient outline. The dose distributions of the two plans are very similar, showing a complete coverage of the PTV by the 95% isodose line. Table 3.6 summarizes the dosimetric parameters used to compare the two plans. Specifically, the percent difference in the D_{mean} and D_{max} values is < 1%. The maximum variations in terms of D_{iso} and D_{min} are 1.8% and 12.5%, respectively. The DVHs corresponding to the PTVs are shown in Fig. 3.4. Comparing the two plans by means of the RT ranking tool, we found that the difference in TCPs between them was within 1%. The maximal TCP difference between both plans, in all cases, does not ascent 4%. Figure 3.4 displays the TCP plan ranking of the investigated cases. Regarding the organs at risk, there was no clinical difference between the two plans.

Due to mainly negligible MR image distortion artifacts and the use of a reliable image fusion technique the differences between these plans were found to be clinically insignificant. However, significant errors can be introduced by means of a) image registration that relies on fiducial markers and bony landmarks located near air-tissue interfaces, and b) RTP based on full head uncorrected MRI datasets that are prone to significant distortion effects. As a result, the RT plan comparison might show clinically relevant discrepancies suggesting that the MRI (corrected)-based plans are more accurate than the standard procedure CT+MRI (uncorrected). MRI Simulation simplifies the RTP process by not requiring additional CT data and the image fusion process.

Depending on the RT modality used in conjunction with the MRI Simulation procedure, the RT verification process, i.e. correct (re-)positioning of the patient before and during the treatment, can be performed based on the registration process between

a) Digitally reconstructed radiographs from MR images (MR-DRRs) and CT/MVCT images by segmenting the MR datasets into dosimetric relevant VOIs (e.g. bone, soft-tissue) and assigning to them bulk electron density information.[48-50] In our case, the skull can be automatically segmented using FSL (see Section 3.2.3) and electron density information can be assigned in Eclipse in order to generate MR-DRRs;

b) MR images and real-time MR data (in particular for an MRI-Linac system[51, 52]).

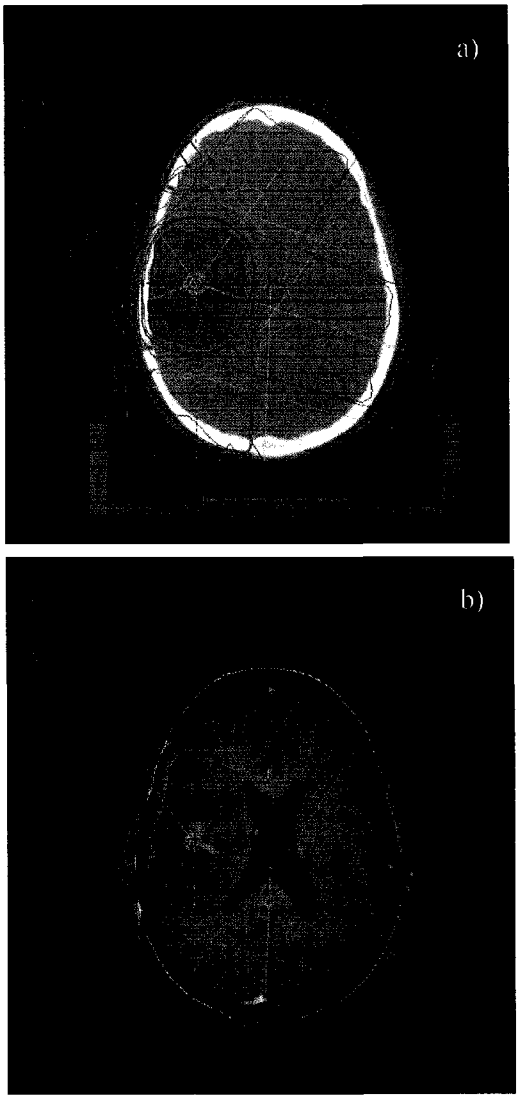

Figure 3.3. Typical example showing a comparison of isodose distributions between a) CT+MRI (uncorrected)-based plan and b) MRI (corrected)-only plan.

a)

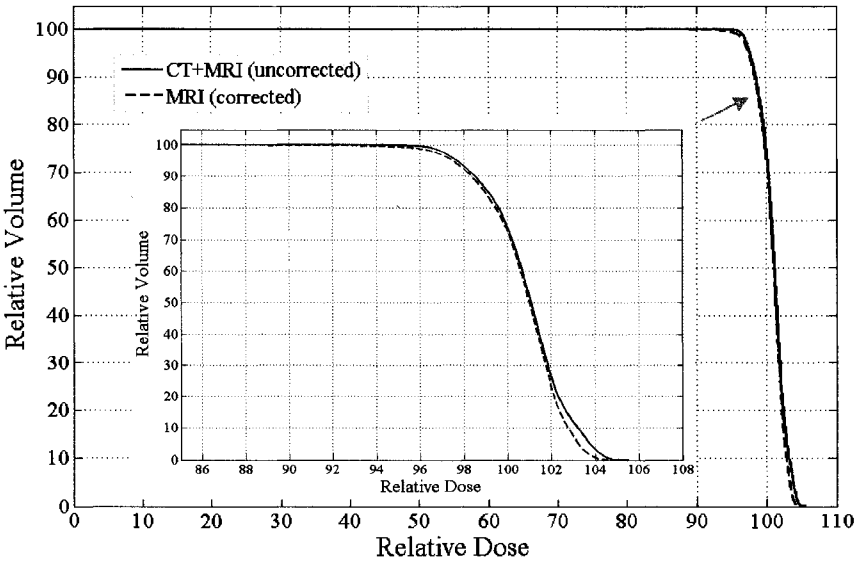
CT+MRI (uncorrected)
MRI (corrected)
Relative Volume
Relative Dose

b)

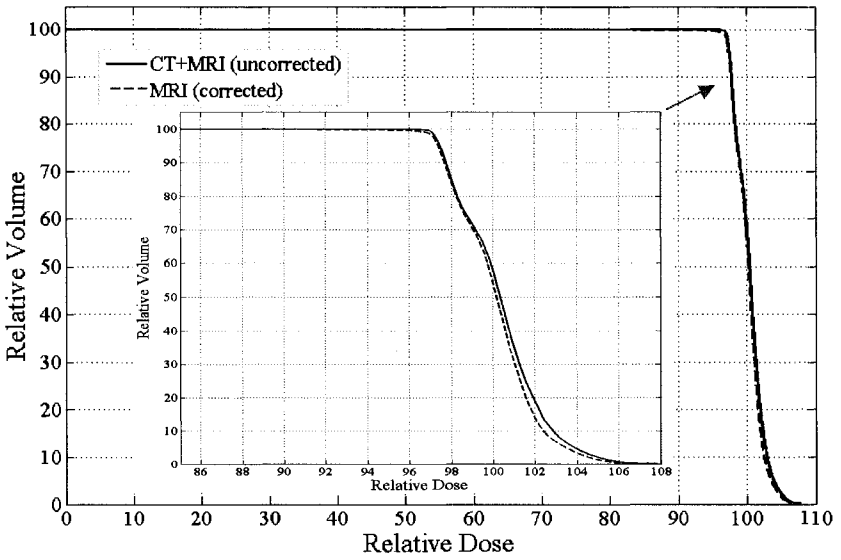
CT+MRI (uncorrected)
MRI (corrected)
Relative Volume
Relative Dose

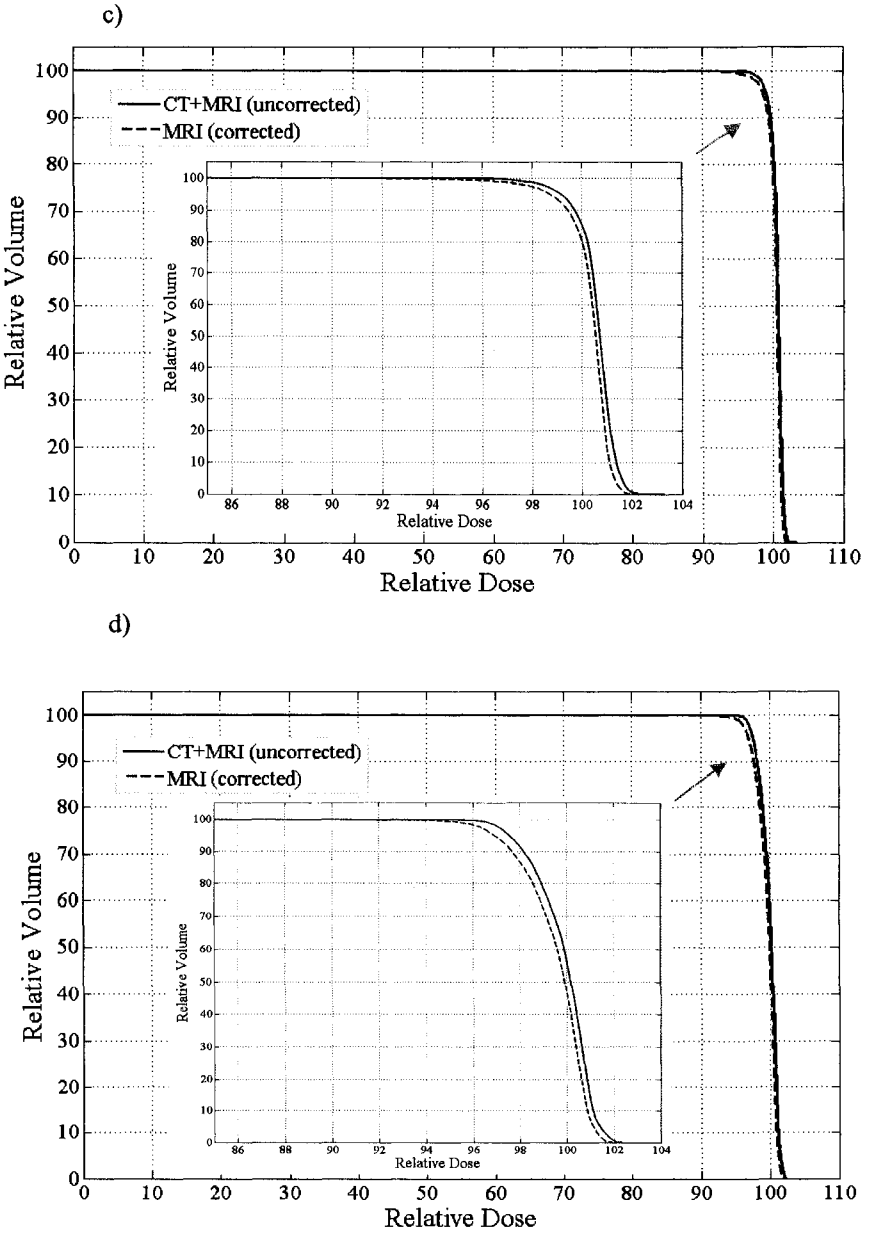

Figure 3.4. Comparison of the PTV DVHs corresponding to the CT+MRI (uncorrected) and MRI (corrected) – based plans for the four patients. The small caption corresponding to each graph represent a zoomed in plot of the DVHs.

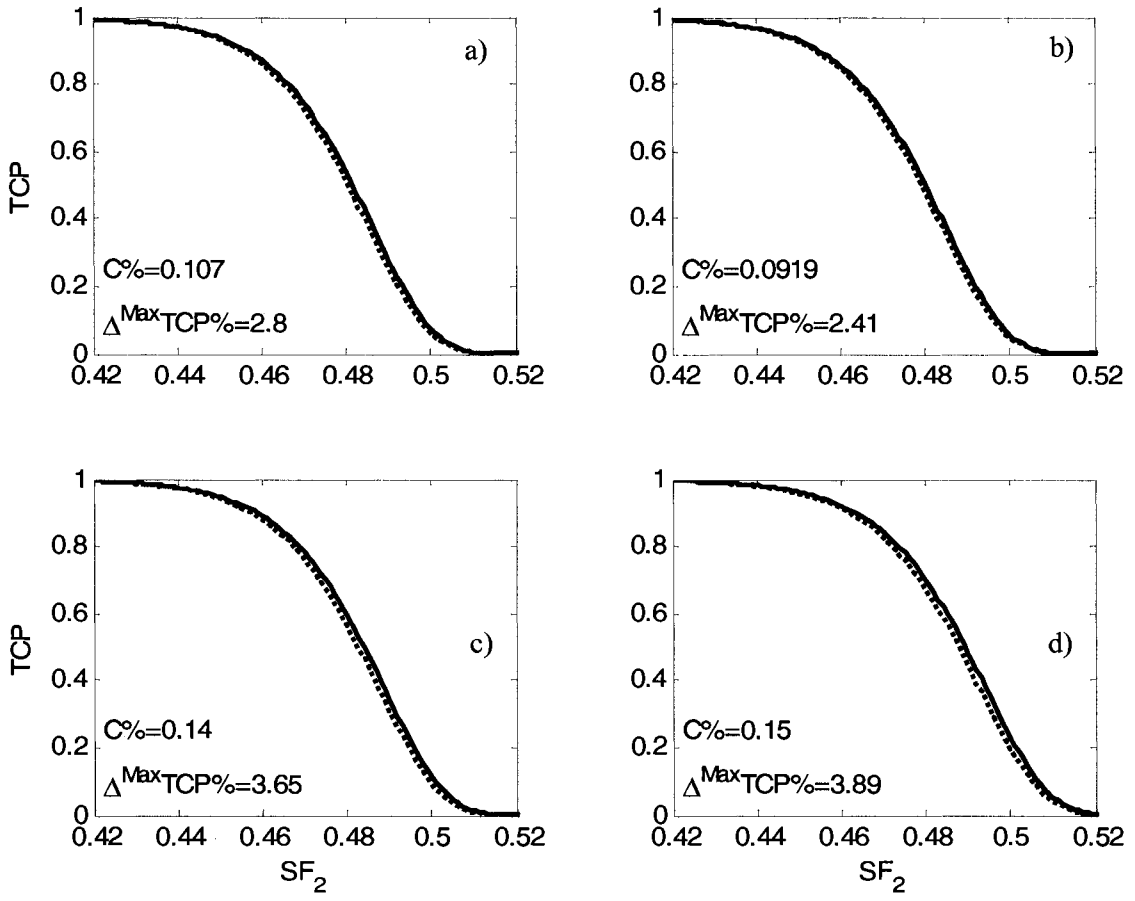

Figure 3.5. TCP-based comparison between the CT+MRI (uncorrected) and MRI (corrected)-only plans corresponding to the four patients. CT+MRI plan is given by the solid line and the MRI plan is represented by the dashed line, respectively.

3.4 CONCLUSIONS

In this study, we investigated a procedure for the MRI Simulation of intracranial lesions based on the following steps (a) correction of the MR image datasets for 3D distortions, (b) automatic segmentation of head sub-structures (i.e. scalp, bone, and brain) relevant for dosimetric calculations, (c) preparation of the MRI datasets for dose calculations by assigning bulk CT values to head sub-structures and performing MRI-based dose calculations in Eclipse, and (d) plan evaluation process based on isodose distributions, various dosimetric parameters, DVHs, and an RT plan ranking tool.

The results of this study show that the proposed MRI Simulation procedure performed similarly to the standard clinical technique based on CT and MRI and is suitable for the radiotherapy of brain cancer.

3.5 REFERENCES

1. Johnson P, Hunt SJ, Drayer BP. Human cerebral gliomas: correlation of postmortem MR imaging and neuropathologic findings. *Radiology* 1989;170:211-217.
2. Zawadzki M. MR imaging of the brain. *Radiology* 1988;166:1-10.
3. Sailer S, Rosenman JG, Soltys M, et al. Improving treatment planning accuracy through multimodality imaging. *Int J Radiat Oncol Biol Phys* 1996;35:117-124.
4. Khoo V, Dearnaley DP, Finnigan DJ, Padhani A, Tanner SF, Leach MO. Magnetic resonance imaging: considerations and applications in radiotherapy treatment planning. *Radiother Oncol* 1997;42:1-15.
5. Heester M, Wijrdeman HK, Strukmans H, Witkamp T, Moerland MA. Brain tumor delineation based on CT and MR imaging. *Strahlenther Onkol* 1993;169:729-733.
6. Bradley W, Waluch V, Yadley RA, Wycoff RR. Comparison of CT and MR in 400 patients with suspected disease of the brain and cervical spinal cord. *Radiology* 1984;152:695-702.
7. Brant-Zawadzki M. MR imaging of the brain. *Radiology* 1988;166:1-10.
8. Thorton A, Sandler MD, Ten Haken RK, McShan DL, Fraas BA, LaVigne ML, Yanke BR. The clinical utility of magnetic resonance imging in 3-dimensional treatment planning of brain neoplasms. *Int J Radiat Oncol Biol Phys* 1992;24:767-775.
9. Fraass B, McShan DL, Diaz RF, Ten Haken RK, Aisen A, et al. Integration of magnetic resonance imaging into radiation therapy treatment planning: I technical considerations. *Int J Radiat Oncol Biol Phys* 1987;13:1897-1908.
10. Purdy J. Principals and Practice of Radiation Oncology. 3 ed: Lippincott-Raven; 1997.
11. Stanescu T, Syme A, Pervez N and Fallone B G. MRI-based treatment planning for radiotherapy of brain lesions. [Abstract]. *Med Phys* 2005;32:2033.

12. Stanescu T, Jans H-S, Stavrev P and Fallone B G. 3T MR-based treatment planning for radiotherapy of brain lesions. *Radiol Oncol* 2006;40:125-132.

13. Stanescu T, Jans H-S, Stavrev P, Fallone BG. A Complete MR-Based Treatment Planning Procedure for Radiotherapy of Intracranial Lesions. [Abstract]. *Med Phys* 2006;33:2271.

14. Stanescu T, Jans H, Pervez N, Stavrev P, Fallone BG. Developments in MRI Simulation of Intracranial Lesions. [Abstract]. *Radiother Oncol* 2007;84:S18.

15. Chen L, Price R A Jr, Wang L, Li J, Qin L, McNeeley S, et al MRI-based treatment planning for radiotherapy: dosimetric verification for prostate IMRT. *Int. J. Radiat. Oncol. Biol. Phys.* 2004;60:636-647.

16. Chen L, Price Jr. RA., Nguyen T-B, et al. Dosimetric evaluation of MRI-based treatment planning for prostate cancer. *Phys Med Biol* 2004;49:5157-5170.

17. Chen Z, Ma CM, Paskalev K, Li J, Yang J, Richardson T, Palacio L, Xu X and Chen L. Investigation of MR image distortion for radiotherapy planning of prostate cancer. *Phys Med Biol* 2006;51:1393-1403.

18. Lee YK, Bollet M, Charles-Edwards G, Flower M A, Leach M O, McNair H, et al. Radiotherapy treatment planning of prostate cancer using magnetic resonance imaging alone *Radiother. Oncol.* 2003;66:203-216.

19. Chen L, Nguyen TB, Jones E, Chen Z, Luo W, Wang L, Price RA, Pollack A, Ma CM. Magnetic resonance-based treatment planning for prostate intensity-modulated radiotherapy: creation of digitally reconstructed radiographs. *Int J Rad Oncol Biol Phys* 2007;68:903-911.

20. Schad L, Lott S, Schmitt F, et al. Correction of spatial distortion in MR Imaging: A prerequisite for accurate stereotaxy. *J Comput Assist Tomo* 1987;11:499-505.

21. Moerland M. Magnetic resonance imaging in radiotherapy treatment planning: PhD thesis, University of Utrecht, The Netherlands; 1996.

22. Bakker CJG, Moerland M A, Bhagwandien R and Beersma R. Analysis of machine-dependent and object-induced geometric distortion in 2DFT MR imaging. *Mag. Reson. Imag* 1992;10:597-608.

23. Chang H, Fitzpatrick JM. A technique for accurate magnetic resonance imaging in the presence of field inhomogeneities. *IEEE T Med Imaging* 1992;11:319-329.

24. Bakker C, Moerland MA, Bhagwandien R and Beersma R. Analysis of machine-dependant and object-induced geometric distortion in 2DDT MR imaging. *Magn. Reson. Imaging* 1992;10:597-608.

25. Hill D, et al. Accurate frameless registration of MR and CT images of the head; applications in planning surgery and radiation therapy. *Radiology* 1994;191:447-454.

26. Just M, Rosler HP, Higer HP, Kutzner J, Thelen M. MRI-assisted radiation therapy planning of brain tumors - clinical experience in 17 patients. *Magn Res Imag* 1991;9:173-177.

27. Bhagwandien R. Object induced geometry and intensity distortions in magnetic resonance imaging: PhD thesis, University of Utrecht, The Netherlands; 1994.

28. Doran SJ, Charles-Edwards L, Reinsberg S A and Leach M O. A complete distortion correction for MR images: I. Gradient warp correction. *Phys. Med. Biol.* 2005;50:1343-1361.

29. Wang D, Doddrell D M and Cowin G. A novel phantom and method for comprehensive 3-dimensional measurement and correction of geometric distortion in magnetic resonance imaging. *Mag. Res. Imag.* 2004;22:529-542.

30. Wang D, Strugnell W, Cowin G, Doddrell D M, Slaughter R. Geometric distortion in clinical MRI systems Part 1: evaluation using a 3D phantom. *Mag Res Imag* 2004;22:1211-1221.

31. Sumanaweera T, Adler JR, Napel S, et al. Characterization of spatial distortion in magnetic resonance imaging and its implications for stereotactic surgery. *Neurosurgery* 1994;35:696-704.

32. Stanescu T, Jans H, Fallone BG. Investigation of a 3D MR Distortion Correction Protocol. [Abstract]. *Med Phys* 2006;33:2658

33. Baldwin L, Wachowicz K, Thomas SD, Rivest R, Fallone BG. Characterization, prediction, and correction of geometric distortion in 3 T MR images. *Med Phys* 2007;34:388-399.

34. Janke A, Zhao H, Cowin GJ, Galloway J, Dodrell DM. Use of spherical harmonic deconvolution methods to compensate for nonlinear gradient effects on MRI images. *Mag Res Med* 2004;52:115-122.

35. Beavis A, Gibbs P, Dealey RA, Whitton VJ. Radiotherapy treatment planning of brain tumors using MRI alone. *Br J Rad* 1998;71:544-548.

36. Amanie J, Robinson D, Murray B, Field C, Warkentin B, Stavrev P, et al. Comparison of dose-escalated and intensity- modulated three-dimensional conformal radiotherapy plans in patients with localized non-small-cell lung cancer. *Curr Oncol* 2004;11:93.

37. Bhagwandien R, Moerland MA, Bakker CJ, Beersma R, Lagendijk JJ. Numerical analysis of the magnetic field for arbitrary magnetic susceptibility distributions in 3D. *Mag Res Imag* 1994;12:101-107.

38. Moerland M, Beersma R, Bhagwandien R, Wijrdeman HK, Bakker CJG. Analysis and correction of geometric distortions in 1.5 T magnetic resonance images for use in radiotherapy treatment planning. *Phys Med Biol* 1995;40:1651-1664.

39. Stephen M, Jenkinson M, Woolrich MW, Beckmann CF, Behrens TEJ et al. Advances in functional and structural MR image analysis and implementation as FSL. *NeuroImage* 2004;23:208-219.

40. Collins D, Neelin P, Peters TM and Evans AC. Automatic 3D Inter-Subject Registration of MR Volumetric Data in Standardized Talairach Space. *Journal of Computer Assisted Tomography* 1994;18:192-205.

41. Collins D, Holmes CJ, Peters TM, and Evans AC. Automatic 3D model-based neuroanatomical segmentation. *Human Brain Mapping* 1995;3:190-208.

42. Ashburner J, Friston KJ. Unified segmentation. *Neuroimage* 2005;26:839-851.

43. Brahme A. Dosimetric precision requirements in radiation therapy. *Acta Radiol Oncol* 1984;23:379-391.

44. Carlone M, Warkentin B, Stavrev P, Fallone B G. Fundamental form of the population TCP model in the limit of large heterogeneity. *Med Phys* 2006;33:1634-1642.

45. Ramsey C, Oliver AL. Magnetic resonance imaging based digitally reconstructed radiographs, virtual simulation, and three-dimensional treatment planning for brain neoplasms. *Med Phys* 1998;25.

46. Ramsey C, Cordrey IL, Spencer KM, Oliver AL. Dosimetric verification of two commercially available three-dimensional treatment planning systems using TG23 test package. *Med Phys* 1999;26:1188-1195.

47. Schad L, Bluml S, Hawighorst H, Wenz F, Lorenz W. Radiosurgical treatment planning of brain metastases based on a fast, three-dimensional MR imaging technique. *Magn Reson Imaging* 1994;12:811-819.

48. Ramsey C, Arwood D, Scaperoth D, Oliver AL. Clinical application of digitally-reconstructed radiographs generated from magnetic resonance imaging for intracranial lesions. *Int J Radiat Oncol Biol Phys* 1999;45:797-802.

49. Chen L, Thai-Binh N, Elan MS, Chen Z, Wei L, Lu W, Price RA., Pollack A, Ma C. Magnetic resonance-based treatment planning for prostate intensity-modulated radiotherapy: creation of digitally reconstructed radiograhs. *Int J Radiat Oncol Biol Phys* 2007;68:903-911.

50. Yin F, Gao Q, Xie H, Nelson D, Yu Y, et al. MR image-guided portal verification for brain treatment field. . *Int J Radiat Oncol Biol Phys* 1998;40:703-711.

51. Fallone B, Carlone M, Murray B, Rathee S, Stanescu T, Steciw S, Wachowicz K, Kirkby C. Development of a Linac-MRI System for Real-Time ART. [Abstract]. *Med Phys* 2007;34:2547.

52. Lagendijk J, Raaymakers BW, van der Heide U, Overweg J, Brown K et al. In Room Magnetic Resonance Imaging Guided Radiotherapy (MRIgRT). *Med Phys* 2005;32:2067

CHAPTER 4.
DOSIMETRIC CALCULATIONS AND MAGNETIC SHIELDING CONSIDERATIONS FOR AN MRI-LINAC SYSTEM

4.1 INTRODUCTION

In recent years, the concept of integrating a source of radiation such as a megavoltage radiation therapy Linac[1-6] or ^{60}Co unit[7-9] with an MRI scanner has emerged as a feasible novel approach for real time image guidance in adaptive radiotherapy, i.e. MRI guided radiation therapy (MRIgRT). Considering the MRI's excellent soft-tissue contrast and its ability to perform multi-planar data acquisition, MRIgRT would be characterized by improved visualization of the target and neighboring anatomy, ultimately facilitating on-line treatment plan optimization. The main benefits of using MRIgRT are expected to include a reduction of the safety margins and a higher local tumor control leading to reduced normal tissue complications.

At Cross Cancer Institute, we are investigating a novel MRI-Linac system consisting of a bi-planar 0.2 T permanent magnet coupled with a 6 MV Linac.[5, 10-15] The system can freely revolve axially around the patient yielding multiple x-ray beams that can be delivered from any desired angle. In this chapter, we examine two important aspects of the proposed MR-Linac system, specifically a) dosimetric effects due to the presence of an external magnetic field (Section 4.2) and b) magnetic shielding of the Linac (Section 4.3).

4.2 DOSIMETRIC CALCULATIONS IN THE PRESENCE OF AN EXTERNAL MAGNETIC FIELD

In this section, we investigate the effects induced by an external magnetic field ($\vec{B}_0$) on the dose deposition of a 6 MV beam in semi-infinite slab-based phantoms by means of Monte Carlo methods. Specifically, we simulate the electron return effect (ERE)[2, 4] in several media with significantly different x-ray attenuation properties, i.e. air, water, lung. This study represents the

ground work of a larger project (Kirkby *et al*[16]) aimed to quantify the magnetic field induced effects on the dose deposition process in patient brain and lung data.

ERE is caused by drastic change in the local behaviour of secondary electron transport which are generated in a medium by radiation (e.g. x-rays) due to the presence of an external magnetic field. As a consequence, the dose deposition patterns in the medium is also modified.[2-4, 17-20] Specifically, the trajectories of the electrons between subsequent collisions are modified (i.e. helical trajectory) depending on the electrons' kinetic energy and the applied field strength. In particular, the magnitude of this effect is enhanced at the interface of high-to-low electron density materials, e.g. tissue-air interface. The exit electrons describe a longer path in air than in tissue and can return to the tissue under the influence of an external magnetic field. As a consequence, the tissue exit dose may increase compared to the case of no magnetic field.[2, 4] The magnitude of the ERE effect is dependent on the strength of the magnetic field, the electrons' velocities and the sample's geometry.

Our analysis extends from low (0.2 T) to high field strengths (1.5 T) for the case of two different MRI-Linac system configurations proposed in the literature, namely

a) A stationary solenoidal MRI with a radiation source rotating around it (Fig. 4.1a). In this geometry, $\vec{B}_0$ direction is towards the solenoid. The beam's relative orientation with regard to the magnetic field's direction varies as the radiation source rotates around the treatment volume. We will refer to this configuration as fixed cylindrical (FC) geometry. The FC arrangement was proposed for a 6 MV Linac mounted on a 0.25 T Helmholtz coils-based magnet[9] and a conventional 1.5 T MRI unit;[1, 2, 6]
b) A bi-planar MRI coupled rigidly with a source of radiation, both components rotating synchronously around the patient (Fig 4.1b). In this setup the beam and the magnetic field maintain the same relative orientation, i.e. perpendicular to each other, during the system's rotation. Thus $\vec{B}_0$ changes its direction with respect to the patient. This

configuration will be referred as the rotating bi-planar (RBP) geometry. A system based on this concept was proposed for a standard 6 MV accelerator integrated with a 0.2 T permanent magnet.[5, 10-12]

The two MRI-Linac hybrid configurations are characterized by essentially distinct mechanisms of dose delivery. Different dose patterns are expected to be generated due to different relative orientations of $\vec{B}_0$ and the radiation beam with regard to the subject.

To characterize the dose deposition of a 6 MV beam in samples placed in magnetic field we used penEasy (2006),[21] which is a modified version of PENELOPE (PENetration and Energy LOss of Positrons and Electrons).[22, 23] The accuracy of PENELOPE has been extensively tested in the literature.[23-26] The package consists of a FORTRAN 77-based Monte Carlo simulation package for the transport mechanism of photons, electrons and positrons in arbitrary geometries and materials. The algorithm relies on a composite scattering model suitable for a wide energy range (i.e. few hundred eV – 1 GeV) and is characterized by both numerical tables and analytical cross-section functions. PENELOPE implements a photon transport algorithm based on the conventional detailed method. The electrons and positrons interaction mechanisms are simulated as follows: a) the hard events are described in detail and b) soft events are described by multiple scattering methods, i.e. techniques base on the global effect of a large number of events confined in a certain step (or "condensed history"). PENELOPE's algorithm for the charged particles transport in static magnetic fields relies on the determination of the charged particles' field induced displacement and velocity change by computing the Lorentz force's impact on the particle's trajectory. It is assumed that the magnetic field effect can be accounted for independently of the transport step that would take place in the case of no magnetic field. Chen *et. al.*[25] showed that PENELOPE generated dose distributions are in good agreement with corresponding experimental data in the case of a plastic phantom placed in a non-uniform magnetic field with a peak strength of 3 T.

Compared to PENELOPE, penEasy allows the user to write a steering program that easily manipulates the source and tally parameters. However, penEasy relies on the same photon and electron transport subroutines implemented in PENELOPE. The simulations were controlled by means of the following parameters: W_{cc} representing the cut-off threshold for the hard inelastic collisions, W_{cr} defined as the cut-off threshold for the radiative events, C_1 defining the fraction by which the mean free path for hard elastic events can be defined by the first transport mean free path at high energies, and C_2 characterizing the maximum average fractional energy loss between consecutive hard elastic events.

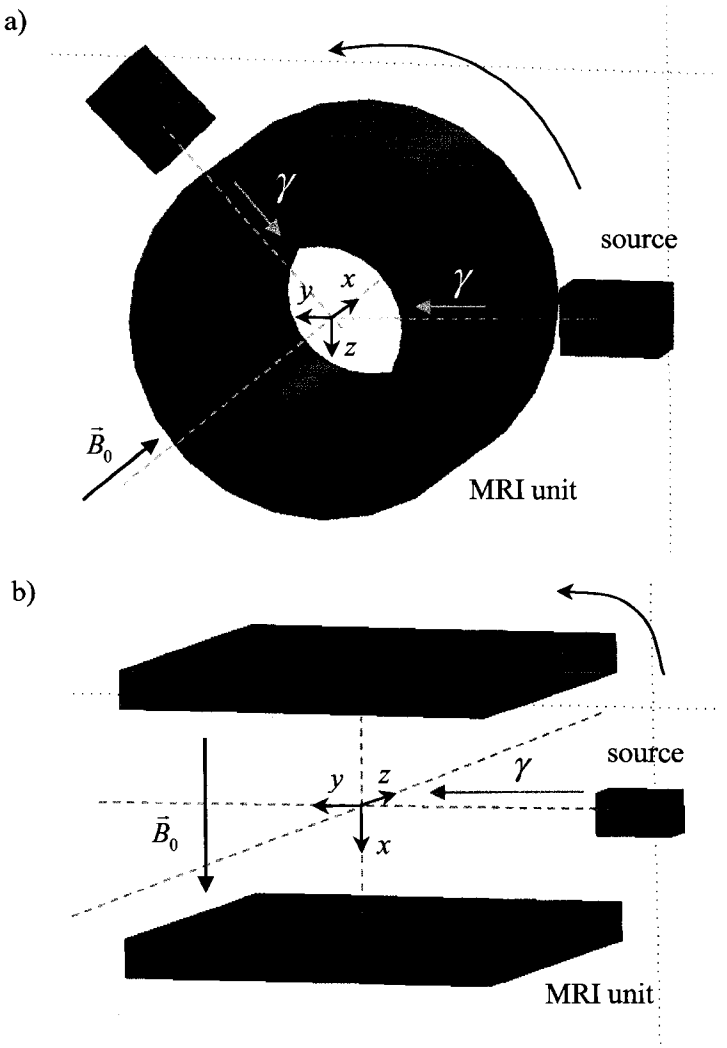

Figure 4.1. Proposed MRI-Linac system configurations: (a) FC geometry – the radiation source rotates around a fixed solenoidal MRI unit. $\vec{B}_0$ points towards the solenoid and its direction is constant with regard to patient's orientation; (b) RBP geometry – the radiation source is rigidly coupled with a bi-planar magnet. Both components rotate around the patient. $\vec{B}_0$ changes direction with regard to the subject but keeps the same relative orientation to the beam.

4.2.1 Materials and methods

4.2.1.1 Simulations on a computer cluster

The simulations were performed on a local computer cluster consisting of 22 nodes, each node containing 4 Opteron 2.0 GHz CPUs. The cluster is set up to run the Rocks (version 3.3.0) software package.[27] Briefly, Rocks, a modified Linux flavour (i.e. CentOS[28]), provides integral components such as Message Passing Interface (MPI)[29] tools for parallel programming.

Unfortunately, penEasy (or PENELOPE) was not designed to be MPI compatible. Therefore, it can not benefit from the parallel computing features offered by Rocks. To overcome this limitation, we operated penEasy through clonEasy,[30] i.e. an open-source library of Linux scripts and auxiliary FORTRAN applications. ClonEasy is designed to implement data exchange based on Secure Shell (SSH) connections between a primary computer node and an arbitrary number of secondary nodes.

The simulations were manipulated remotely via SSH from a workstation. After the simulation files (penEasy) are installed on the cluster's head computer along with clonEasy, the latter was utilized to subsequently upload, compile and execute the job files and to download the simulation results. These operations are performed simultaneously on all the cluster's nodes, i.e. clones. ClonEasy identifies uniquely the clones by their IP addresses. Also, it feeds independent seed values to the random number generator corresponding to each clone's job file. This ensures the implementation of independent sequences in individual CPUs leading to partial results that are statistically independent. For instant communication between the head computer and each clone, the cluster user account was set up to grant SSH access by means of public key authentication.

The simulation results were analyzed on the local workstation after the output files were transferred over the network. A typical output comprises of 48 tally files, i.e. 12 nodes of 4 CPUs

each, which were subsequently combined into a single global results file by using a data processing tool developed in Matlab.

4.2.1.2 Phantom geometry

The phantoms consisted of semi-infinite slabs of material as follows: a) water layer with a thickness of 18 cm, placed in air (Fig. 4.2a) and b) ICRP lung slab with a thickness of 10 cm, sandwiched between two 4 cm thick water layers and placed in air (Fig. 4.2b). The lung was assigned a mass density of 0.3 g/cm^3 and a chemical composition as per NIST.[31] We chose uniform lung material instead of air to simulate the dose induced effects of an external magnetic field in a realistic low density tissue. However, the lung slab represented only an approximation of the complex structure of real lung tissue. The simulations were performed by using single as well as two opposing and equally weighted non-diverging x-ray fields with a field size of 5 x 5 cm^2. The radiation source was characterized by a 6 MV central axis spectrum[32] corresponding to a Varian Linac. The simulation parameters were: W_{cc} = 60 keV, W_{cr} = 6 keV, and $C_1 = C_2 = 0.1$. The choice of these values offer reasonable simulation efficiency without compromising the accuracy of the simulation results.[21] The dimensions of the dose scoring voxels were 0.2 × 0.2 × 1.0 cm^3. A sufficient number of histories were considered to achieve < 1 % statistical uncertainty for the dose to water along the central axis. In both RBP and FC geometries, the magnetic field and the radiation beam were simulated along the x and z axes, respectively (see Fig. 4.1). As a result, the Lorentz force pointed along the y-axis. In the next section, the (y,z) plane refers to the respective (y,z) planes in the RBP or FC configuration.

4.2.2 Results

4.2.2.1 Water phantom

Figure 4.3 shows the relative dose distributions in the plane perpendicular to the external magnetic field ($\vec{B}_0$) containing the central axis, generated by a 6 MV beam incident on a water phantom. The dose values were normalized to the central axis value at 1.5 cm depth (i.e. D_{max}) in water corresponding to the zero magnetic field case (Fig. 4.3a). Compared to the 0 T map, the 0.2 T and 1.5 T distributions shown in Figs. 4.3b and 4.3c, respectively, do not exhibit *z*-axial symmetry, specifically the dose is shifted to a certain extent in the direction of the Lorentz. By increasing the field strength the trajectories of the secondary electrons, which are responsible for the dose deposition process, are altered to a higher degree. For the 1.5 T case most of the electrons exiting the phantom return to the water slab, increasing the dose at the water-air interface due to the ERE effect. Figure 4.4 displays the dose distributions in a 3D manner to better visualize the 2D dose profile gradient. The exit dose peaks corresponding to the 0.2 T and 1.5 T cases are clearly depicted.

Figure 4.5 (a) and (b) show a comparison of the 1D dose profiles along the central axis corresponding to 0 T, 0.2 T and 1.5 T cases and the $D_{0.2T} - D_{0.0T}$ and $D_{1.5T} - D_{0.0T}$ percent difference profiles, respectively. In the water slab the 1.5 T profile appears to be shifted about 3-4 mm towards the air-to-water interface compared to the 0 T case (Fig. 4.5a). This change in dose deposition translates into an entrance dose to water increase of about 10 % (Fig. 4.5b). Also, for the 1.5 T case, there is a sharp dose increase of about 20 % at the water-to-air interface. In contrast, there is little difference between the low field (0.2 T) and 0 T profiles inside the water layer. At the water-to-air boundary, in the last voxel, there is a 6 % discrepancy (Fig 4.5b). By increasing the field strength the dose in the air layer located beyond the water slab decreases.

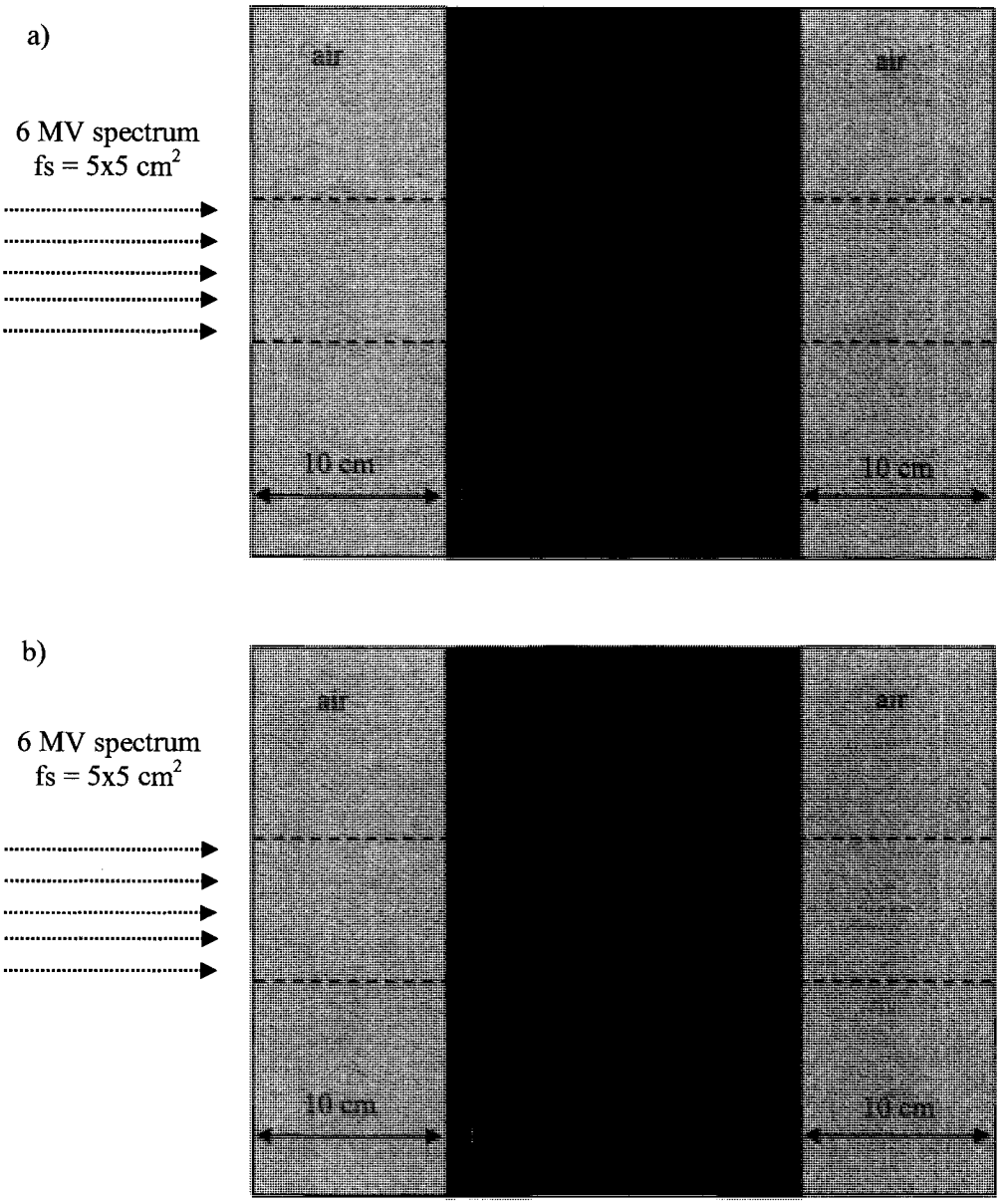

Figure 4.2. The phantoms consist of semi-infinite slabs of material: (a) water layer in air; (b) water-lung-water slabs in air. The field size of the incident 6 MV beam was 5 x 5 cm^2.

In Fig. 4.6 the dose difference maps, i.e. $D_{0.2T} - D_{0.0T}$ and $D_{1.5T} - D_{0.0T}$, along the central axis plane are displayed. It is important to show these maps in addition to the 1D profiles (Fig. 4.5a) as the dose distribution does not have axial symmetry, specifically hot or cold spots might be present at the edge of the field. The $D_{0.2T} - D_{0.0T}$ map shows that for a 0.2 T field the dose distribution in the water layer is shifted upward (with regard to the page orientation) generating a hot and a cold stripe (~ 4 mm wide) along the upper and lower edge of the field, respectively. The maximum dose difference in these regions is < 5 %. The $D_{1.5T} - D_{0.0T}$ map shows a similar effect; the intensity of the hot and cold stripes is +23 % and -20 %, respectively. Decreasing the field strength, the electrons tend to travel a longer distance in the air slab. Considering this effect, at 0.2 T the secondary electrons exiting the water layer return in the proximity of the radiation field region and contribute to a hot spot with a maximum of < 25 %. In contrast, at high field (1.5 T) the exiting electrons return back to the water slab mostly within the radiation field region after traveling a much smaller distance generating a hot stripe with a maximum of about 30%.

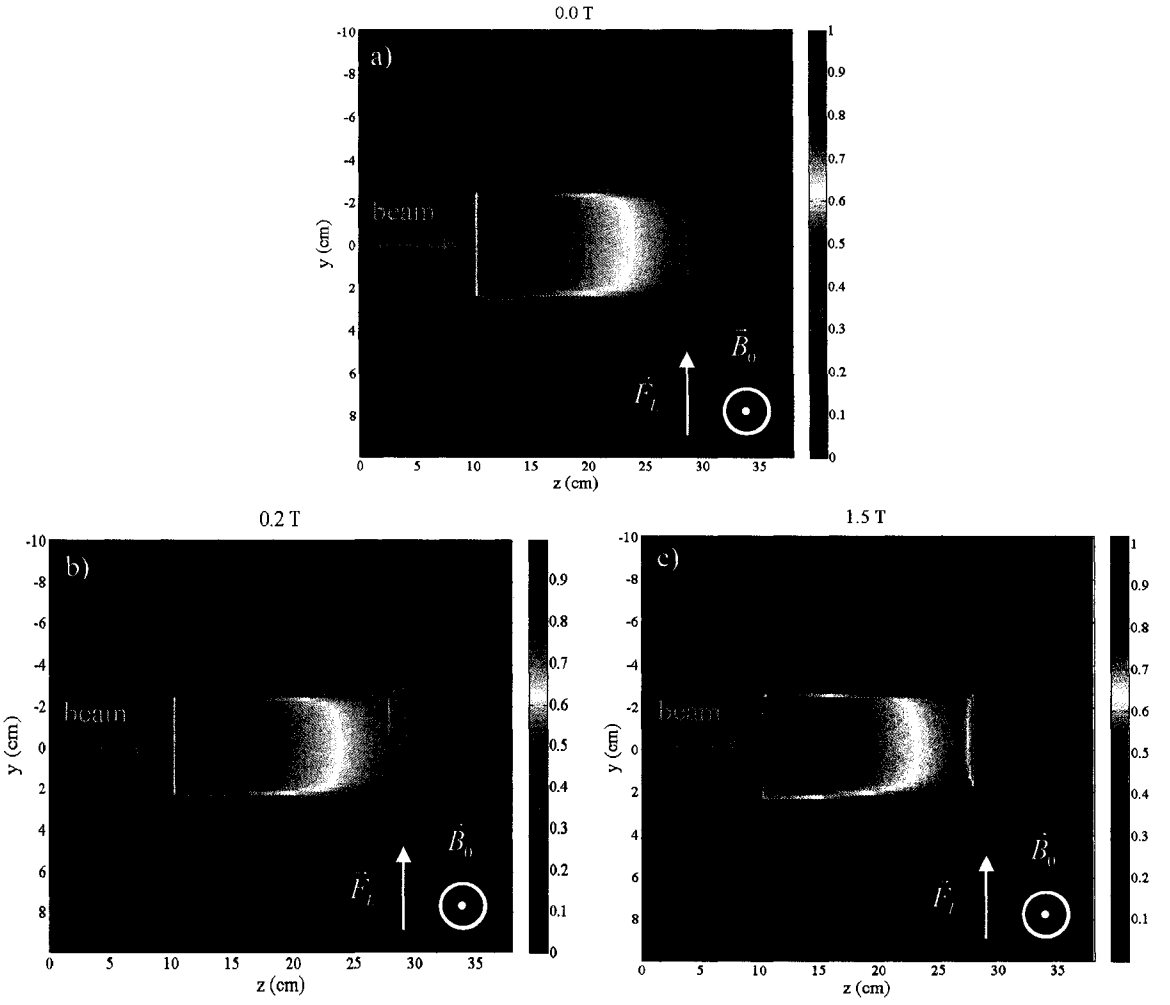

Figure 4.3. Relative dose distribution in the central plane for a 6 MV photon beam incident on a water phantom. The strength of the static magnetic field is (a) 0 T, (b) 0.2 T and (c) 1.5 T. The 6 MV beam enters the phantom from left hand side. For panels (b) and (c) the dose distributions are shifted along the direction of the Lorentz force (F_L) compared to the no field case.

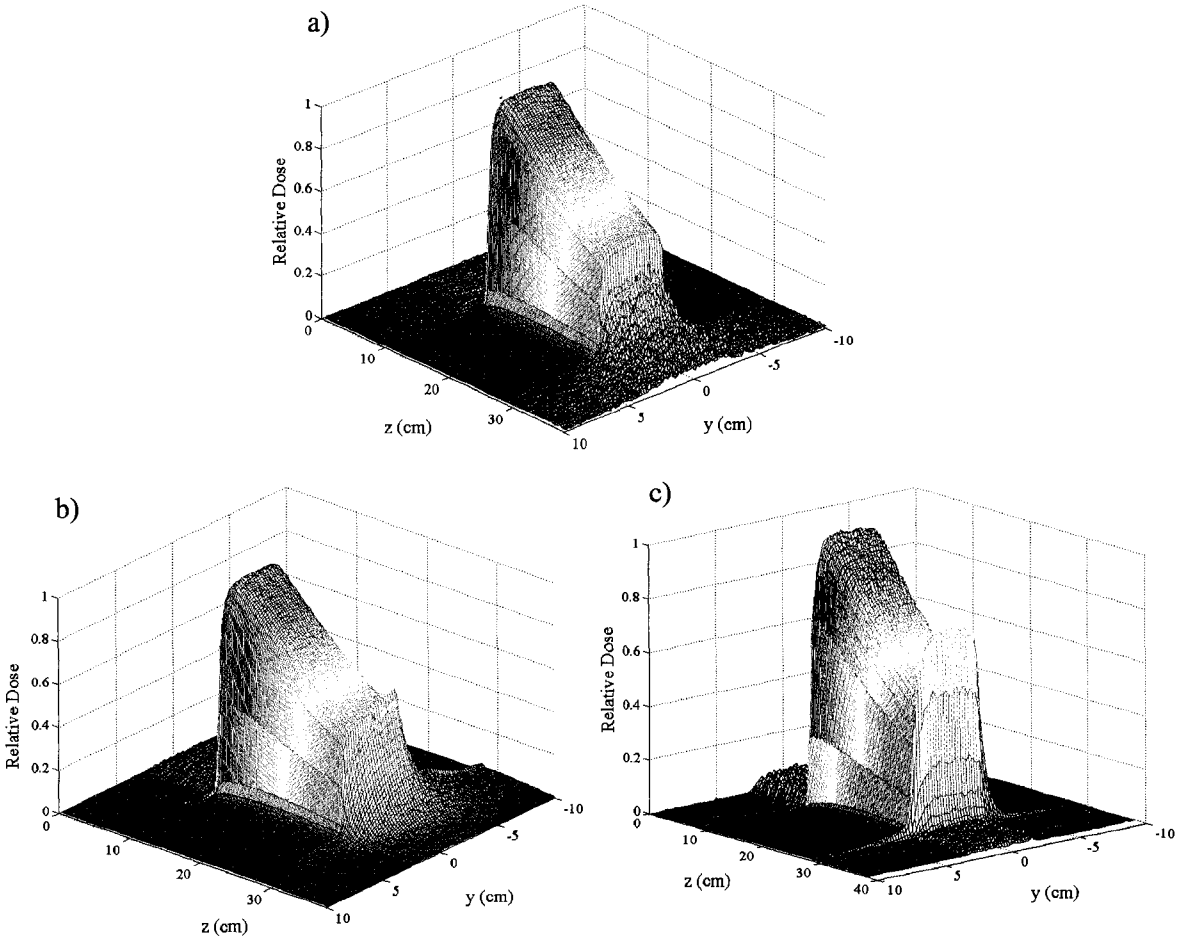

Figure 4.4. 3D visualization of the relative dose distribution in the central plane of Fig. 4.3. The magnetic field strength is (a) 0 T, (b) 0.2 T and (c) 1.5 T. The exit dose peaks are clearly depicted for the 0.2 T and 1.5 T cases.

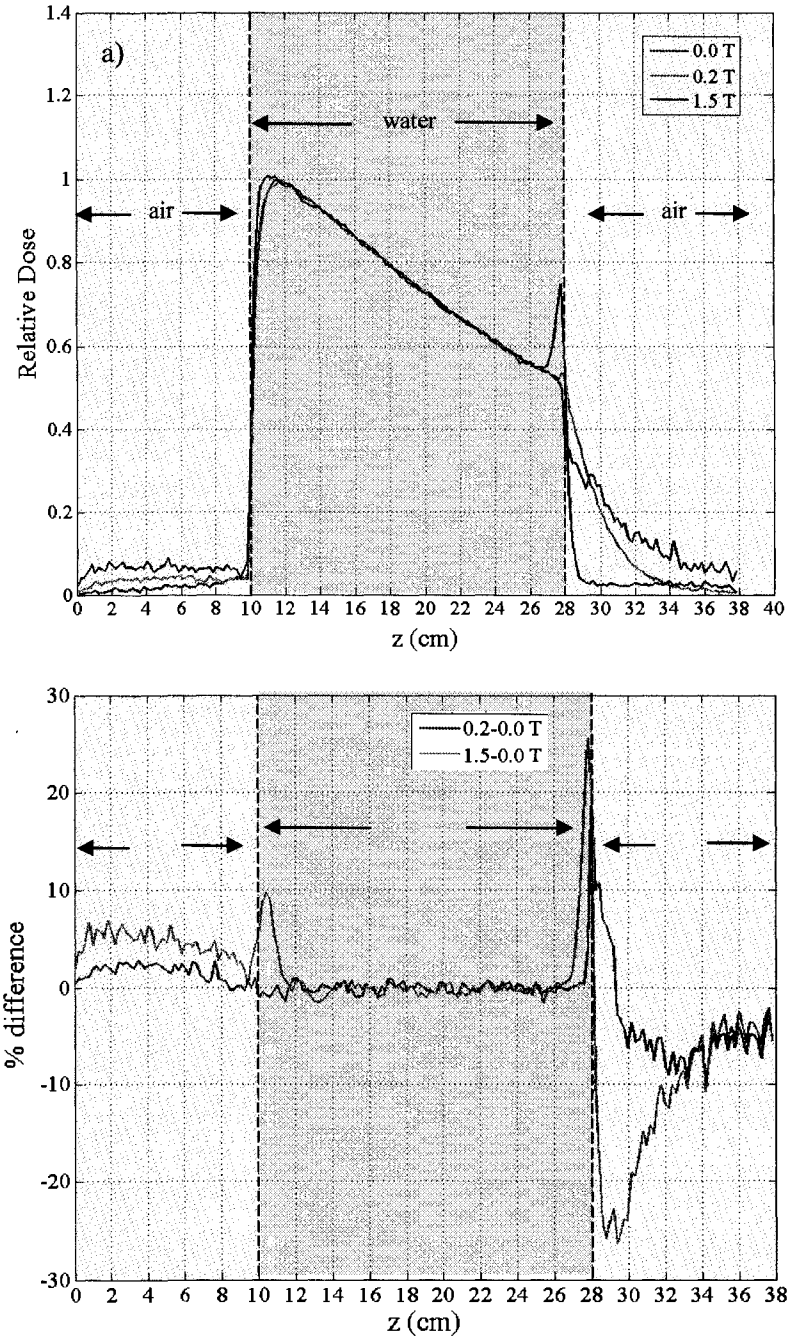

Figure 4.5. 1D profiles along the central axis of the phantom: (a) relative dose for 0 T, 0.2 T and 1.5 T cases; (b) percent difference profiles corresponding to $D_{0.2T} - D_{0.0T}$ and $D_{1.5T} - D_{0.0T}$. Dose values in (a) were normalized to D_{max} in water for the 0 T case.

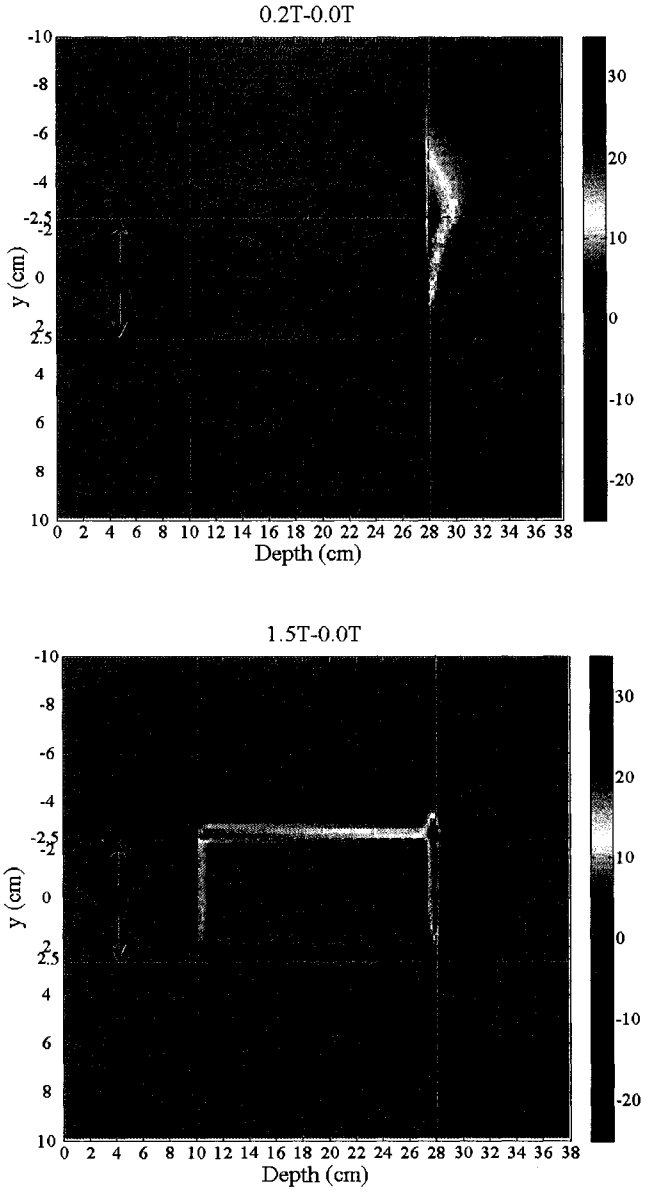

Figure 4.6. 2D dose difference maps are shown in (a) $D_{0.2T} - D_{0.0T}$ and (b) $D_{1.5T} - D_{0.0T}$.

Figure 4.7 shows the relative dose distributions along the central axis plane for two parallel opposing fields. The no field case is presented as a reference (Fig. 4.7a). Figs. 4.7 (b) and (c) correspond to the 0.2 T case in the RBP and FC configurations, respectively. In the RBP geometry the dose distribution shift is in the direction of the Lorentz force and remains the same. By comparison, in the FC geometry the ERE effects caused by the two equally weighted opposing fields tend to cancel each other out due to a reversed orientation of the Lorentz force. Similar maps were generated for the 1.5 T case (not shown). In Fig. 4.8, the cumulative effect of the individual maps (Fig. 4.7) is shown. By taking a 1D profile along the central axis, we find that there is no significant difference between the cumulative effect of two parallel opposing pair (POP) fields in the RBP and FC geometries at either 0.2 T or 1.5 T, as depicted in Fig. 4.9. The effect of maximum dose peak shift to shallower depths characteristic of the 1.5 T case results in a 15 % dose difference (with regard to 0 T case) increase at both air-to-water and water-to-air interfaces. In contrast, at 0.2 T there is only a small increase in dose (< 5 % over 4 mm) at both air and water boundaries. It is interesting to note that the 0.2 T and 0 T cases are in good agreement even in the adjoining air regions. At 1.5 T the dose in the adjoining air regions drops rapidly compared to the no field case (up to 12 %).

In Fig. 4.10, $D_{0.2T} - D_{0.0T}$ and $D_{1.5T} - D_{0.0T}$ maps for POP fields show the distribution of the hot and cold regions in the RBP and FC configurations, respectively. The differences between the two geometries are clearly depicted. Depending on the direction of the Lorentz force, at 0.2 T the dose-to-air hot spots are located on the same and opposite side of the incident fields for the RBP and FC geometry, respectively. Inside the water slab, there is no significant difference for the FC configuration as the ERE effects generated by the opposing beams cancel each other out (Fig. 4.10b). In contrast, the RBP geometry presents hot and cold regions (< 6 %) along the edges of the fields (Fig. 4.10a), which is a consequence of the combined ERE effects induced by the fields. At 1.5 T, the RBP geometry map shows lateral hot (~ 20 %) and cold (~ 15 %) regions. Also, hot regions (< 15 %) are present at both water and air interfaces. For the FC geometry we

see a similar pattern for the water entrance and exit regions. However, the lateral stripes are less intense (< 8 %) than in the RBP configuration.

4.2.2.2 Water-lung-water phantom

Compared to the water phantom case, the presence of the lung layer inside the water slab significantly alters the dose deposition process. Lung has a lower density than water and thus important ERE effects are expected to be present in the medium especially at the water-to-lung and lung-to-water interfaces.

Figure 4.11 shows the relative dose distributions in the same central axis plane as for the water phantom. The dose values were normalized to D_{max} in water corresponding to the no field case (Fig. 4.11a). Increasing the field strength, the dose deposited in the lung slab suffers a larger shift in the direction of the Lorentz force (Figs. 4.11b and 4.11c). Figure 4.12a shows that due to the return effect in the lung slab there are two additional peaks present in the phantom as compared to the water only case (Fig. 4.5a). Specifically, in the case of a 1.5 T field, at the water-to-lung boundary there is a relative dose increase of 28 % to water and 40 % to lung and at the lung-to-water interface a relative dose decrease of 26 % to lung and 24 % to water. For 0.2 T the $D_{0.2T} - D_{0.0T}$ dose differences are generally within ± 2.5 %. The dose distributions due to the return effect at the air-to-water and water-to-air interfaces are the same as for the case of a single water slab phantom (Fig. 4.5). In the lung layer, Figs. 4.13 show dose differences in the lateral regions, along the direction of the beam, with values of about ± 10 % at 0.2 T and ± 25 % for the 1.5 T case.

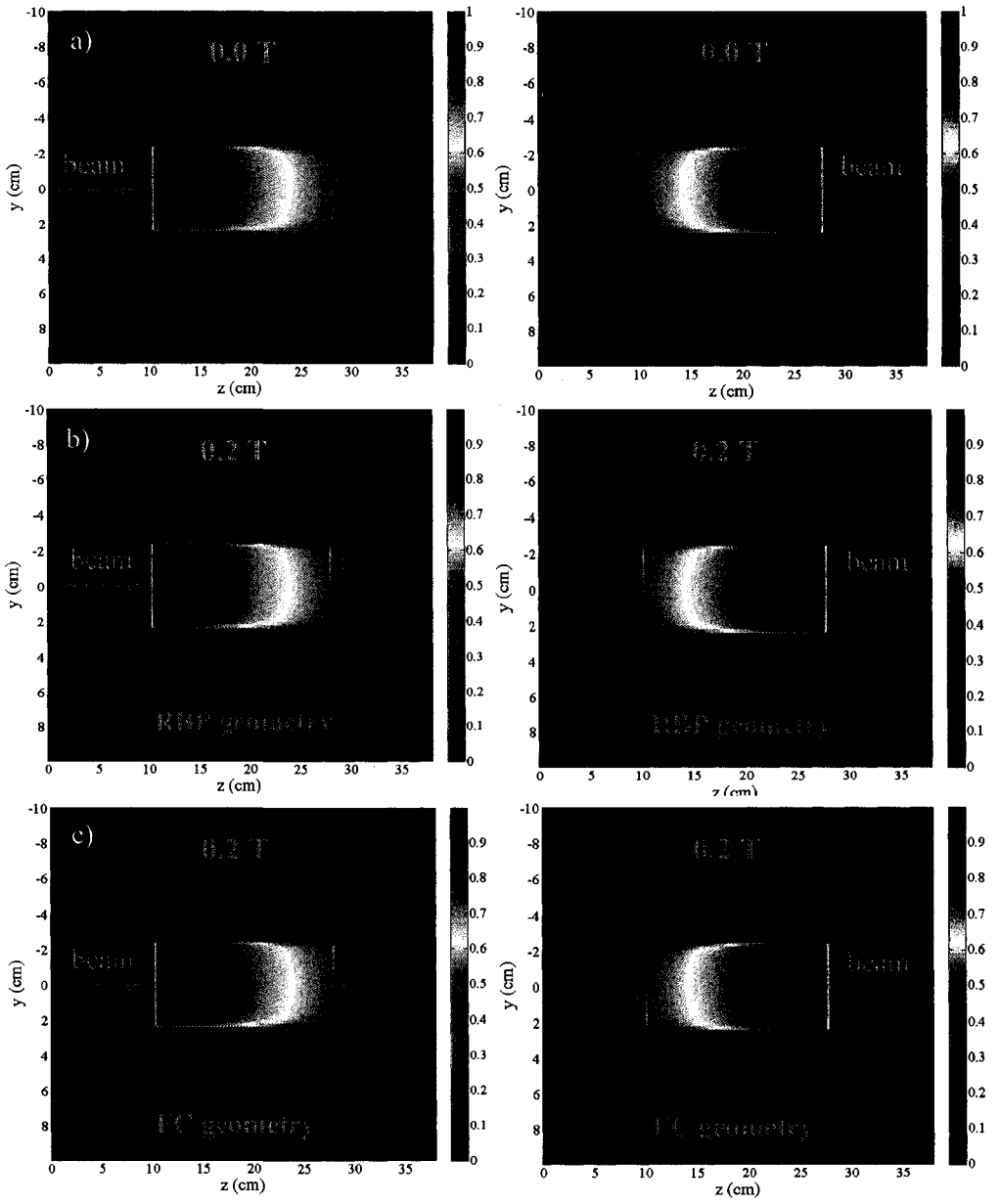

Figure 4.7. Relative dose distributions in the central plane corresponding to two 6 MV parallel opposing fields incident on a water phantom. (a) 0 T, (b) 0.2 T for the RBP geometry and (c) 0.2 T for the FC geometry.

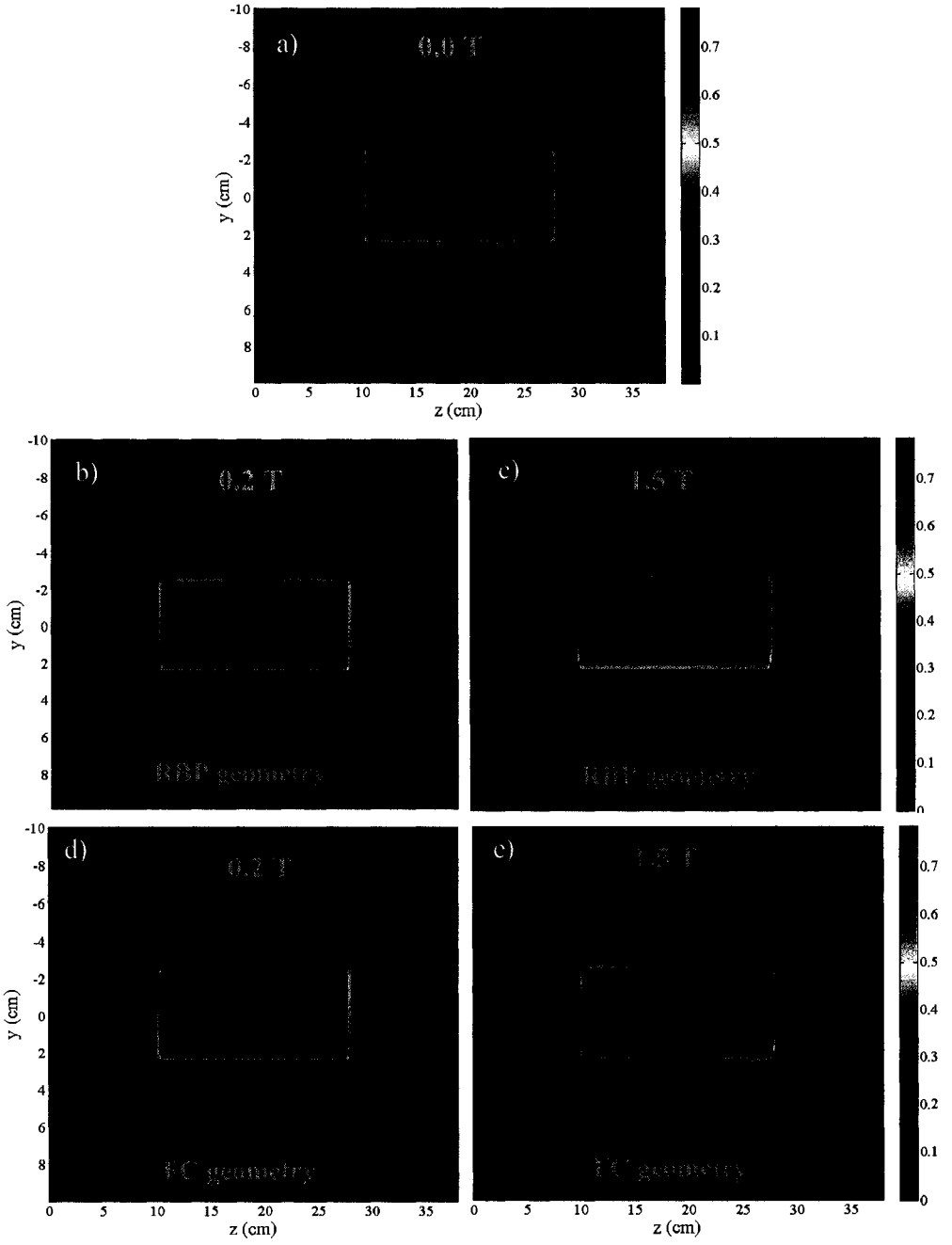

Figure 4.8. Cumulative relative dose distribution from two parallel opposing fields – (a) 0 T, (b) 0.2 T for RBP geometry, (c) 1.5 T for RBP geometry, (d) 0.2 T and FC geometry, (e) 1.5 T and FC geometry.

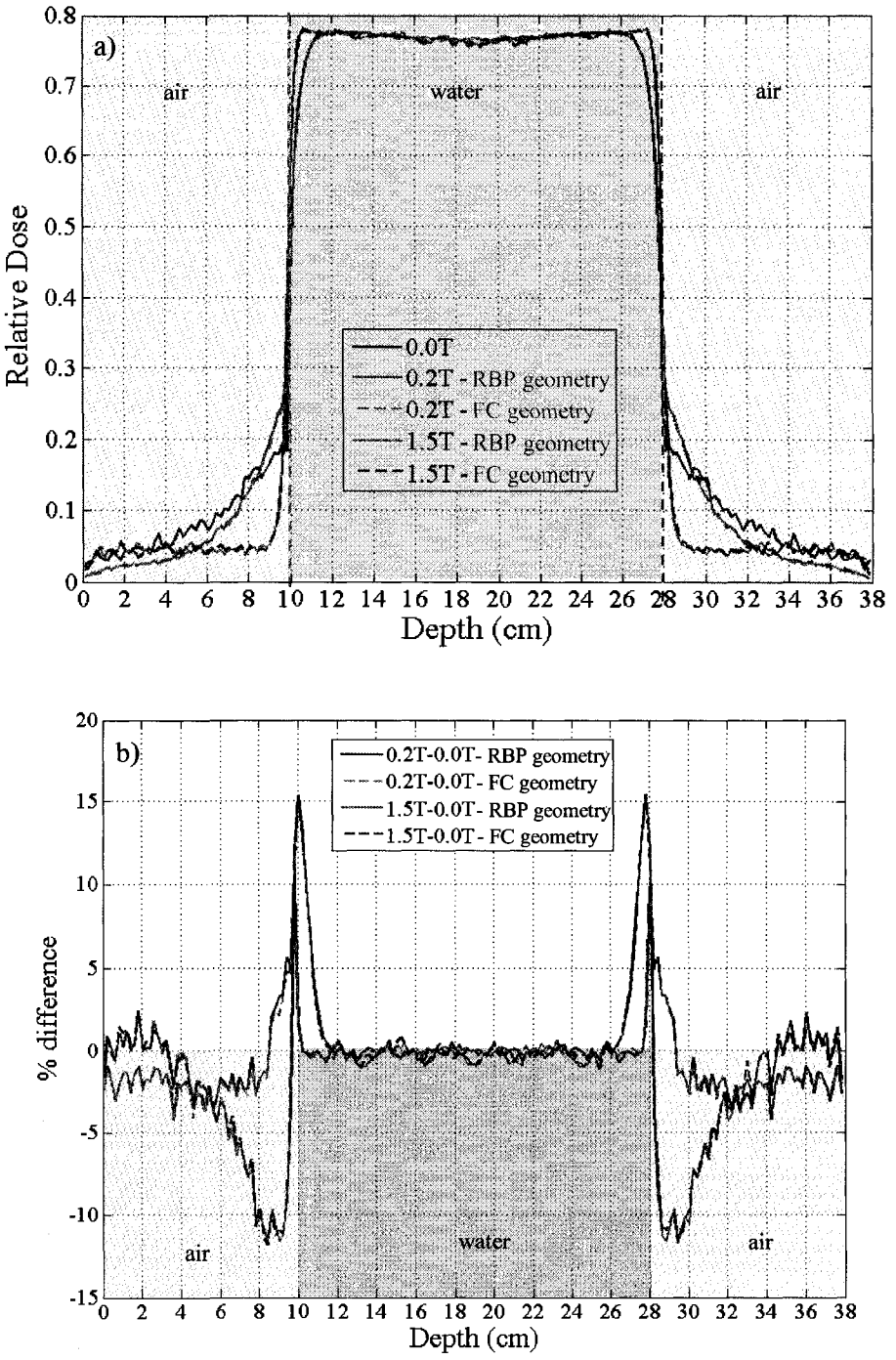

Figure 4.9. Central axis profile lines: (a) comparison between the RBP and FC system configurations for the 0.2 T and 1.5 T field strengths and no field, respectively; (b) dose difference profiles corresponding to $D_{0.2T} - D_{0.0T}$ and $D_{1.5T} - D_{0.0T}$ for the RBC and FC geometries.

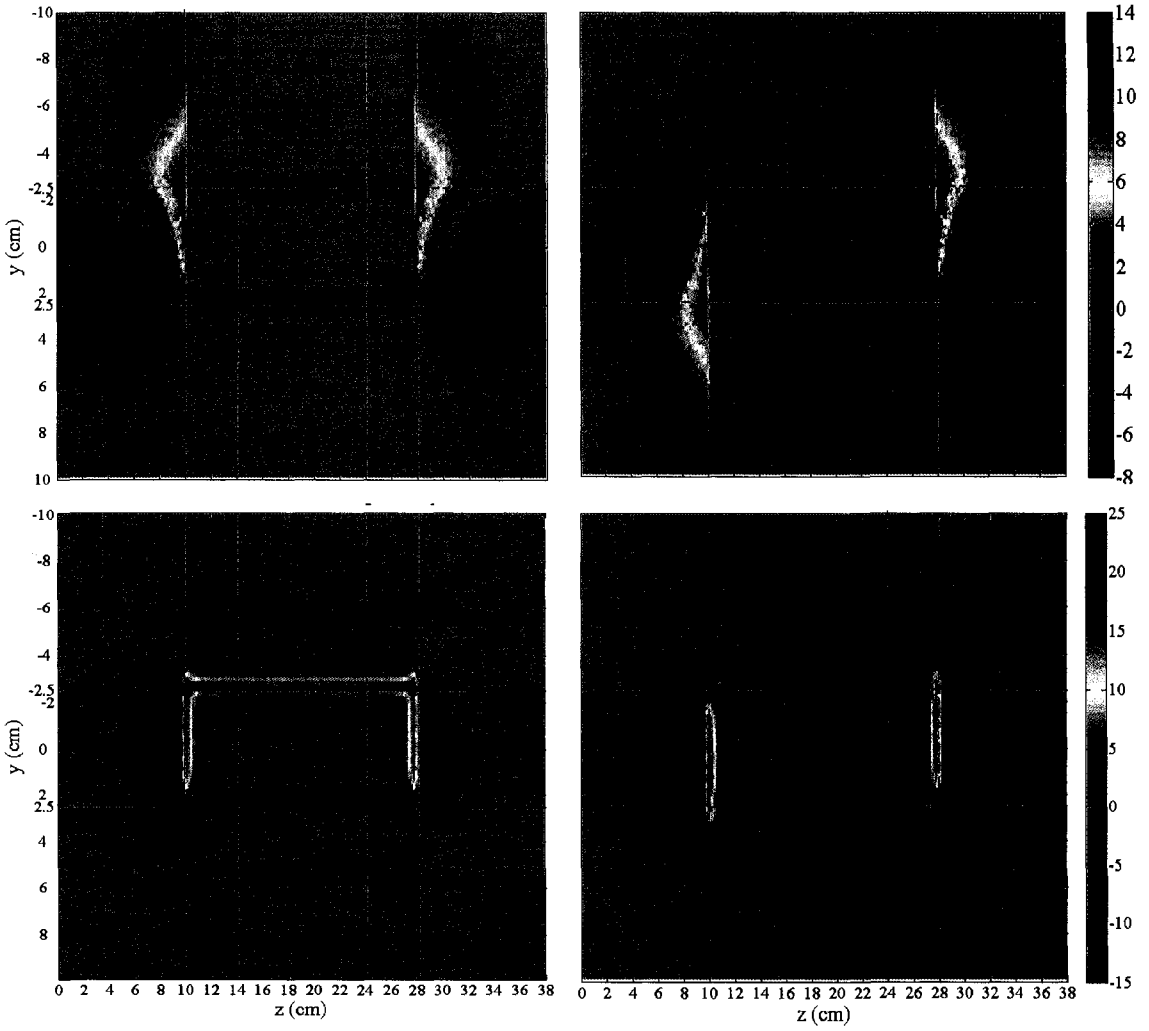

Figure 4.10. Relative 2D dose difference distributions (in percent) with respect to the no field case for: (a) 0.2 T and RBP geometry, (b) 0.2 T and FC geometry, (c) 1.5 T and RBP geometry, (d) 1.5 T and FC geometry.

Figures 4.14 show the cumulative dose distributions along the central axis plane corresponding to two equally weighted parallel opposing fields in both RBP and FC configurations for the water-lung-water phantom. The particular characteristics of both the RBP and FC geometries are highlighted, i.e. the dose distributions due to the beams' cumulative return effects. Figures 4.15 present the central axis profiles for the relative dose maps shown in Fig. 4.14 and the $D_{0.2T} - D_{0.0T}$ and $D_{1.5T} - D_{0.0T}$ dose difference profiles. At 1.5 T field, at the water-to-lung boundary there is a relative dose increase of 6 % to water and 8 % to lung and at the lung-to-water interface a relative dose increase of 8 % to lung and 2 % to water. For the same region, at 0.2 T the $D_{0.2T} - D_{0.0T}$ dose differences are generally within ± 2 %. Comparing Figs. 4.15b and 4.9b, we note that the insertion of the lung layer generated additional dose peaks at the water-to-lung and lung-to-water interfaces in the water-lung-water phantom.

Figures 4.16 show the difference maps $D_{0.2\,T} - D_{0.0\,T}$ and $D_{1.5\,T} - D_{0.0\,T}$ for the RBP and FC geometries, respectively. For the RBP configuration the dose distribution modifications due to the presence of a magnetic field are adding constructively. The electron return effect is more pronounced in the lung layer. As a consequence, in this material we observe lateral dose variations of about ± 12 % at 0.2 T, which is twice the effect in water (Fig. 4.10). Similarly, at 1.5 T the regions parallel to the magnetic field direction show variations up to ± 30 %. In the FC configuration the Lorentz forces point in opposite directions. At 0.2 T, in the lung material, the electron return effects from the two beams cancel each other out. However, at 1.5 T, due to a larger asymmetry in the dose distribution, distinct hot and cold spots (± 20 %) are present. Specifically, the hot and cold stripes seen in the case of a single beam (Fig. 4.11) at the water-to-lung and lung-to-water interfaces, respectively, are not fully compensated by the cold and hot regions corresponding to the opposite beam.

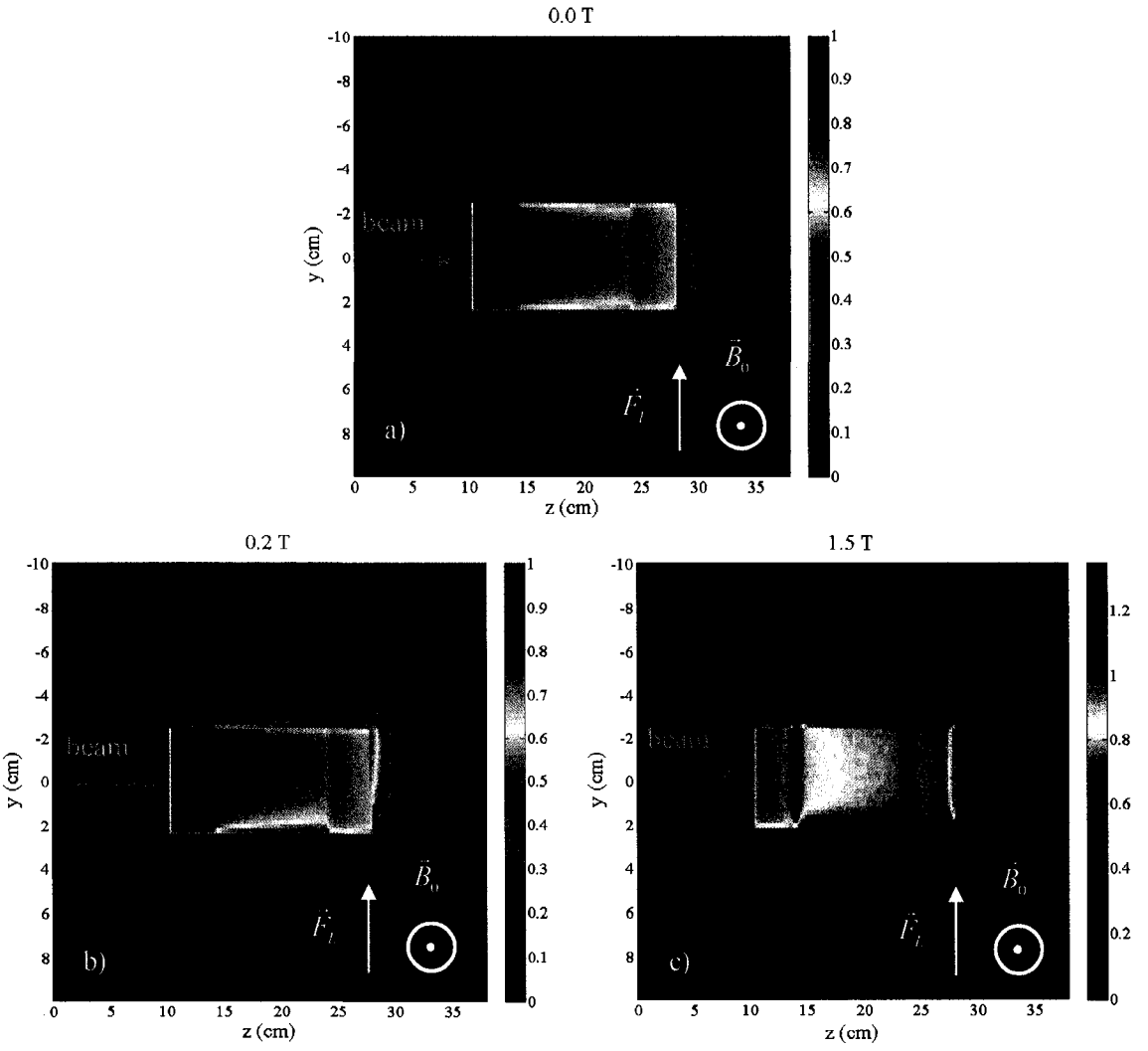

Figure 4.11. Relative dose distributions in the central plane for a 6 MV beam incident on a water-lung-water phantom. The strength of the static magnetic field is: (a) 0 T, (b) 0.2 T and (c) 1.5 T. The beam enters the phantom from the left hand side.

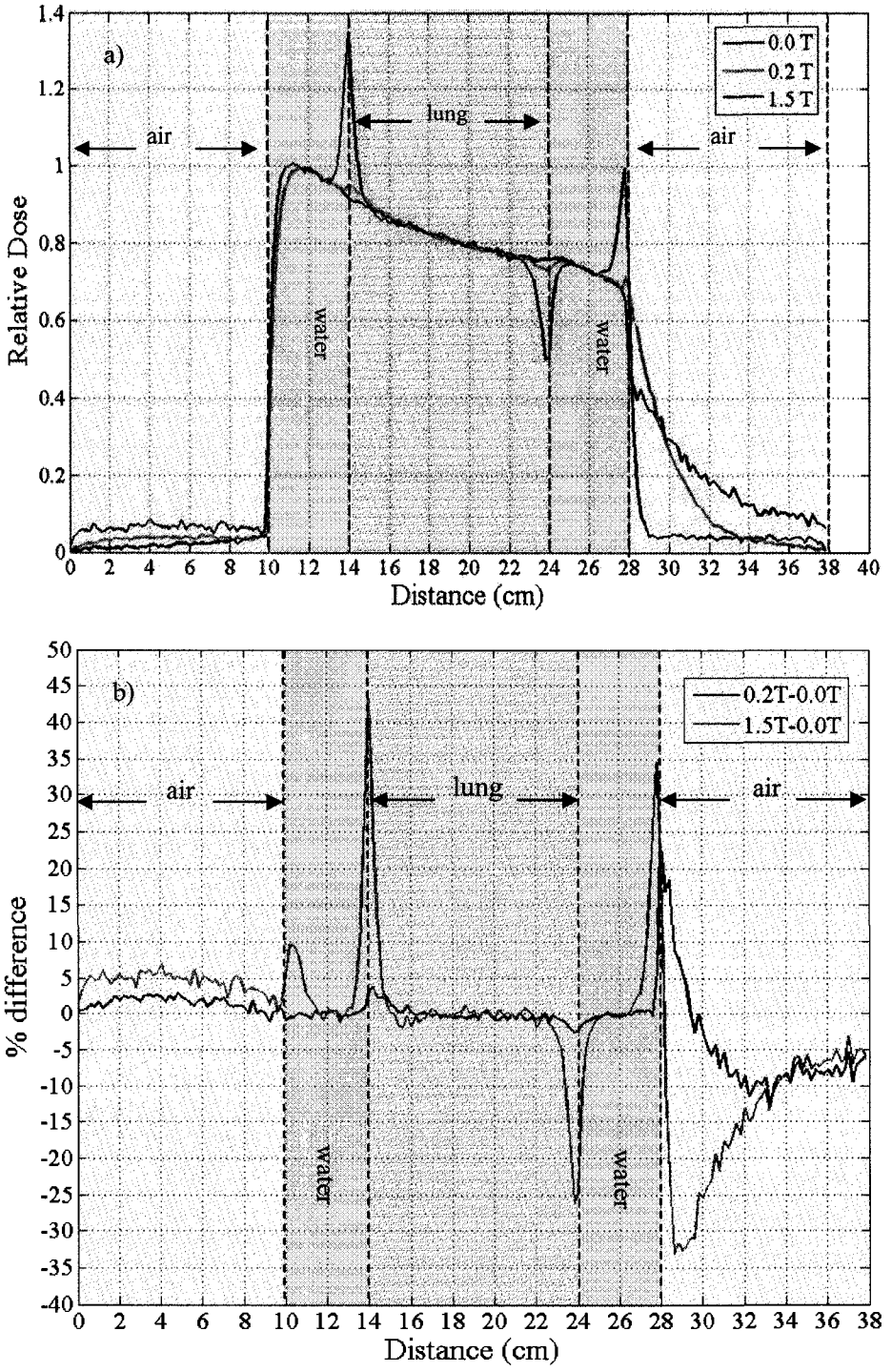

Figure 4.12. Central axis profiles: (a) comparison of the 0 T, 0.2 T and 1.5 T cases for a single beam; (b) $D_{0.2T} - D_{0.0T}$ and $D_{1.5T} - D_{0.0T}$ dose differences.

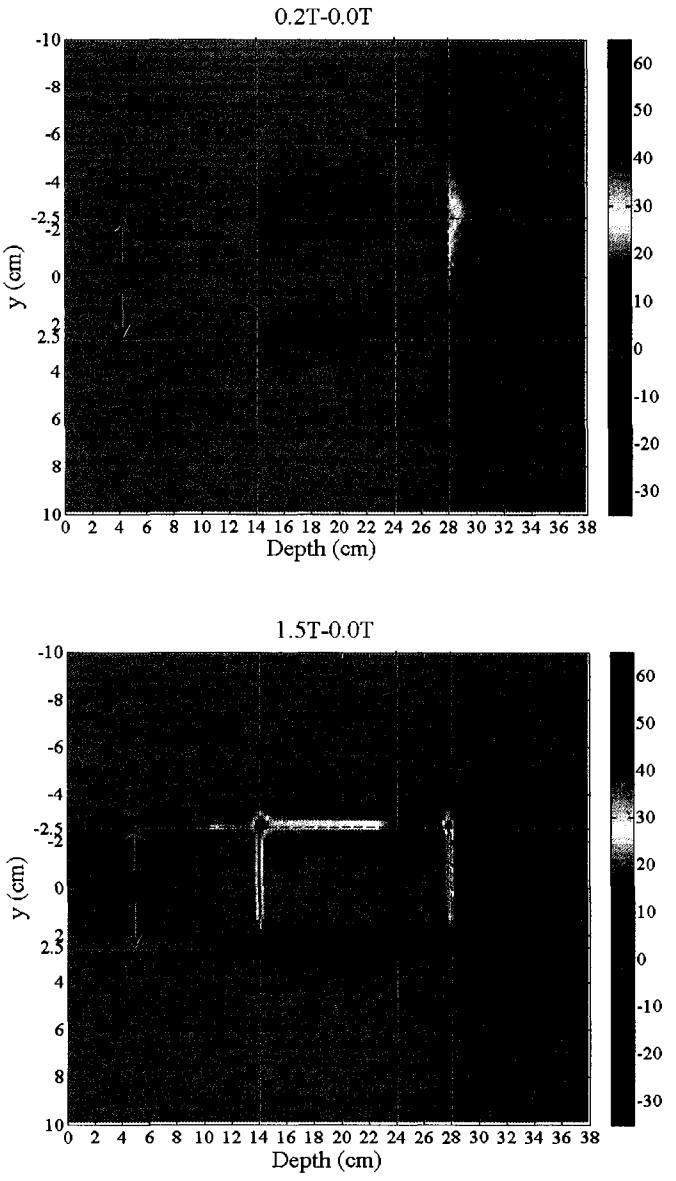

Figure 4.13. Dose difference maps (a) $D_{0.2\,T} - D_{0.0\,T}$ and (b) $D_{1.5\,T} - D_{0.0\,T}$ for a single field, for a 6 MV beam incident on a water-lung-water phantom.

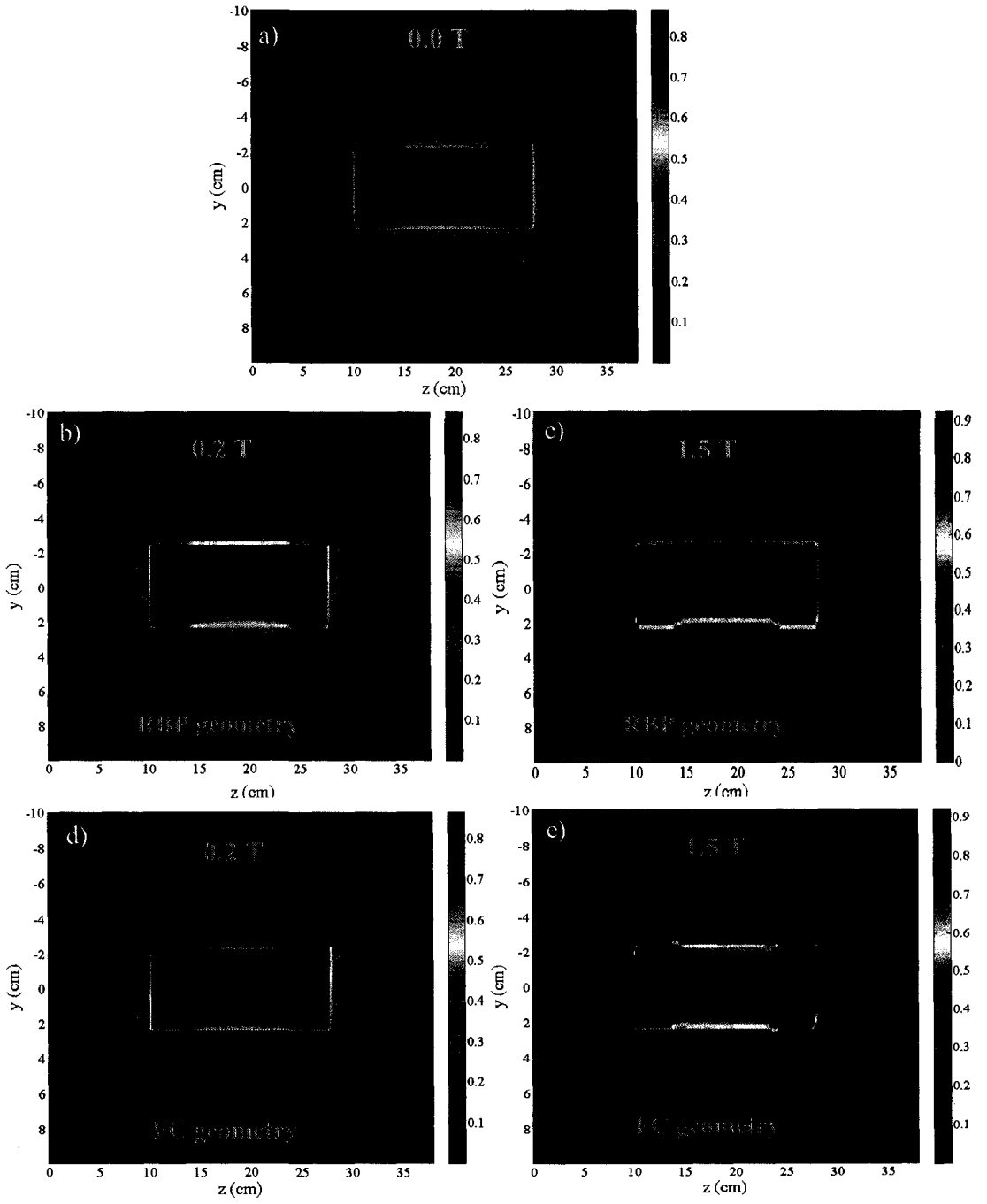

Figure 4.14. Cumulative relative dose distribution from two parallel opposing fields – (a) 0 T, (b) 0.2 T for RBP geometry, (c) 1.5 T for RBP geometry, (d) 0.2 T and FC geometry, (e) 1.5 T and FC geometry. change axis to % - see also following images

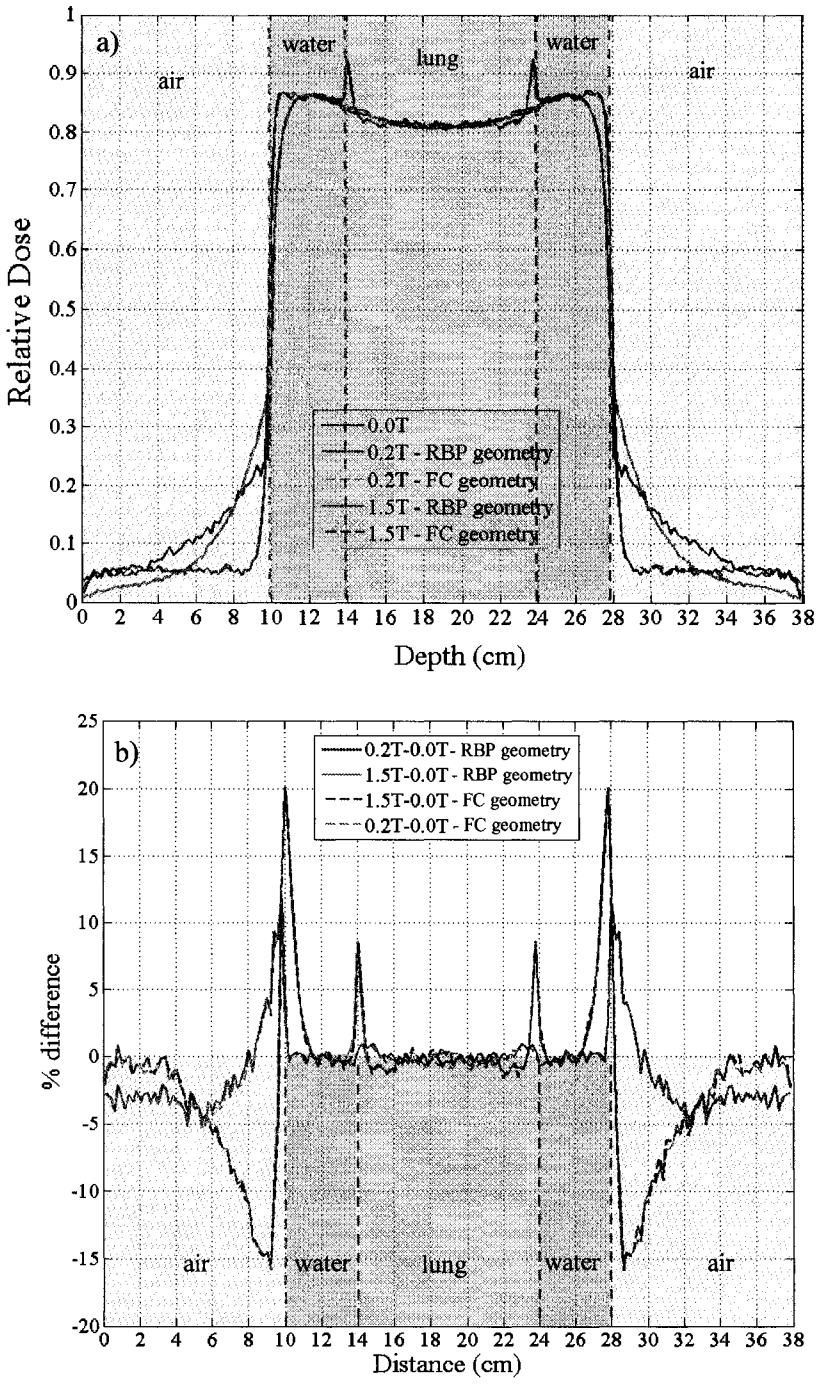

Figure 4.15. Parallel opposing fields: (a) central axis 0.2 T and 1.5 T profiles corresponding to both RBP and FC system configurations; (b) $D_{0.2T} - D_{0.0T}$ and $D_{1.5T} - D_{0.0T}$ dose differences.

4.2.3 Discussion

The net effect induced by the presence of the external magnetic field in either RBP or FC geometry is to generate a dose distribution shift in the direction of the Lorentz force. Sufficiently strong magnetic fields can produce significant electron return effects especially when radiation beam enters a low density material. Ideally, these dosimetric effects would be accounted for in the treatment planning algorithms used for clinical applications. However, it is hard to predict the consequences of the return effects due to high magnetic fields (e.g. 1.5 T) in practical complex geometries without Monte Carlo calculations. In contrast, for low magnetic fields (e.g. 0.2 T) the dose distributions are not significantly altered suggesting that simple corrections could be implemented by slightly shifting the dose distributions along the direction of the Lorentz force. In our particular case of a 0.2 T RBP geometry such a correction could be defined as dose shifts related to the density of the targeted material, e.g. lung. However, this is an area that requires further investigations.

Previously, studies[1-4] were performed to investigate the dose effects in the presence of an 1.5 T field. In particular, the 1.5 T relative dose profile shift towards the air-to-water interface in the case of a water slab phantom (see Fig. 4.5) was also determined by Raaymakers *at al*[1] by performing Monte Carlo calculations (using GEANT4 toolkit[33, 34]) and measured experimentally by Raaijmakers *et al*[3]. The authors reported on a 3 mm shift which is in very good agreement with our results (i.e. 3-4 mm).

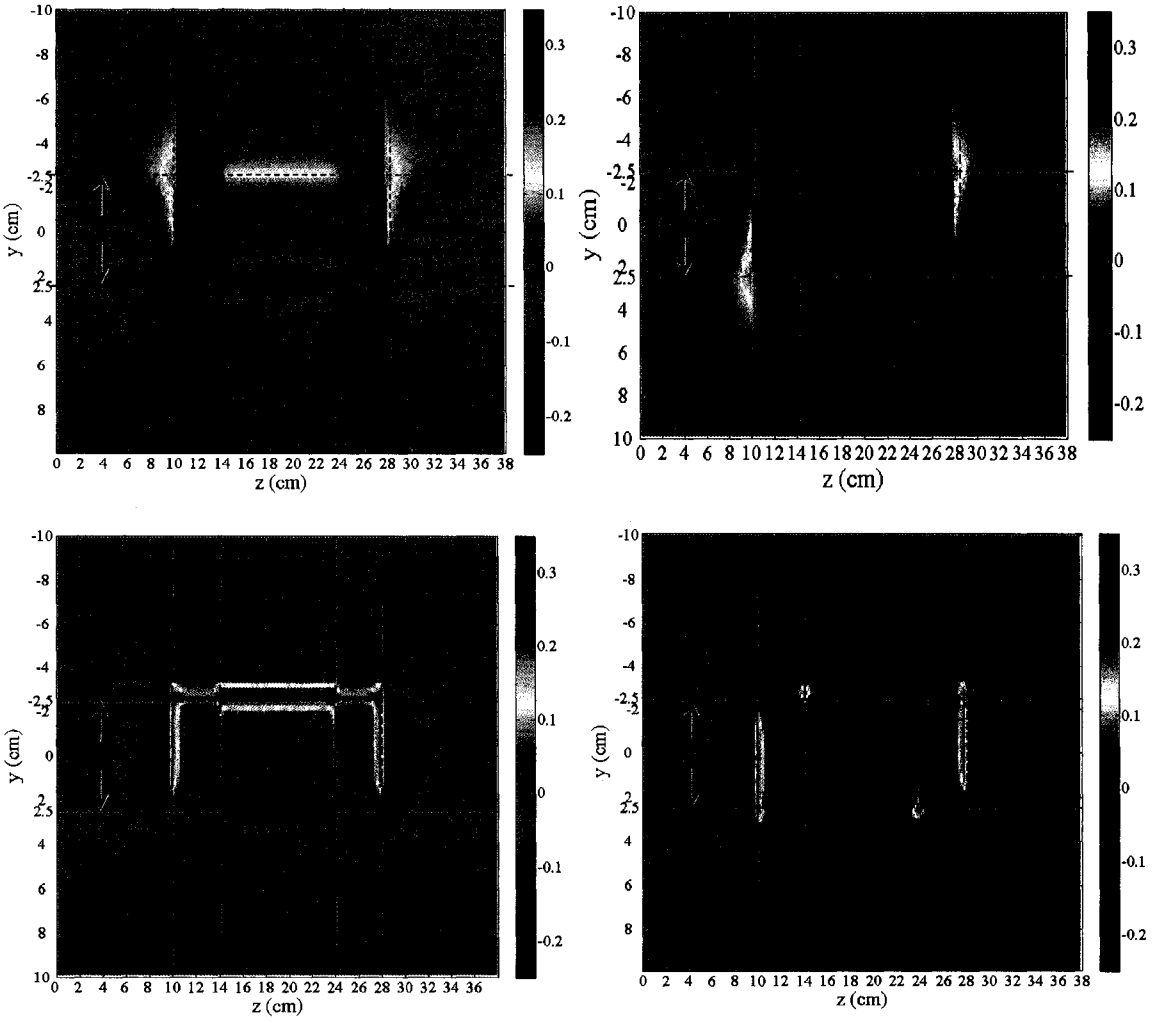

Figure 4.16. Cumulative parallel opposing fields' dose difference distributions with respect to the 0 T case for (a) 0.2 T and RBP geometry, (b) 0.2 T and FC geometry, (d) 1.5 T and RBP geometry, (e) 1.5 T and FC geometry.

4.2.4 Conclusions

We analyzed the dosimetric consequences caused by an external magnetic field in semi-infinite slab phantoms (combination of water, lung and air materials). The analysis was performed for low (0.2 T) as well as high (1.5 T) magnetic fields by considering two inherently different MRI-Linac system configurations, i.e. RBP and FC. The RBP geometry assumes a therapy Linac coupled rigidly to an open end of a bi-planar 0.2 T MRI permanent magnet. Both components rotate axially around the patient to deliver radiation at any desired angle. The FC arrangement is comprised of a fixed solenoid integrated with a rotating radiation source (FC). The simulations were aimed to help the understanding of the dose distribution patterns produced by a novel MRI-Linac system (RBP configuration), which is under investigation in our institution.

Substantially different dose patterns are generated for the RBP and FC configurations due to different relative orientations of $\vec{B}_0$ and the radiation beam with regard to the phantom. For our proposed configuration (i.e. 0.2 T field and RBP geometry) the maximum dose difference with regard to the no field case was found to be less than 5 % and 6 % for a single and two parallel opposing fields, respectively, in a water phantom. The magnitudes of these effects double in the case of a water-lung-water phantom.

4.3 MAGNETIC SHIELDING CONSIDERATIONS FOR AN MRI-LINAC SYSTEM

One of the main technical difficulties involved in the construction and operation of an MRI-Linac system is related to the magnetic interference between the MRI magnet and the therapy linear accelerator. For a typical linac, electrons are emitted by the linac's gun and are quickly accelerated inside the waveguide until they reach the target. As a result of the electrons' interaction processes within the linac's target, x-rays are produced and subsequently used for therapy purposes. The presence of a sufficiently strong external magnetic field may undesirably alter the trajectories of the traveling electrons inside the waveguide leading to an improper operation of the Linac. Thus the Linac needs to be shielded against the magnet's fringe fields below a level, i.e. 0.5 G representing the earth's magnetic field strength, which would not noticeably perturb the electrons' trajectories.

The magnetic shielding can be (a) passive by using strategically designed and placed pieces of metallic materials whose purpose is to deflect the magnetic field away from the spatial regions of interest or (b) active by implementing special coil configurations to cancel out the magnet's fringe fields at the desired locations. In this section, we investigate a passive shielding method for an MRI-Linac system based on a bi-planar magnet.[5, 10, 14, 15] We chose to use passive shielding as it was easy to design and simulate.

4.3.1 Materials and methods

4.3.1.1 System description

The schematic of the MRI-Linac configuration which is under investigation in our institution is depicted in Fig. 4.17a. The system comprises of a bi-planar 0.2 T permanent magnet, a typical 6 MV therapy accelerator along with a multi-leaf collimator (MLC) and a beam stopper. The Linac is coupled rigidly to one of the open ends of the magnet, thus the treatment beam can be delivered unobstructed to the active treatment volume, i.e. 40 x 40 x 40 cm^3 region centered at the isocenter of the MRI unit. The size of this volume was chosen to meet the treatment requirements of most of the patients. The bremsstrahlung target of the Linac is located at 1.95 m away from the isocenter of the magnet. The MLC is an add-on device of the medical Linacs that allows the implementation of advanced radiation treatment techniques such as IMRT. The beam stopper has the role of absorbing the exit radiation from the treatment region. The imaged sample remains stationary in the horizontal plane while the MRI unit and the Linac revolve in unison around it. The magnet structure is characterized by a height of 1.97 m and a square footprint with a side of 2.12 m (Fig. 4.17a). The magnet poles are embedded in a steel (1020) structure supported by four posts. A 3D representation of the magnet is shown in Fig. 4.17b. The opening of the magnet is 83 cm. It is common practice to attach annular-shaped materials, i.e. Rose rings, to the parallel inner faces of the magnet frame holding the poles (Fig. 4.17a) to enhance the homogeneity of the magnetic field inside the active volume. Considering that each ring is 5.5 cm high, the magnet opening is reduced to 72 cm.

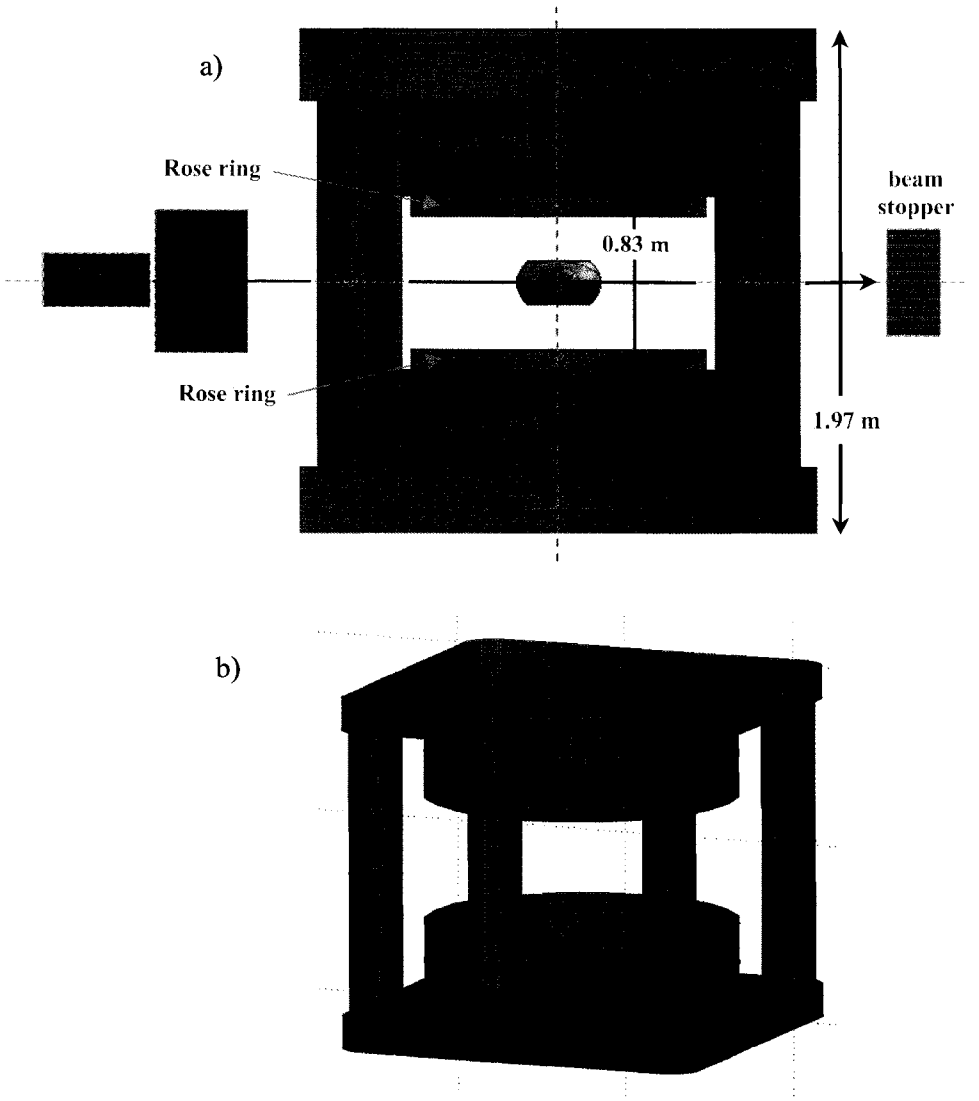

Figure 4.17. Schematic representation of the human integrated MRI-Linac system: (a) dimensions of the magnet structure and the main components of the system, i.e. magnet, Linac, MLC, and beam stopper; (b) 3D view of the magnet.

4.3.1.2 Numerical simulations

The magnetic field of the human magnet was modeled by using the AC/DC module of COMSOL Multiphysics (version 3.3a, COMSOL, Stockholm, Sweden),[35] a commercially available software package. COMSOL is a powerful interactive environment for simulating a wide variety of scientific and engineering partial differential equations (PDEs)-based problems by using finite element method (FEM) analysis. COMSOL allows the user to define any desired problem by feeding custom PDEs or by selecting and modifying pre-defined physics application templates, i.e. specialized modules consisting of equations and variables for specific areas of interest. The modules available in COMSOL version 3.3a include: AC/DC and RF dealing with electromagnetism problems, Acoustics, Chemical Engineering, etc. These modules are designed to interact with each other to allow the simulation of complex multi-physics problems. The user can access COMSOL by using either a standalone Java-based graphical user interface (GUI) or scripting macros written in Matlab or the COMSOL Script language.

The AC/DC module, as an additional package for COMSOL, provides a library of functional models for the analysis of electromagnetic effects, components, and systems (e.g. electric motors, generators, permanent magnets, etc). For our particular problem of a bi-polar magnet we used a 3D model that is based on the magnetostatics of magnetic materials with no electric currents present. In this model, the fundamental equations are represented in terms of the magnetic scalar potential, i.e. V_m. A current free region is characterized by

$$\vec{\nabla} \times \vec{H} = 0 \tag{4.1}$$

where $\vec{\nabla} = \vec{i}\frac{\partial}{\partial x} + \vec{j}\frac{\partial}{\partial y} + \vec{k}\frac{\partial}{\partial z}$ with $(\vec{i}, \vec{j}, \vec{k})$ being the unit vectors along the main axes (x,y,z).

The magnetic field $\vec{H}$ is defined as the gradient of V_m

$$\vec{H} = -\vec{\nabla} V_m \tag{4.2}$$

similarly to the definition of the electric potential for static electric fields. $\vec{H}$ is related to the magnetic field density, i.e. $\vec{B}$, as follows

$$\vec{B} = \mu(\vec{H} + \vec{M}) \tag{4.3}$$

where $\mu = \mu_r \mu_0$ is the magnetic permeability of the medium with μ_r and μ_0 being the relative medium and vacuum permeabilities, respectively, and $\vec{M}$ represents the magnetization vector of the medium. We can derive an equation for the magnetic potential V_m by considering Eq. (4.3) along with the Gauss law for magnetism given by

$$\vec{\nabla} \cdot \vec{B} = 0 . \tag{4.4}$$

which states that the magnetic field has no divergence, i.e. the magnetic field lines are solenoidal. Substituting Eqs. (4.2) and (4.3) in Eq. (4.4) we obtain

$$-\vec{\nabla} \cdot (\mu \vec{\nabla} V_m - \mu \vec{M}) = 0 . \tag{4.5}$$

In Eq. (4.5), considering that the values of μ and M are known for all materials involved in the magnet geometry we can determine V_m at any location in space. Once V_m is calculated, H and B can be derived from Eqs. (4.2) and (4.3), respectively.

Considering the complexity of our system geometry (i.e. magnet, linac with MLC and additional shielding material) it is impractical to analytically solve the PDEs involved in Eq. (4.5). Therefore, numerical methods such as FEM need to be implied. The concept of FEM is to subdivide the problem geometry into a large number of non-overlapping regions, i.e. finite elements, characterized by a simple geometry (e.g. triangles). For each element, the exact solution of V_m is approximated by a simple function. For example, in the case of a triangle-shaped element the function can be defined as the linear interpolation of the V_m values corresponding to the triangle's three vertices. Given that the elements' size is small enough the approximation of V_m closely matches its exact solution. The system model's response is considered to be approximated by that of the discrete model, which is generated by assembling all the constituent elements.

The workflow of a typical COMSOL simulation process is described in Fig. 4.18. The steps involved in the procedure are as follows

a) Define system geometry - The geometric arrangement of the system components and the associated media can be introduced to the simulation package by drawing each individual component of the system using the 2D/3D drawing tools available in COMSOL or by importing the structure from dedicated design software such as AutoCAD or SolidWorks. The 3D simulation geometry is comprised of the magnet structure described in Section 4.3.1.1 (see also Fig. 4.17) confined in an air-filled cube with an 8 m side, i.e. world box. The geometry is depicted in Fig. 4.19. The world box is required to define the space for which the domain equations are solved and so minimize the computation time. However, its dimensions were chosen to be large enough to allow an accurate representation of the fringe field around the magnet. Additional components were placed in the vicinity of the magnet for shielding purposes, i.e. a pair of steel plates and a metal box surrounding the Linac and MLC (see below);

b) Physics settings - By choosing to use the magnetostatics model with no currents from the AC/DC package, the physics equations are pre-defined (see Eq. (4.5)). The main boundary condition (BC) required to solve the system was along the exterior boundaries of the world box. Specifically, the magnetic field was assumed to be tangential to the box's walls to resemble the closed loop characteristic of the field lines. This condition translates into the following BC

$$\vec{n} \cdot (\mu \nabla V_m - \mu \vec{M}) = \vec{n} \cdot \vec{B} = 0 \tag{4.6}$$

where $\vec{n}$ is the normal vector to the boundaries. Figure 4.20 shows the distribution of several magnetic field lines and their behaviour in the close vicinity of the world box's boundaries as imposed by Eq. (4.6). The relative permeabilities of the main components such as the magnet structure were introduced as parameters by considering the magnetic

properties of the corresponding materials, i.e. the relative permeability curves as a function of the magnetic field strength. An example of such a curve is shown in Fig. 4.21 for steel 1020 (data provided by NRC) which was used for the magnet structure (see Fig. 4.17);

c) Mesh generation – Adequate discrete mesh size is automatically/manually selected for each individual component as a function of its dimensions and the desired degree of local resolution (see Figure 4.22). Several mesh parameters, e.g. curvature mesh size and curvature resolution cutoff, are used to determine the local mesh size.

d) Compute solution – the solver and its parameters are chosen along with the solution parameters. We used the FGMRES solver with an algebraic multigrid (AMG) preconditioner, which was designed to optimize the solver for maximum performance with significant reduction in memory usage when applied to large 3D models. The main solver parameters were: i) relative tolerance (10^{-6}) which is defined as the threshold difference between two consecutive iterations required for the solver to converge and ii) maximum number of iterations (5000).

e) Data post-processing - The solution is visualized and verified using COMSOL. For further data analysis, e.g. generation of 2D parts per million (ppm) local field variation maps, the simulation models were exported as scripting code and integrated into an in-house developed data processing software written in Matlab. The 2D ppm maps were required to evaluate the effects on the field homogeneity across the magnet's imaging volume caused by the placement of additional components in the vicinity of the magnet's structure (e.g. shielding plates, linac, etc). The 2D ppm distributions were determined by using

$$ppm = 10^6 \frac{B_{struct} - B_{init}}{0.2} \tag{4.7}$$

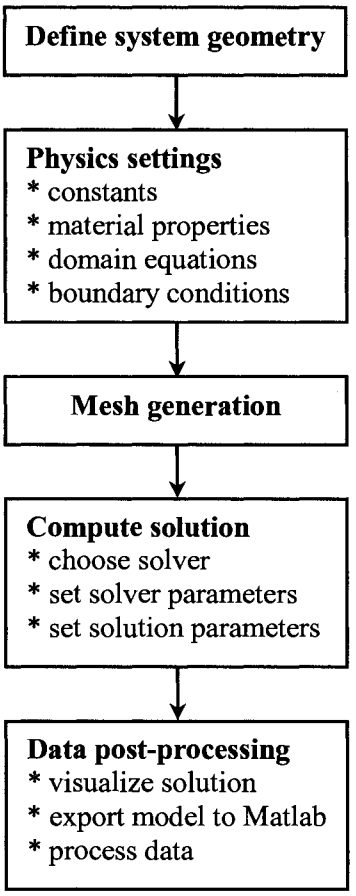

Figure 4.18. Diagram showing the main steps of a typical COMSOL simulation process.

where B_{init} and B_{struct} represent the 2D distributions of the magnetic field corresponding to the magnet (reference map) and the magnet along with new component, respectively, calculated in COMSOL.

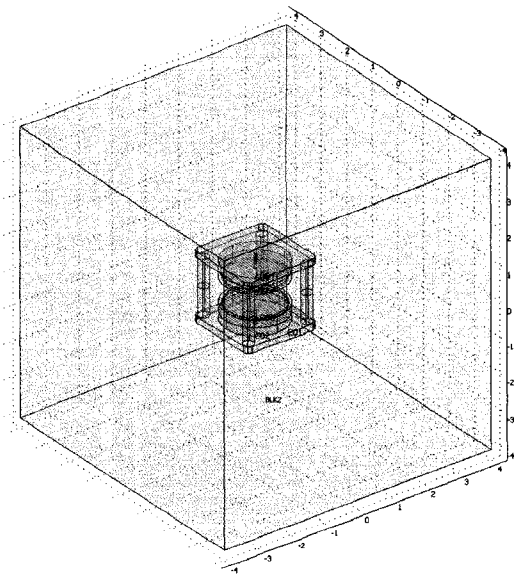

Figure 4.19. Schematic of the model geometry consisting of the world box along with the magnet structure.

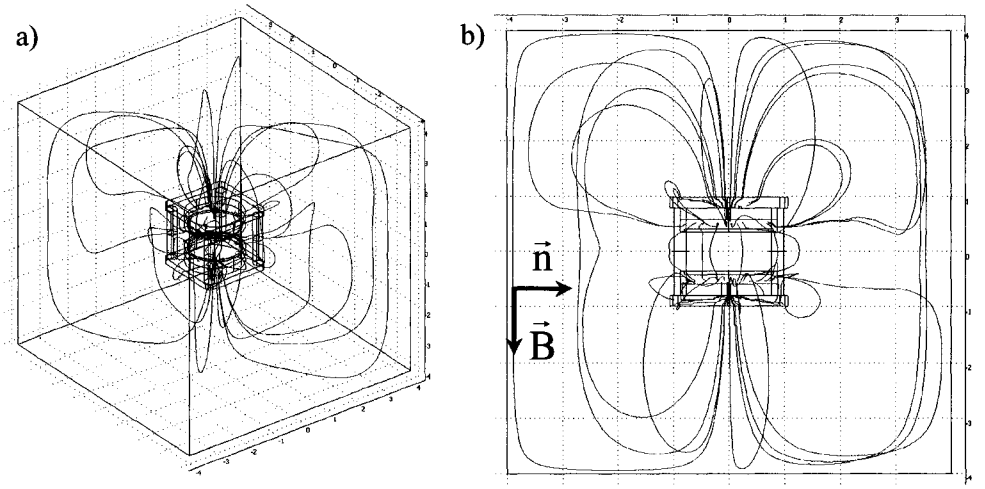

Figure 4.20. The boundary condition set along the world box's boundaries considers that only the parallel component of the magnetic field is non-zero: a) 3D representation of several magnetic field lines, b) 2D section of the geometry showing the orientation of the normal and magnetic field vectors at one boundary of the world box.

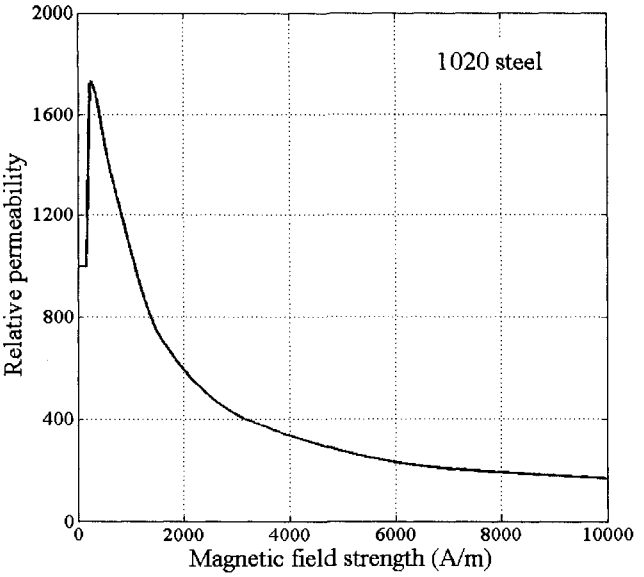

Figure 4.21. The relative permeability of steel (1020) as a function of the magnetic field strength. The maximum field strength used in our simulations was about 50000 A/m.

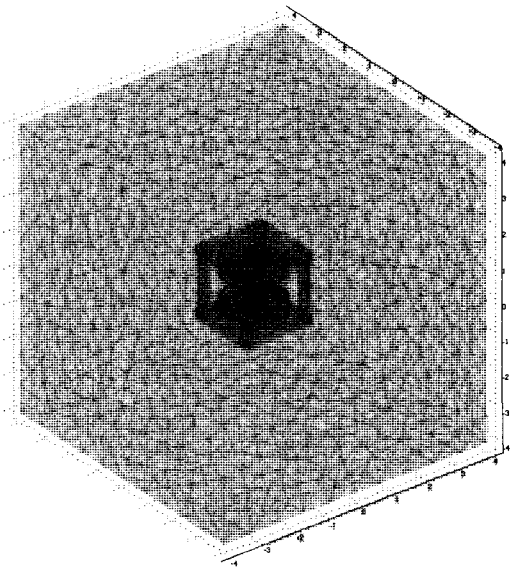

Figure 4.22. A typical representation of the meshing process applied to our geometry (see Fig. 4.20). The local mesh size is dependant on the dimensions of each sub-domain.

4.3.2 Results and discussion

Figure 4.23 shows the magnet's field distribution corresponding to the transverse and horizontal radiation beam central axis planes. Figure 4.24 shows the central axis profile of the magnetic field strength as a function of distance from the isocenter of the magnet along the radiation beam direction. As expected, the field stays constant inside the magnet and decreases as we move away from the structure. In the vicinity of the Linac, at about 2 m away from the isocenter of the magnet, the field is approximately 40 G (see inset in Fig. 4.24). Considering this field level and the fact that the electrons are emitted by the Linac gun with an energy of 30 KeV, the radius of the traveling electrons' path is about 8.5 cm. By accelerating the electrons in the Linac's waveguide the perturbation due to the external fringe field becomes less significant. However, at the target the electrons may show a significant shift from their correct trajectory corresponding to the case of no external field. In the MLC region, the field is significantly higher, ranging from 40 to 325 G.

Figure 4.23 presents a limited picture of the magnetic field's behaviour in the Linac-MLC region as the metal components of both Linac and MLC, which could introduce a significant degree of distortion in the local fringe field, were not considered. To simplify the problem, we set the objective of our shielding simulations to be the reduction of the fringe field in the Linac-MLC area below the earth's magnetic field (i.e. 0.5 G). The main reason for choosing such a criterion is that a typical therapy accelerator is designed to properly operate at this field level. In addition, the effects induced by a high magnetic field on the MLC's components may be difficult to calculate. Considering that the fringe field in the Linac-MLC region exceeds the 0.5 G criterion, both the Linac and MLC need to be shielded.

The passive shielding was implemented by adding steel (1020) plates on two opposite sides of the magnet as shown in Fig. 4.25. By choosing two identical plates, we ensure that the field inside and outside the magnet is symmetrically altered. The size of each plate was chosen to

cover the entire side of the magnet structure, i.e. 1.97 m high and 2.12 m wide. The thickness and location of the plates were varied to determine the best shielding configuration.

Figure 4.26 shows the fringe field central axis profiles along the radiation beam direction at the location of the Linac and MLC for several values of the plates' thickness. The plates were symmetrically placed on each side of the magnet at a distance of 10 cm. By increasing the plates' thickness the field intensity decreases in the first half of the MLC region due to a folding effect of the field lines in the region prior to the MLC. All profiles reach a minimum of about 0.05 G. In the second half of the MLC area, the field values increase up to about 1.4 G. The folding effect is a direct consequence of placing the shielding plates in the vicinity of the magnet as they perturb the fringe field at the MLC-Linac location (see no-plates case in Fig. 4.24). In contrast, in the Linac area the field stays almost constant at about 1.5 G.

The presence of the steel plates perturbs the homogeneity of the field inside the magnet, i.e. 40 x 40 x 40 cm^3 treatment volume. To avoid interference with the MR imaging procedures it is desired that the field inhomogeneities are minimal. Figure 4.27 shows that by increasing the plates' thickness from 5 cm to 10 cm the maximum ppm variation inside the magnet drops from 300 to about 240 ppm. Increasing the plates' thickness further, from 10 cm to 15 cm, does not result in further improvement of inhomogeneities.

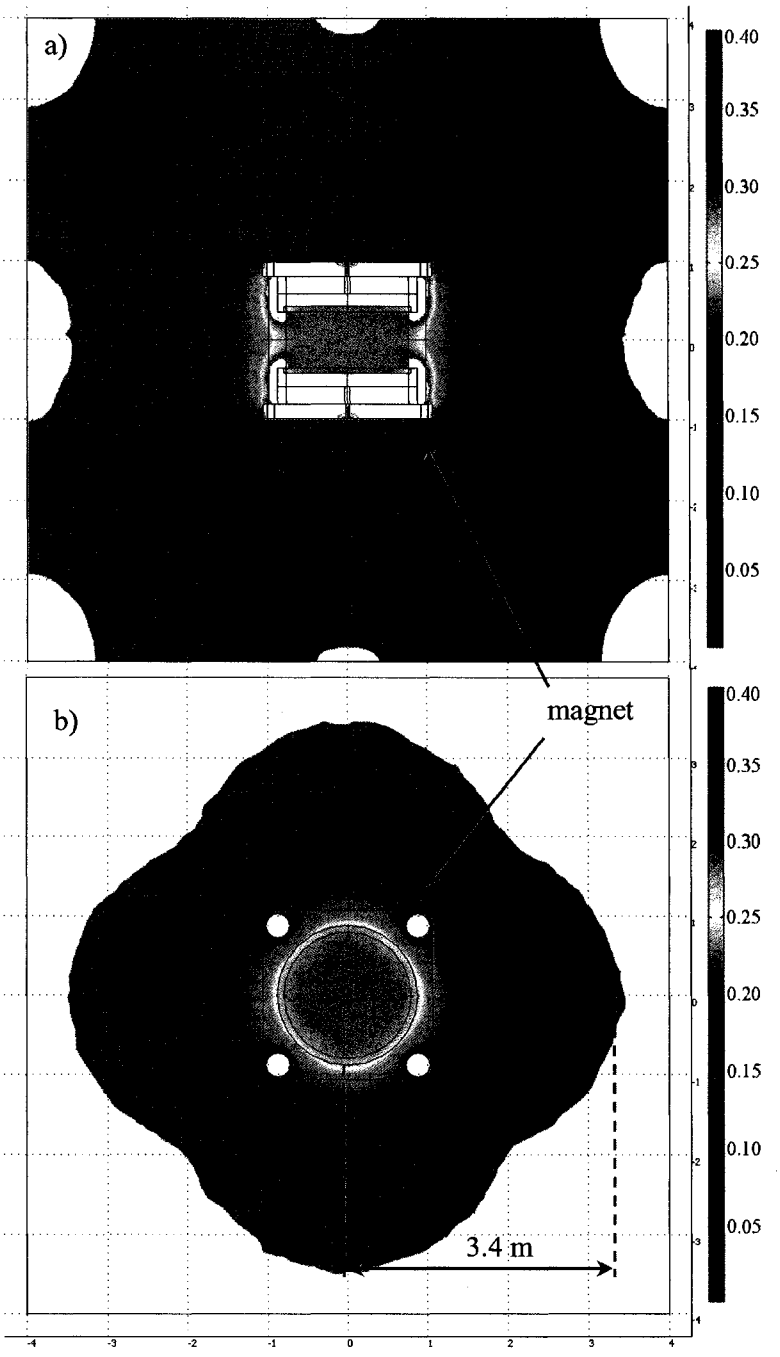

Figure 4.23. 2D maps showing the 0.5 G field distribution inside the world box (8 m side) for the radiation beam central axis: a) transverse and b) horizontal planes. The grid spacing is 1 m. The color code scale (blue to red) is from 0.5 G to $4 \cdot 10^3$ G (or 0.4 T). The white regions are characterized by field strengths outside the scale (both sides).

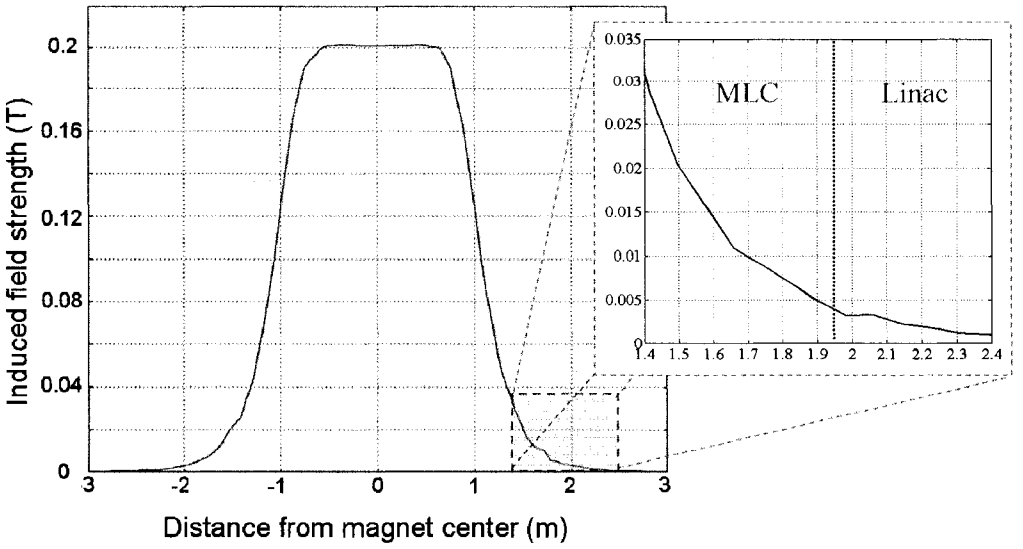

Figure 4.24. Radiation beam central axis magnetic field profile as a function of distance from the magnet's isocenter. A zoom into the region corresponding to the Linac and MLC is shown in the inset.

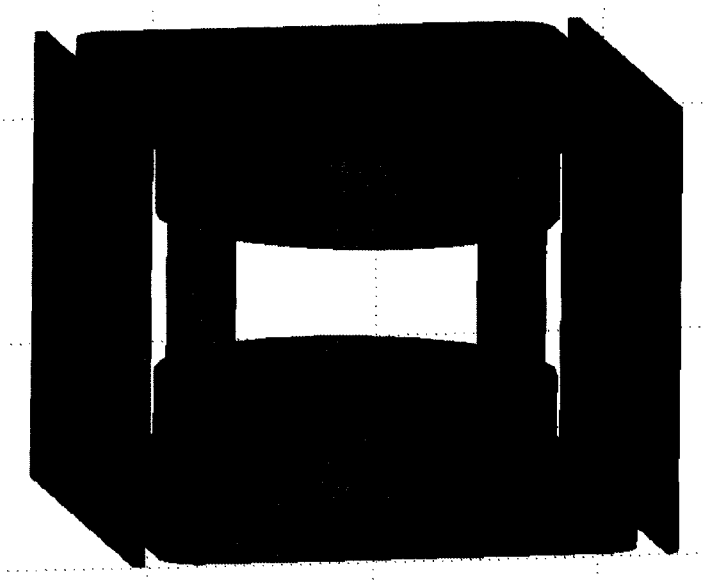

Figure 4.25. Passive shielding applied to the magnet by adding steel (1020) plates on 2 opposite sides of the magnet. The plate facing the Linac has a window that allows the unobstructed passing of the therapy beam. The size of the window was chosen to allow a 40 x 40 cm^2 field size at the isocenter of the magnet.

Figure 4.28 depicts the central axis profiles of the magnetic field in the Linac-MLC area for several values of the plates-to-magnet distance. The plates' thickness was 5 cm. In the MLC region, right behind the shielding plates, the field increases with the increase of the plates-to-magnet distance. In the second half of the MLC area, i.e. after the folding effect region, the trend is reversed, specifically the field decreases with the increase of the plates-to-magnet spacing. In the Linac region, the field follows a similar trend, i.e. it decreases with the increase of the plates-to-magnet distance. The effects on the field homogeneity inside the magnet induced by placing the plates at different locations are shown in Fig. 4.29. By increasing the plates-to-magnet distance from 1 cm to 20 cm, the maximum field variation decreases from about 650 ppm to 135 ppm. Considering the data presented in Figs. 4.26-4.29, we choose to use for our shielding configuration 10 cm thick steel plates positioned at 10 cm away from the magnet structure. This results in a fringe field of less than 3 G in the Linac-MLC region. Inside the magnet, the field variation is within 300 ppm. Such a level of inhomogeneity can be corrected by using common active shimming techniques.

To reduce the fringe field in the Linac and MLC region below 0.5 G we surrounded these structures with a rectangular box with a 1 mm thick MuMetal™ wall as shown in Fig. 4.30. MuMetal™ is characterized by a very large relative permeability as shown in Fig. 4.31.[36] Due to this unique property, MuMetal™ is the material of choice for magnetic shielding purposes. However, MuMetal™ is very expensive, which required us to limit its use in the shielding design. Figure 4.32 shows that the field inside the MuMetal™ box is significantly lower that the 0.5 G tolerated level.

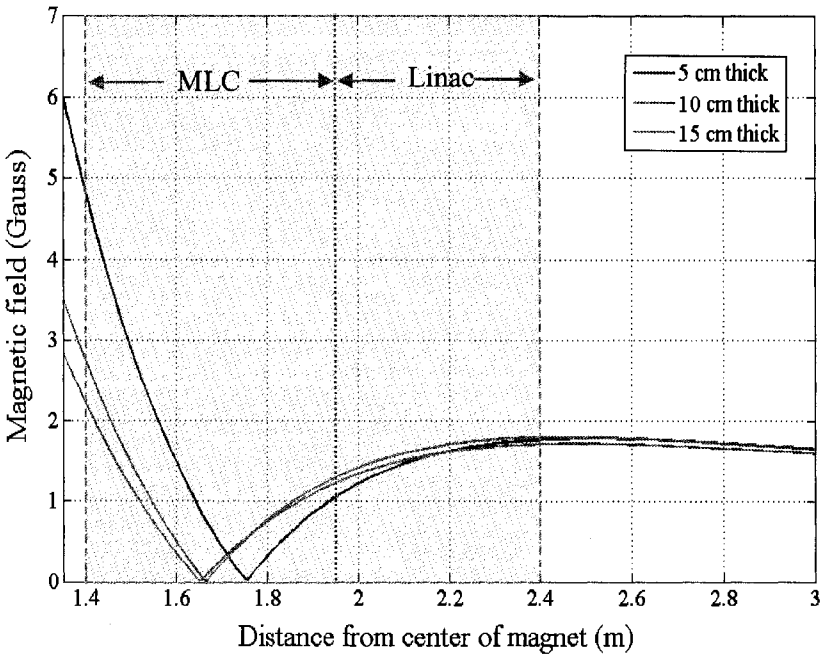

Figure 4.26. Central axis profiles of the magnetic field in the vicinity of the MLC and Linac as a function of the plates' thickness. The plates were placed at a distance of 10 cm away from magnet's structure.

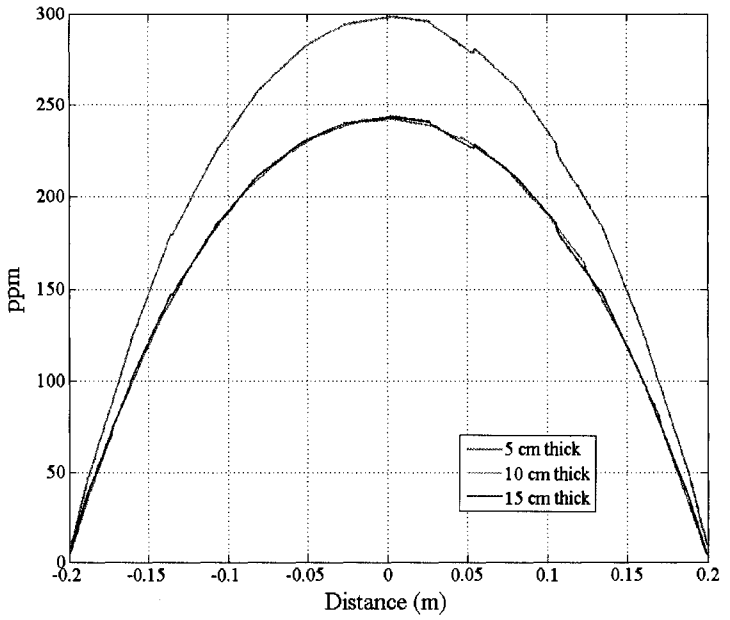

Figure 4.27. Central axis profiles of the magnetic field ppm local variation inside the magnet as a function of the plates' thickness. The plates were located at 10 cm away from the magnet structure.

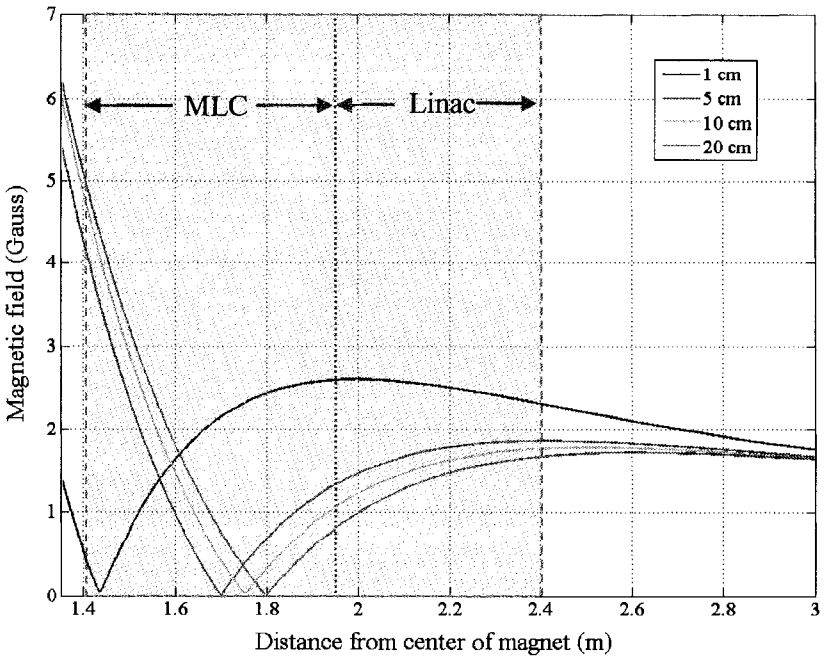

Figure 4.28. Central axis profiles of the magnetic field in the vicinity of the MLC and Linac as a function of plates' location. The plate thickness was 5 cm.

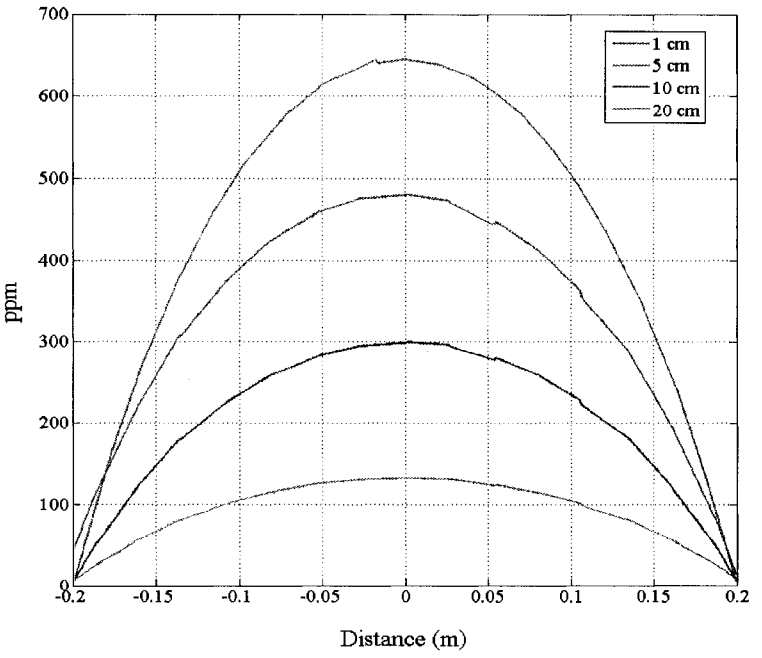

Figure 4.29. Central axis profiles of the magnetic field ppm local variation inside the magnet as a function of plates' location. The plate thickness was 5 cm.

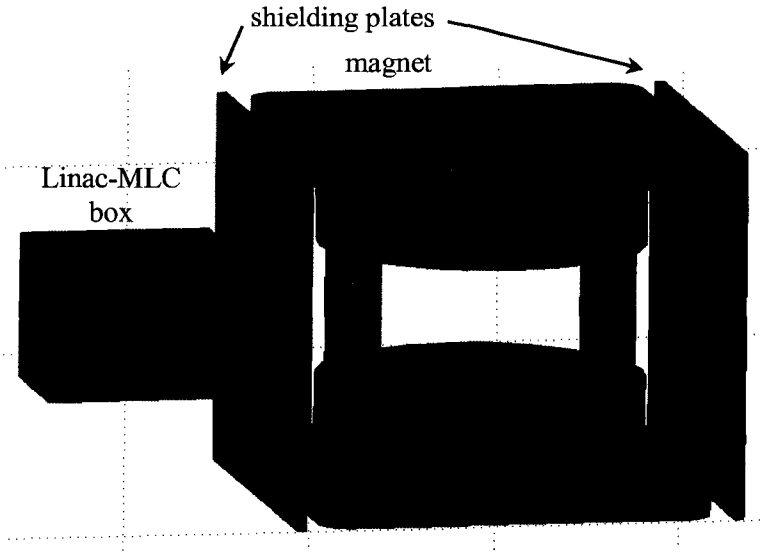

Figure 4.30. The MRI-Linac system configuration consisting of the magnet structure and 2 steel (1020) plates along with a MuMetal™ box required for the shielding of the Linac and MLC components from magnet's fringe fields.

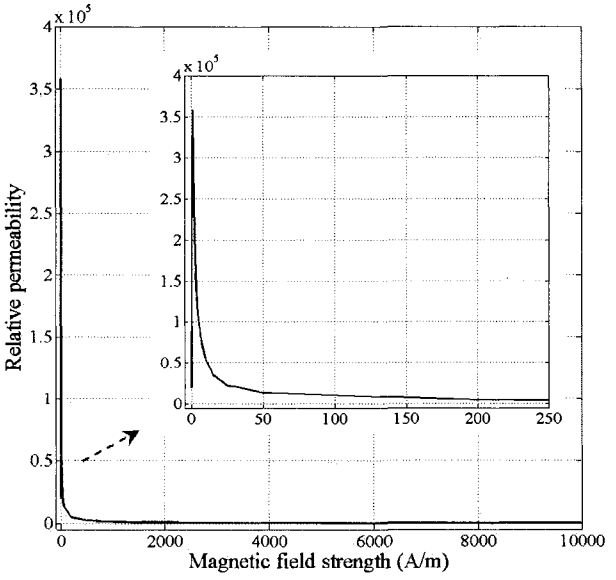

Figure 4.31. The relative permeability of MuMetal™ as a function of the magnetic field strength. The inset shows a zoomed image of the relative permeability at low field strengths.

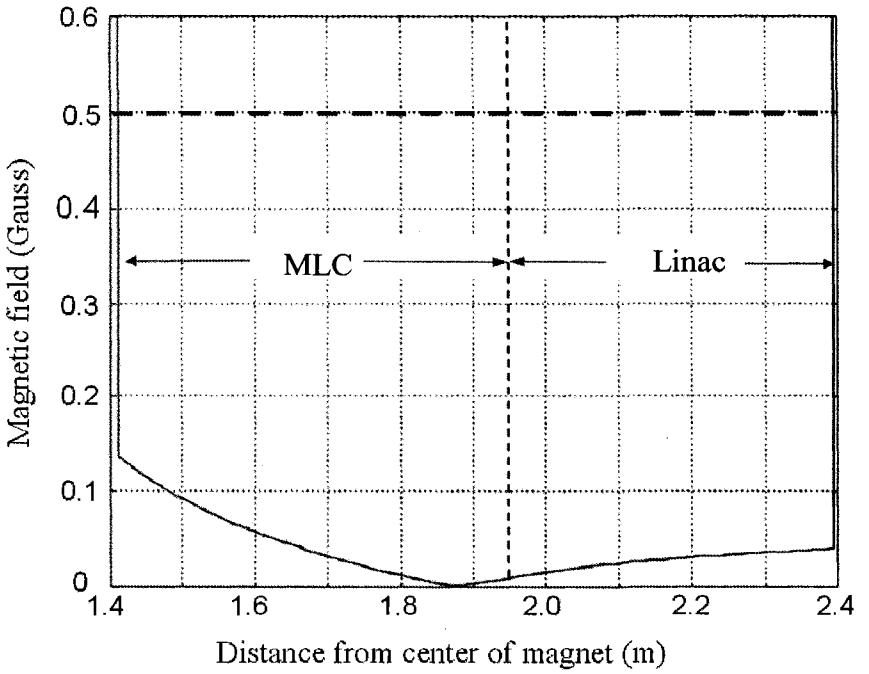

Figure 4.32. Central axis profile of the magnetic field inside the MuMetal™ Linac-MLC box. The field is significantly lower than the design level given by the red dashed line, i.e. 0.5 G.

4.3.3 Conclusions

We investigated a passive shielding method applied to an MRI-Linac system based on a 0.2 T bi-planar magnet. The magnet was simulated using COMSOL, a commercially available software tool for solving partial differential equations based on the finite element method.

The passive shielding was introduced and optimized to minimize the magnetic interference between the magnet and the Linac. The magnet's fringe field strength in the space occupied by the Linac and MLC was reduced below earth's magnetic field, i.e. 0.5 G. This was achieved: (a) by placing steel (1020) plates on two opposite sides of the magnet structure and (b) by surrounding the Linac and MLC with a rectangular box lined with a 1 mm thick MuMetal™ wall. Once magnetically shielded, the Linac can operate normally when coupled to the 0.2 T MRI system.

4.4 REFERENCES

1. Raaymakers BW, Raaijmakers AJ, Kotte AN, *et al.* Integrating a MRI scanner with a 6 MV radiotherapy accelerator: dose deposition in a transverse magnetic field. *Phys Med Biol* 2004;49:4109-4118.
2. Raaijmakers AJ, Raaymakers BW, Lagendijk JJ. Integrating a MRI scanner with a 6 MV radiotherapy accelerator: dose increase at tissue-air interfaces in a lateral magnetic field due to returning electrons. *Phys Med Biol* 2005;50:1363-1376.
3. Raaijmakers AJ, Raaymakers BW, Lagendijk JJ. Experimental verification of magnetic field dose effects for the MRI-accelerator. *Phys Med Biol* 2007;52:4283-4291.
4. Raaijmakers AJ, Raaymakers BW, van der Meer S, *et al.* Integrating a MRI scanner with a 6 MV radiotherapy accelerator: impact of the surface orientation on the entrance and exit dose due to the transverse magnetic field. *Phys Med Biol* 2007;52:929-939.
5. Fallone B, Carlone M, Murray B, Rathee S, Stanescu T, Steciw S, Wachowicz K, Kirkby C. Development of a Linac-MRI System for Real-Time ART. [Abstract]. *Med Phys* 2007;34:2547.
6. Lagendijk J, Raaymakers BW, van der Heide U, Overweg J, Brown K et al. In Room Magnetic Resonance Imaging Guided Radiotherapy (MRIgRT). *Med Phys* 2005;32:2067
7. Dempsey J, Benoit D, Fitzsimmons JR, Haghighat A, Li JG et al. A Device for Realtime 3D Image-Guided IMRT. 2005;47th Annual ASTRO General Meeting, Denver, CO.
8. Yanez Y, Dempsey JF. Monte Carlo Simulations of Air Cavities in Phantoms Submerged in Magnetic Fields. *Med Phys* 2007;34:2590
9. Kron T, Eyles D, Schreiner JL, Battista J. Magnetic resonance imaging for adaptive cobalt tomotherapy: A proposal. *J Med Phys* 2006;31:242-254.

10. Fallone B, Carlone M, Murray B, Rathee S, Stanescu T, Steciw S, Kirkby C, Tomanek B, Sharp J. Development of a Small Bore Linac-MRI System for Real Time Image Guided Radiotherapy. [Abstract]. *Radiother Oncol* 2007;84:S3.

11. Fallone B, Carlone M, Murray B. Integrated External Beam Radiotherapy and MRI System. PCT International Patent. Vol WO/045076; 2007. pp. 5625-5635.

12. Fallone B, Carlone M, Murray B. Real-time Dose Reconstructed Using Dynamic Simulation and Image-Guided Adaptive Radiotherapy. PCT International Patent. Vol WO/045075; 2007. pp. 5625-5634.

13. Carlone M, Lamey M, Steciw S, Burke B, Fallone B. Study of RF Interference Between a Linear Accelerator and MRI. [Abstract]. *Med Phys* 2007;34:2621.

14. Steciw S, Stanescu T, Carlone M, Fallone B. Magnetic Shielding of a Coupled MRI-Linac System. [Abstract]. *Med Phys* 2007;34:2623.

15. Murray B, Fallone G, Carlone M, Steciw S, Stanescu T, Rathee S. Designing a Linac to Operate Near an MRI. [Abstract]. *Radiother Oncol* 2007;84:S3.

16. Kirkby C, Stanescu T, Rathee S, Carlone M, Murray B, Fallone BG. Patient dosimetry for hybrid MRI-radiotherapy systems. *Med Phys* 2008;(in press).

17. Bielajew AF. The effect of strong longitudinal magnetic fields on dose deposition from electron and photon beams. *Med Phys* 1993;20:1171-1179.

18. Jette D. Magnetic fields with photon beams: Monte Carlo calculations for a model magnetic field. *Med Phys* 2000;27:2726-2738.

19. Li XA, Reiffel L, Chu J, *et al.* Conformal photon-beam therapy with transverse magnetic fields: a Monte Carlo study. *Med Phys* 2001;28:127-133.

20. Reiffel L, Li A, Chu J, *et al.* Control of photon beam dose profiles by localized transverse magnetic fields. *Phys Med Biol* 2000;45:N177-182.

21. Sempau J. PENEASY, a structured main program for PENELOPE, freely available from http://www.upc.es/inte/downloads/penEasy.htm. 2006.

22. Salvat F, Fernández-Varea JM, Acosta E, *et al.* PENELOPE: A code system for Monte Carlo simulation of electron and photon transport. Issy-les-Moulineaux: OECD Nuclear Energy Agency; 2003.

23. Baro J, Sempau J, Fernandez-Varea JM, *et al.* PENELOPE: an algorithm for Monte Carlo simulation of the penetration and energy loss of electrons and positrons in matter. *Nucl. Instrm. Methods Phys. Res B* 1995;100:31-46.

24. Sempau J, Acosta E, Baro J, Fernández-Varea JM, Salvat F. An algorithm for Monte Carlo simulation of coupled electron-photon transport *Nucl. Instrm. Methods Phys. Res B* 1997;132:377-390.

25. Sempau J, Fernandez-Varea JM, Acosta E, Salvat F. Experimental benchmarks of the Monte Carlo code PENELOPE. *Nucl. Instrm. Methods Phys. Res B* 2003;207:107-123.

26. Chen Y, Bielajew AF, Litzenberg DW, Moran JM, Becchetti FD. Magnetic confinement of electron and photon radiotherapy dose: a Monte Carlo simulation with a nonuniform longitudinal magnetic field. *Med Phys* 2005;32:3810-3818.

27. www.rocksclusters.org.

28. www.centos.org.

29. www.open-mpi.org.

30. Sempau J. CLONEASY, a library of scripts, freely available from http://www.upc.edu/inte/en/descarregues.php (Barcelona, 2006).

31. Berger M, Coursey JS, Zucker DS. ESTAR, PSTAR, and ASTAR: Computer Programs for Calculating Stopping-Power and Range Tables for Electrons, Protons, and Helium Ions (version 1.2.2). [Online] Available: http://physics.nist.gov/Star 2005;(National Institute of Standards and Technology, Gaithersburg, MD, 2005).

32. Sheikh-Bagheri D, Rogers DW. Monte Carlo calculation of nine megavoltage photon beam spectra using the BEAM code. *Med Phys* 2002;29:391-402.

33. Agostinelli S, Allison J, Amako K, Apostolakis J, Araujo H *et al.* GEANT4 - a simulation toolkit. *Nuclear Instruments and Methods in Physics Research Section A: Accelerators, Spectrometers, Detectors and Associated Equipment* 2003;506:250-303.

34. Allison J, Amako K, Apostolakis J, Araujo H, Arce Dubois P *et al.* Geant4 developments and applications. *IEEE Transactions on Nuclear Science* 2006;53:270-278.

35. http://www.comsol.com.

36. www.imphyalloys.com.

CHAPTER 5.

CONCLUSIONS

In the present work we addressed fundamental aspects of the MRIgRT process of cancer sites: a) measure and correction of MRI scanner-related image distortions, b) MRI-based treatment planning (i.e. MRI Simulation) procedure for intracranial lesions, and c) magnetic shielding and dosimetric effects of the MRI-Linac system,

Following an introduction in Chapter 1, in Chapter 2 we described an MR image distortion correction method that relies on a) an adaptive control points' identification and registration tool and b) an iterative algorithm that calculates the best estimate of 3D distortion. By applying this technique the distortions were successfully mapped within the voxel resolution of the raw imaging data (0.94 x 0.94 x 1 mm^3). Specifically, for a 260 × 260 × 240 mm^3 phantom volume the total maximum distortion was found to be 5.55 mm with a μ and σ of 1.86 mm and 0.41, respectively. After correcting the image datasets, the residual distortion metrics were 0.55 mm/0.14 mm/0.05, respectively. This distortion correction method was implemented as an image processing preliminary step of the MRI-based treatment planning procedure for brain lesions, which was presented in Chapter 3. The MRI Simulation technique consists of a) correction of the

MR images for 3D distortions (Chapter 2), b) automatic segmentation of head sub-structures (i.e. scalp, bone, and brain) relevant for dosimetric calculations, c) preparation of the MRI datasets for dose calculations by assigning bulk CT values to head sub-structures and performing MR-based dose calculations in Eclipse TPS, and d) RT plan evaluation process based on isodose distributions, various dosimetric parameters, DVHs, and an RT ranking tool. We showed that the proposed MRI-based treatment planning procedure performed similarly to the standard clinical technique (within 1%), which relies on both CT and MR imaging modalities. This suggests that the MRI Simulation procedure is suitable for the radiotherapy of brain cancer.

Regarding the operation of an MRI-Linac system, in Chapter 4 we investigated by means of Monte Carlo methods the dosimetric effects caused by an external magnetic field in semi-infinite slab phantoms (i.e. water, lung and air media). We considered two fundamentally distinct MRI-Linac system configurations, i.e. RBP and FC, in the case of low (0.2 T) as well as high (1.5 T) magnetic fields. For our proposed configuration (i.e. 0.2 T field and RBP geometry) the maximum dose difference with regard to the 0 T case was found to be within 6 % in a uniform water phantom. The magnitude of these effects doubles for a water-lung-water phantom. The dose deposited patterns suggest that simple corrections could be implemented by slightly shifting the dose distributions along the direction of the Lorentz force. Such an adjustment can be specified because the dose shifts are correlated with the density of the targeted material (e.g. lung). In Chapter 4 we also covered a passive shielding method for developed for our MRI-Linac system based on a 0.2 T bi-planar magnet. The magnet was simulated using COMSOL, a FEM-based software package. The components of the passive shielding configuration were introduced and optimized to minimize the magnetic interference between the magnet and the linac. This was achieved by reducing the fringe field in the Linac-MLC region below earth's magnetic field, i.e. 0.5 G. The shielding consisted of a) two 10 cm thick steel (1020) plates placed at 10 cm away from the structure on opposite sides of the magnet and b) a box lined with a 1 mm MuMetal™ wall surrounding the Linac and MLC components.

The magnetic shielding and dosimetric calculations are essential for the optimal construction and operation of the MRI-Linac system whereas the MRI Simulation procedure represents a clinical application of the system.

In the case of an MRI-Linac system, the RTP workflow would consist of the following steps (see diagram in Fig. 5.1):

a) The patient is subjected to an MRI scan for diagnosis purposes;

b) RT planning is performed using only MRI data from step (a) (i.e. MRI Simulation);

c) Patient is repositioned for treatment by using an MRI-based RTP verification method. Such a method would be based on the image registration process of the diagnostic MRI scan (step (a)) and real-time MRI data, e.g. several image slices recorded at specific locations/orientations;

d) Radiation treatment delivery begins. The tumor site needs to be monitored in real-time by fast acquisition of MRI data;

e) If tumor volume changes location (e.g. due to breathing) during the delivery of radiation the delivery process needs to be adapted to these variations. The change in anatomy is detected by comparing (e.g. deformable registration) tumor contours, i.e. from steps (b) and (d). It is common that over the course of the treatment (weeks) the tumor location and/or volume varies, which requires the re-adjustment of the patient position (step (c)) and/or the RT plan (step (b)), respectively;

f) End of treatment planning and patient follow-up.

Future work may involve:

i. <u>The construction of the MRI-Linac system.</u> For clinical applications, the magnet-linac system has to revolve around a certain imaging/treatment active volume to allow the radiation beam(s) delivery from any desired angle. This pose the

challenging problem of rigidly mounting the MRI (heavy component) and linac in a configuration that would allow their unison rotating motion;

ii. Development of RTP verification techniques based solely on MRI data. Such methods rely on the registration process of subsequently acquired MRI data: e.g. diagnostic dataset (used for RTP) and up-to-date scans (before each treatment fraction). By analyzing the local characteristics of the image pixel information, similar reference organ structures can be identified in these corresponding image datasets. As a result, we can determine the organs relative image topography, i.e. size and spatial location. This information is required to re-align the patient in the treatment frame of reference.

iii. Real-time tumor tracking based on deformable image registration methods. During treatment delivery the target's shape and location may vary due to internal motion of surrounding structures. It is paramount to map the local behaviour of the tumor during irradiation process to ensure the efficiency of the latter. This can be accomplished by subsequent/periodic image sampling of the targeted anatomy using fast MR imaging techniques (e.g. navigator echo). Specifically, tumor information is resolved on the acquired images (i.e. tumor tracking) by analyzing image pixel local patterns (i.e. deformable registration).

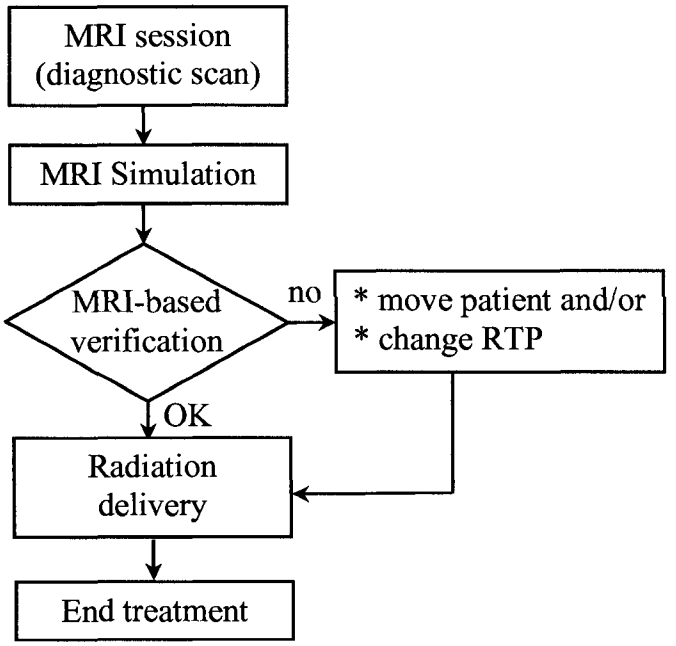

Figure 5.1. The treatment planning process for an MRI-Linac system.

APPENDIX

A.1 STATIONARY STATES OF A SINGLE ISOLATED SPIN

The interaction energy (ξ) corresponding to a proton at rest placed in a spatially uniform external magnetic field ($\vec{B}_0$) is given by the scalar product of its magnetic moment ($\vec{\mu}$) and $\vec{B}_0$ as follows

$$\xi = -\vec{\mu} \cdot \vec{B}_0 . \tag{A.1}$$

where the minus sign suggests that the magnetic energy is minimal when $\vec{\mu}$ is parallel to $\vec{B}_0$. In the case of a nuclear magnetic moment we have

$$\vec{\mu} = \gamma \hbar \vec{J} \tag{A.2}$$

where $\hbar = h/(2\pi)$ in terms of Planck's quantum constant h, $\vec{J}\hbar$ is the nuclear spin angular momentum, and γ is the gyromagnetic ratio, a constant that is fixed for each nuclei species. From Eqs. (A.1) and (A.2) the interaction energy can be expressed as

$$\xi = -\gamma \hbar \vec{J} \cdot \vec{B}_0 . \tag{A.3}$$

Considering that we apply a static magnetic field along z-axis, i.e. $\vec{B}_0 = (0,0,B_0)$ Eq. (A.3) becomes

$$\xi = -\gamma \hbar J_z B_0 \tag{A.4}$$

where J_z is a quantum mechanics operator. For our particular system introduced above, the Hamiltonian, i.e. energy's operator, is given by the interaction energy

$$H \equiv \xi = -\gamma \hbar J_z B_0 . \tag{A.5}$$

Considering Schrödinger equation

$$H\psi = i\hbar \frac{\partial \psi}{\partial t} \tag{A.6}$$

and by applying the method of separation of variables for stationary states, namely the spin wave functions (i.e. energy eigenstates) given by $\psi(\vec{r},t) = \varphi(\vec{r}) e^{\frac{i}{\hbar}Et}$, the energy eigenstates are solutions of

$$H\psi = E_0 \psi \tag{A.7}$$

where E_0 is an energy eigenvalue. From Eqs. (A.5) and (A.7) we obtain

$$-\gamma \hbar J_z B_0 \psi = E_0 \psi . \tag{A.8}$$

Eq. (A.8) suggests that the energy eigenstates are also eigenstates of the J_z operator, namely

$$E_0 = \pm \frac{1}{2} \gamma \hbar B_0 . \tag{A.9}$$

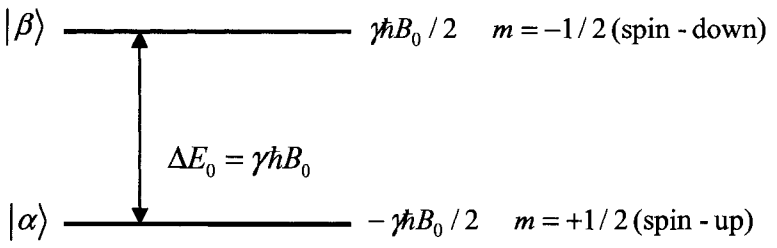

Figure A.1. Energy level diagram representing energy eigenvalues, energy eigenstates ($|\alpha\rangle$ and $|\beta\rangle$) and their corresponding magnetic quantum number (i.e. m) of a proton spin in a constant magnetic field.

Therefore, there are only two energy states available for our proton. This aspect can be represented by an energy level diagram as shown in Fig. A.1. The energy difference can also be expressed as $\Delta E_0 = \hbar\omega_0$, where $\omega_0 = -\gamma B_0$ represents the Larmor frequency. Hence, ΔE is linearly proportional to the strength of the applied magnetic field, i.e. Zeeman effect.

The terms spin-up and spin-down refer to the z-component of the angular momentum, i.e. $m\hbar$, only. Considering that the spin vector value is $\hbar\sqrt{s(s+1)}$, with s being the spin quantum number, and $-s < m < s$ we can infer that the magnitude of the spin vector is larger than its z component. Therefore, the spin vector $\vec{J}$ can lie with equal probability anywhere on the surface of a cone (centered on the z-axis).

At any moment, the proton's spin has a certain probability of being in either spin-up or spin-down state. For a general wavefunction we can express this concept as a weighted sum of energy eigenstates

$$\psi = C_+|\alpha\rangle + C_-|\beta\rangle \tag{A.10}$$

where coefficients C_+ and C_- represent the relative proportions of $|\alpha\rangle$ and $|\beta\rangle$ states. The proton's spin probabilities of being only in the spin-up or spin-down state are $C_+^* C_+ = |C_+|^2$ and $C_-^* C_- = |C_-|^2$, respectively.

A.2 ENSEMBLE OF SPINS ½ - ON MAXWELL-BOLTZMANN STATISTICS

Let us assume an ensemble of isolated spins ½. For a set of energy eigenstates $|i\rangle$ the Hamiltonian is

$$H|i\rangle = \omega_i|i\rangle \tag{A.11}$$

where ω_i are the energy eigenvalues corresponding to $|i\rangle$. In thermal equilibrium, the populations of energy states are governed by the classical Maxwell-Boltzmann distribution as follows

$$\overline{P}_i^{th-eq} = \frac{e^{-\hbar\omega_i / k_B T}}{\sum_n e^{-\hbar\omega_n / k_B T}} \tag{A.11}$$

where k_B is Boltzmann constant and T is the absolute temperature. The denominator is given by the sum over all energy states available, i.e. in our case $|\alpha\rangle$ and $|\beta\rangle$ (see Fig. A.1). This process

is not characterized by the Fermi-Dirac statistics as the distances between protons are large resulting in weak interactions.

Considering Larmor frequency (ω_0), introduced in Appendix A.1, the energy eigenvalues are given by

$$\begin{aligned} \omega_{|\alpha\rangle} &= +\frac{1}{2}\omega_0 \\ \omega_{|\beta\rangle} &= -\frac{1}{2}\omega_0 \end{aligned} \tag{A.12}$$

The Boltzmann factor is defined as follows

$$B = \frac{\Delta E}{k_B T} \tag{A.13}$$

where $\Delta E = \hbar\omega_0$ represents the energy difference between the $|\alpha\rangle$ and $|\beta\rangle$ states (see Appendix A.1).

Considering Eq. (A.13), for $|\alpha\rangle$ and $|\beta\rangle$ Eq. (A.11) can be written as

$$\begin{aligned} \overline{P}_{|\alpha\rangle}^{th-eq} &= \frac{e^{B/2}}{e^{B/2} + e^{-B/2}} \\ \overline{P}_{|\beta\rangle}^{th-eq} &= \frac{e^{-B/2}}{e^{B/2} + e^{-B/2}} \end{aligned} \tag{A.14}$$

where $\overline{P}_{|\alpha\rangle}^{th-eq}$ and $\overline{P}_{|\beta\rangle}^{th-eq}$ represent the ensemble averages of the probabilities of finding a spin in $|\alpha\rangle$ and $|\beta\rangle$, respectively.

In practice, $\Delta E_0 << k_B T$, ΔE_0 is roughly five orders of magnitude smaller than thermal energy $k_B T$. Therefore, B is also small and as a consequence we can simplify Eqs. A.14 and obtain the following equations

$$\begin{aligned} \overline{P}_{|\alpha\rangle}^{th-eq} &\cong \frac{1}{2} + \frac{1}{4} B \\ \overline{P}_{|\beta\rangle}^{th-eq} &\cong \frac{1}{2} - \frac{1}{4} B \end{aligned} \tag{A.15}$$

A.3 SPINS EXCITATION PROCESS - ROTATING FRAME

To perturb the net magnetization ($\vec{M}$) of a spin system placed in a static magnetic field $\vec{B}_0$, a second magnetic field ($\vec{B}_1$) has to be applied. As a result, the spins behaviour is governed by a net magnetic field given by

$$\vec{B} = \vec{B}_0 + \vec{B}_1(t) \tag{A.16}$$

where $\vec{B}_0 = (0,0,B_0)$, $\vec{B}_1(t) = (B_1 \cos\omega_1 t, B_1 \sin\omega_1 t, 0)$ is a time dependant and circularly polarized magnetic field rotating about $\vec{B}_0$, ω_1 is the angular frequency corresponding to $\vec{B}_1$, and t is the time variable.

The equation of motion for $\vec{M} = (M_x, M_y, M_z)$ is given by

$$\dot{\vec{M}} = \gamma \vec{M} \times \vec{B} = \gamma \begin{vmatrix} \vec{i} & \vec{j} & \vec{k} \\ M_x & M_y & M_z \\ B_1 \cos \omega_1 t & B_1 \sin \omega_1 t & B_0 \end{vmatrix} \tag{A.17}$$

The components of Eq. (A.17) are as follows

$$\begin{cases} \dot{M}_x = \gamma \left(M_y B_0 - M_z B_1 \sin \omega_1 t \right) \\ \dot{M}_y = \gamma \left(M_z B_1 \cos \omega_1 t - M_x B_0 \right) \\ \dot{M}_z = \gamma \left(M_x B_1 \sin \omega_1 t - M_y B_1 \cos \omega_1 t \right) \end{cases} \tag{A.18}$$

At this point, it is easier to describe the interaction process between $\vec{M}$ and $\vec{B}$ by using a new system of reference attached to $\vec{B}_1$, i.e. rotating frame $(\vec{i}_\rho, \vec{j}_\rho, \vec{k}_\rho)$, which is shifted from the initial laboratory frame by the angle $\omega_1 t$. This approach is equivalent to viewing the nuclear spins from a reference frame revolving around the z-axis. Namely, $\vec{M}$ becomes $\vec{M}_\rho$ with its components given by

$$\begin{cases} M_{x\rho} = M_x \cos \omega_1 t + M_y \sin \omega_1 t \\ M_{y\rho} = -M_x \sin \omega_1 t + M_y \cos \omega_1 t \\ M_{z\rho} = M_z \end{cases} \tag{A.19}$$

In the new system of reference both $\vec{B}_0$ and $\vec{B}_1$ are static fields.

Considering Eqs. (A.18), the equation of motion corresponding to $\vec{M}_\rho$ are

$$\begin{cases} \dot{M}_{x\rho} = (\omega_1 + \gamma B_0) M_{y\rho} \\ \dot{M}_{y\rho} = -(\omega_1 + \gamma B_0) M_{x\rho} + \gamma B_1 M_{z\rho} \\ \dot{M}_{z\rho} = -\gamma B_1 M_{y\rho} \end{cases} \tag{A.20}$$

Eqs. (A.20) can be merged into a single vector equation as follows

$$\dot{\vec{M}}_\rho = \begin{vmatrix} \vec{i}_\rho & \vec{j}_\rho & \vec{k}_\rho \\ M_{x\rho} & M_{y\rho} & M_{z\rho} \\ \gamma B_1 & 0 & \omega_1 + \gamma B_0 \end{vmatrix} = \gamma \vec{M}_\rho \times \vec{B}_{eff} \tag{A.21}$$

where

$$\vec{B}_{eff} = B_1 \cdot \vec{i}_\rho + (B_0 + \omega_1 / \gamma) \cdot \vec{k}_\rho \tag{A.22}$$

Eq. (A.22) corresponding to the rotating frame has a similar form as Eq. (A.16) of the initial laboratory frame. The fundamental difference between the two is that $\vec{B}$ is replaced by $\vec{B}_{eff}$.

A.4 RELAXATION PROCESS - BLOCH EQUATIONS

The protons' relaxation process, after an RF pulse, can be characterized by using a simple phenomenological model based on Bloch equations. However, this approach has some limitations, namely it can not be used to describe NMR spectra (quantum effects have to be considered). The Bloch equations are[1]

$$\frac{d\vec{M}}{dt} = \gamma \vec{M} \times \vec{B}_0 - \frac{M_x \vec{i} + M_y \vec{j}}{T_2} + \frac{M_0 - M_z}{T_1} \vec{k} \tag{A.23}$$

where $\vec{M}$ is the net magnetization vector, i.e. $\vec{M} = (M_x, M_y, M_z)$, M_0 represents the thermal equilibrium value of $|\vec{M}|$, γ is the gyromagnetic ratio, $\vec{B}_0$ is the externally applied magnetic field, T_1 and T_2 are the longitudinal and transverse relaxation time constants, t is time variable, and $(\vec{i}, \vec{j}, \vec{k})$ represents the unit vectors of the laboratory system of reference.

Expanding the cross-product in Eq. (A.23) we obtain

$$\frac{d\vec{M}}{dt} = \gamma \begin{vmatrix} \vec{i} & \vec{j} & \vec{k} \\ M_x & M_y & M_z \\ 0 & 0 & B_0 \end{vmatrix} - \frac{M_x \vec{i} + M_y \vec{j}}{T_2} + \frac{M_0 - M_z}{T_1} \vec{k} \tag{A.24}$$

The three components of $\vec{M}$ are given by

$$\begin{cases} \dfrac{dM_x}{dt} = \gamma M_y B_0 - \dfrac{M_x}{T_2} \\ \dfrac{dM_y}{dt} = -\gamma M_x B_0 - \dfrac{M_y}{T_2} \\ \dfrac{dM_z}{dt} = \dfrac{M_0 - M_z}{T_1} \end{cases} \tag{A.25}$$

The general solutions of Eqs. (A.25) are[1]

$$\begin{cases} M_x(t) = e^{-t/T_2}\left[M_x(0)\cos(\gamma B_0 t) + M_y(0)\sin(\gamma B_0 t)\right] \\ M_y(t) = e^{-t/T_2}\left[M_y(0)\cos(\gamma B_0 t) - M_x(0)\sin(\gamma B_0 t)\right] \\ M_z(t) = M_z(0)e^{-t/T_1} + M_0(1 - e^{-t/T_1}) \end{cases} \tag{A.26}$$

Eq. (A.23) represents the reduced form of Bloch equations. By adding certain terms, the diffusion and chemical exchange processes can also be described by these equations. In general, Bloch equations apply successfully to media characterized by high molecular mobility. However, they fail to accurately describe rigid systems, i.e. strongly dipole coupled, as the T_2 decay shows a non-exponential behaviour.

A.5 LOCAL WEIGHTED MEAN TRASFORMATION

The local weighted mean (lwm) transformation consists of a) establishing a certain correspondence between the MRI and CT sets of control points and b) inferring a spatial transformation function based on the position of the control points. The transformation function maps any arbitrarily selected point in the volume of interest and is given by[2]

$$f(x,y)=\frac{\sum_{i=1}^{N} W_i(R)\cdot P_i(x,y)}{\sum_{i=1}^{N} W_i(R)} \tag{A.27}$$

where $W_i(R)$ represents the weighting functions, which are defined as

$$\begin{cases} W_i(R)=1-3R^2+2R^3,\ 0\le R\le 1,\ i=1,...N \\ W_i(R)=0,\ R>1 \end{cases} \tag{A.28}$$

with $R=\left[(x-x_i)^2+(y-y_i)^2\right]^{1/2}/R_n$, $i=1,...N$, where (x,y) and (x_i,y_i) represent the coordinates of the CT and MRI control points, respectively; R_n is the displacement of point (x_i,y_i) from its corresponding (n-1)th nearest control point; and N is the number of control points used in the

transformation. In Eq. (A.27), $P_i(x,y)$ represents the polynomials used to fit the positions of the (x_i,y_i) control point and its (n-1)th nearest control points and is given by

$$P_i(x,y)=\sum_{j=0}^{n}\sum_{k=0}^{j}a_{jk}x_i^k y_i^{j-k},\ i=1,...,N \tag{A.29}$$

where n is the order of the polynomial (i.e. in our case $n = 2$).

A.6 BICUBIC CONVOLUTION INTERPOLATION

A typical form of a bicubic interpolation function is given by

$$f(x)=\sum_i c_i \cdot u\left(\frac{x-x_i}{h}\right) \tag{A.30}$$

where u represents the interpolation kernel, x_i are the interpolation nodes, h is the sampling increment, and coefficients c_i are chosen in such a way that the interpolation condition $f(x_i)=g(x_i)$ is fulfilled. g represents the sampled function for each discrete interpolation node. The interpolation kernel used in Matlab for the bicubic interpolation is based on the work of Keys[3] and is given by

$$u(x)=\begin{cases}(a+2)\cdot|x|^3-(a+3)\cdot|x|^2+1, & |x|\le 1\\ a\cdot|x|^3-5a\cdot|x|^2+8a\cdot|x|-4a, & 1<|x|\le 2\\ 0, \text{ otherwise}\end{cases} \tag{A.31}$$

where a is a constant, which can take the values -0.5 or -0.75 only. In Matlab a is set to -0.5. Replacing a in Eq. (A.31) we obtain

$$u(x)=\begin{cases}1.5\cdot|x|^3-2.5\cdot|x|^2+1, & |x|\le 1\\ -0.5\cdot|x|^3+2.5\cdot|x|^2-4\cdot|x|+2, & 1<|x|\le 2\\ 0, \text{ otherwise}\end{cases}. \tag{A.32}$$

A.7 REFERENCES

1. Haacke E, Brown RW, Thompson MR, Venkatesan R. Magnetic Resonance Imaging. Physical Principles and Sequence Design: John Wiley & Sons, Inc.; 1999
2. Goshtasby A. Image registration by local approximation methods. *Image and Vision Computing* 1988;6:255-261
3. Keys R. Cubic Convolution Interpolation for Digital Image Processing. *IEEE Transactions on Acoustics, Speech, and Signal Processing* 1981;ASSP-29:1155-1160.

BIBLIOGRAPHY

Agostinelli S, Allison J, Amako K, Apostolakis J, Araujo H *et al.* GEANT4 - a simulation toolkit. *Nuclear Instruments and Methods in Physics Research Section A: Accelerators, Spectrometers, Detectors and Associated Equipment* 2003;506:250-303. [p. 142]

Allison J, Amako K, Apostolakis J, Araujo H, Arce Dubois P *et al.* Geant4 developments and applications. *IEEE Transactions on Nuclear Science* 2006;53:270-278. [p. 142]

Amanie J, Robinson D, Murray B, Field C, Warkentin B, Stavrev P, et al. Comparison of dose-escalated and intensity- modulated three-dimensional conformal radiotherapy plans in patients with localized non-small-cell lung cancer. *Curr Oncol* 2004;11:93. [p. 85, 95]

Ashburner J, Friston KJ. Unified segmentation. *Neuroimage* 2005;26:839-851. [p. 89]

Bakker C, Moerland MA, Bhagwandien R and Beersma R. Analysis of machine-dependant and object-induced geometric distortion in 2DDT MR imaging. *Magn. Reson. Imaging* 1992;10:597-608. [p. 4, 36, 84]

Baldwin L, Wachowicz K, Thomas SD, Rivest R, Fallone BG. Characterization, prediction, and correction of geometric distortion in 3 T MR images. *Med Phys* 2007;34:388-399. [p. 4, 28, 39, 68, 73, 74, 84]

Balter J, Sandler HM, Lam K, Bree RL, Lichter AS, Haken RK Measurement of prostate movement over the course of routine radiotherapy using implanted markers *Int. J. Radiat. Oncol. Biol. Phys.* 1995;31 113–118. [p. 2]

Baro J, Sempau J, Fernandez-Varea JM, *et al.* PENELOPE: an algorithm for Monte Carlo simulation of the penetration and energy loss of electrons and positrons in matter. *Nucl. Instrm. Methods Phys. Res B* 1995;100:31-46. [p. 118]

Beavis A, Gibbs P, Dealey RA, Whitton VJ. Radiotherapy treatment planning of brain tumors using MRI alone. *Br J Rad* 1998;71:544-548. [p. 70, 73, 88, 97]

Berger M, Coursey JS, Zucker DS. ESTAR, PSTAR, and ASTAR: Computer Programs for Calculating Stopping-Power and Range Tables for Electrons, Protons, and Helium Ions (version 1.2.2). [Online] Available: http://physics.nist.gov/Star 2005;(National Institute of Standards and Technology, Gaithersburg, MD, 2005). [p. 122]

Bhagwandien R, Moerland MA, Bakker CJ, Beersma R, Lagendijk JJ. Analysis of patient induced marker shifts in MRI. Proceedings Eleventh Annual Meeting of the Society for Magnetic Resonance in Medicine (SMRM); 1992. p. 4305. [p. 35]

Bhagwandien R. Object induced geometry and intensity distortions in magnetic resonance imaging: PhD thesis, University of Utrecht, The Netherlands; 1994. [p. 35, 84, 88]

Bhagwandien R, Moerland MA, Bakker CJ, Beersma R, Lagendijk JJ. Numerical analysis of the magnetic field for arbitrary magnetic susceptibility distributions in 3D. *Mag Res Imag* 1994;12:101-107. [p. 35, 88]

Bhangwandien R, van Ee R, Beersma R and Bakker C J G. Numerical Analysis of the Magnetic Field for Arbitrary Magnetic Susceptibility Distributions in 2D. *Mag. Res. Imag.* 1992;10:299-313. [p. 35]

Bielajew AF. The effect of strong longitudinal magnetic fields on dose deposition from electron and photon beams. *Med Phys* 1993;20:1171-1179. [p. 97]

Bloch F. Nuclear induction. Phys. Rev. Vol 70; 1946. p. 460. [p. 7]

Bloch F, Hansen WW, Packard M. The nuclear induction experiment. *Phys. Rev.* 1946;70:474. [p. 7]

Bradley W, Waluch V, Yadley RA, Wycoff RR. Comparison of CT and MR in 400 patients with suspected disease of the brain and cervical spinal cord. *Radiology* 1984;152:695-702. [p. 7, 82]

Brahme A. Dosimetric precision requirements in radiation therapy. *Acta Radiol Oncol* 1984;23:379-391. [p. 95]

Brant-Zawadzki M. MR imaging of the brain. *Radiology* 1988;166:1-10. [p. 82]

Breeuwer M, Holden M, Zylka W Detection and correction of geometric distortion in 3D MR images. Proc of SPIE Image Processing. Vol 4322 2001. pp. 1110-1120. [p. 35, 53]

Bydder G, Steiner RE, Young IR, Hall AS, Thomas DJ, Marshall J, Pallis CA, Legg NJ. Clinical NMR imaging of the brain: 140 cases. *AJR* 1982;139:215-236. [p. 7]

Carlone M, Lamey M, Steciw S, Burke B, Fallone B. Study of RF Interference Between a Linear Accelerator and MRI. [Abstract]. *Med Phys* 2007;34:2621. [p. 2, 116]

Carlone M, Warkentin B, Stavrev P, Fallone B G. Fundamental form of the population TCP model in the limit of large heterogeneity. *Med Phys* 2006;33:1634-1642. [p. 95]

Chang H, Fitzpatrick JM. A technique for accurate magnetic resonance imaging in the presence of field inhomogeneities. *IEEE T Med Imaging* 1992;11:319-329. [p. 4, 35, 84]

Chang H, and Fitzpatrick J M Geometrical image transformation to compensate for MRI distortions. Proc. SPIE Vol 1233; 1998. pp. 116-127. [p. 36]

Chen L, Price R A Jr, Wang L, Li J, Qin L, McNeeley S, et al MRI-based treatment planning for radiotherapy: dosimetric verification for prostate IMRT. *Int. J. Radiat. Oncol. Biol. Phys.* 2004;60:636-647. [p. 4, 34, 75, 83]

Chen L, Price Jr. RA., Nguyen T-B, et al. Dosimetric evaluation of MRI-based treatment planning for prostate cancer. *Phys Med Biol* 2004;49:5157-5170. [p. 4, 21, 34, 75, 83]

Chen L, Thai-Binh N, Elan MS, Chen Z, Wei L, Lu W, Price RA., Pollack A, Ma C. Magnetic resonance-based treatment planning for prostate intensity-modulated radiotherapy: creation of digitally reconstructed radiograhs. *Int J Radiat Oncol Biol Phys* 2007;68:903-911. [p. 4, 69, 71, 83]

Chen Z, Ma CM, Paskalev K, Li J, Yang J, Richardson T, Palacio L, Xu X and Chen L. Investigation of MR image distortion for radiotherapy planning of prostate cancer. *Phys Med Biol* 2006;51:1393-1403. [p. 35, 83, 84]

Chen Y, Bielajew AF, Litzenberg DW, Moran JM, Becchetti FD. Magnetic confinement of electron and photon radiotherapy dose: a Monte Carlo simulation with a nonuniform longitudinal magnetic field. *Med Phys* 2005;32:3810-3818. [p. 118, 119]

Coffey C, Hines HC, Wang PC, Smith SL. The early applications and potential usefulness of NMR in radiation therapy treatment planning. Proc. Eighth International Conference on the Use of Computers in Radiation Therapy. Toronto, Canada; 1984. pp. 173-180. [p. 7]

Collins D, Neelin P, Peters TM and Evans AC. Automatic 3D Inter-Subject Registration of MR Volumetric Data in Standardized Talairach Space. *Journal of Computer Assisted Tomography* 1994;18:192-205. [p. 89]

Collins D, Holmes CJ, Peters TM, and Evans AC. Automatic 3D model-based neuroanatomical segmentation. *Human Brain Mapping* 1995;3:190-208. [p. 89]

Damadian R. Tumor Detection by Nuclear Magnetic Resonance. *Science* 1971;171:1151-1153. [p. 7]

Dempsey J, Benoit D, Fitzsimmons JR, Haghighat A, Li JG et al. A Device for Realtime 3D Image-Guided IMRT. 2005;47th Annual ASTRO General Meeting, Denver, CO. [p. 2, 116]

Doran SJ, Charles-Edwards L, Reinsberg S A and Leach M O. A complete distortion correction for MR images: I. Gradient warp correction. *Phys. Med. Biol.* 2005;50:1343-1361. [p. 4, 5, 35, 36, 37, 38, 39, 49, 55, 59, 64, 65, 66, 69, 74, 75, 84]

Drake D, Jaffray DA, Wong JW Characterization of a fluoroscopic imaging system for kV and MV radiography. *Med. Phys.* 2000 27 898-905. [p. 2]

Elsen P. Multimodality matching of brain images. PhD thesis, University Hospital Utrecht, The Netherlands; 1993. [p. 35]

ICRU Report 62. Prescribing, Recording and Reporting Photon Beam Therapy (supplement to ICRU Report. 50). *International Commission on Radiation Units and Measurements* 1999:Bethesda, MD. [p. 2]

Fallone B, Carlone M, Murray B, Rathee S, Stanescu T, Steciw S, Wachowicz K, Kirkby C. Development of a Linac-MRI System for Real-Time ART. [Abstract]. *Med Phys* 2007;34:2547. [p. 2, 21, 86, 116, 117, 132]

Fallone B, Carlone M, Murray B, Rathee S, Stanescu T, Steciw S, Kirkby C, Tomanek B, Sharp J. Development of a Small Bore Linac-MRI System for Real Time Image Guided Radiotherapy. [Abstract]. *Radiother Oncol* 2007;84:S3. [p. 2, 116, 117, 129]

Fallone B, Carlone M, Murray B. Integrated External Beam Radiotherapy and MRI System. PCT International Patent. Vol WO/045076; 2007. pp. 5625-5635. [p. 2, 116, 117]

Fallone B, Carlone M, Murray B. Real-time Dose Reconstructed Using Dynamic Simulation and Image-Guided Adaptive Radiotherapy. PCT International Patent. Vol WO/045075; 2007. pp. 5625-5634. [p. 2, 116, 117]

Fraass B, McShan DL, Diaz RF, Ten Haken RK, Aisen A, et al. Integration of magnetic resonance imaging into radiation therapy treatment planning: I technical considerations. *Int J Radiat Oncol Biol Phys* 1987;13:1897-1908. [p. 4, 82]

Gilhuijs K, Van de Ven PJH, Van Herk M. Automatic three-dimensional inspection of patient setup in radiation therapy using portal images, simulator images, and computed tomography data. *Med. Phys.* 1996;23 389-399. [p. 2]

Glatstein E, Lichter AS, Fraass BA, van de Geijn J. The imaging revolution and radiation oncology: Use of CT, ultrasound and NMR for localization, treatment planning and treatment delivery. *Int J Rad Oncol Biol Phys* 1985;11:1299-1311. [p. 7]

Glazer G, Gross BH. Aisen AM, Quint LE, Francis IR, Orringer MB Imaging of the pulmonary hilum: A prospective comparative study in patients with lung cancer. *Am J Radiol* 1985;145:245-248. [p. 7]

Goshtasby A. Image registration by local approximation methods. *Image and Vision Computing* 1988;6:255-261. [p. 184]

Groh BA SJ, Drake DG, Wong JW, Jaffray DA A performance comparison of flat-panel imager-based MV and kV cone-beam CT *Med. Phys.* 2002 29 967-975. [p. 2]

Haacke E, Brown RW, Thompson MR, Venkatesan R. Magnetic Resonance Imaging. Physical Principles and Sequence Design: John Wiley & Sons, Inc.; 1999 [p. 182]

Heelan R, Martini K, Westcott JW, Bains MS, Watson RC et al. Carcinomatous involvement of the hilum and mediastinum: Computed tomographic and magnetic resonance evaluation. *Radiology* 1985;153:111-115. [p. 7]

Heester M, Wijrdeman HK, Strukmans H, Witkamp T, Moerland MA. Brain tumor delineation based on CT and MR imaging. *Strahlenther Onkol* 1993;169:729-733. [p. 34, 82]

Hill D, et al. Accurate frameless registration of MR and CT images of the head; applications in planning surgery and radiation therapy. *Radiology* 1994;191:447-454. [p. 19, 34, 84]

Jadetzky O, Wertz JF Detection of sodium complexes by nuclear spin resonance. *Am J Physiol* 1956;187:608. [p. 7]

Jaffray DA SJ, Wong JW, Martinez AA Flat-panel cone-beam computed tomography for image-guided radiation therapy. *Int. J. Radiat. Oncol. Biol. Phys.* 2002 53 1337-1349. [p. 2]

Janke A, Zhao H, Cowin GJ, Galloway J, Dodrell DM. Use of spherical harmonic deconvolution methods to compensate for nonlinear gradient effects on MRI images. *Mag Res Med* 2004;52:115-122. [p. 35, 84]

Jette D. Magnetic fields with photon beams: Monte Carlo calculations for a model magnetic field. *Med Phys* 2000;27:2726-2738. [p. 97]

Johnson P, Hunt SJ, Drayer BP. Human cerebral gliomas: correlation of postmortem MR imaging and neuropathologic findings. *Radiology* 1989;170:211-217. [p. 2, 4, 82]

Just M, Rosler HP, Higer HP, Kutzner J, Thelen M. MRI-assisted radiation therapy planning of brain tumors - clinical experience in 17 patients. *Magn Res Imag* 1991;9:173-177. [p. 28, 34, 84]

Kagawa K, Lee WR, Schultheiss TE, Hunt MA, Shaer AH and Hanks GE. Initial clinical assessment of CT-MRI image fusion software in localization of the prostate for 3D conformal radiation therapy. *Int J Radiat Oncol Biol Phys* 1997;38:319-325. [p. 34]

Karger CP, Hoss A, Bendl R, Canda V and Schad L. Accuracy of device-specific 2D and 3D image distortion correction algorithms for magnetic resonance imaging of the head provided by a manufacturer. *Phys. Med. Biol.* 2006;51:N253-N261. [p. 34, 43]

Keys R. Cubic Convolution Interpolation for Digital Image Processing. *IEEE Transactions on Acoustics, Speech, and Signal Processing* 1981;ASSP-29:1155-1160. [p. 185]

Khoo V, Joon DL. New developments in MRI for target volume delineation in radiotherapy. *Brit J Radiol* 2006;79:S2-S15. [p. 4, 82]

Kirkby C, Stanescu T, Rathee S, Carlone M, Murray B, Fallone BG. Patient dosimetry for hybrid MRI-radiotherapy systems. *Med Phys* 2008;(in press). [p. 117]

Krempien R, Schubert K, Zierhut D, Steckner MC, Treiber M et al Open low-field magnetic resonance imaging in radiation therapy treatment planning. *Int J Rad Oncol Biol Phys* 2002;53:1350-1360. [p. 35, 53]

Kron T, Eyles D, Schreiner JL, Battista J. Magnetic resonance imaging for adaptive cobalt tomotherapy: A proposal. *J Med Phys* 2006;31:242-254. [p. 2, 116, 117]

Kumar A, Welti D, Ernst R. NMR Fourier zeugmatography. *J Magn Reson* 1975;18:69-83. [p. 7]

Lagendijk J, Raaymakers BW, van der Heide U, Overweg J, Brown K et al. In Room Magnetic Resonance Imaging Guided Radiotherapy (MRIgRT). *Med Phys* 2005;32:2067. [p. 2, 116, 117, 123]

Lauterbur P. Image Formation by Induced Local Interactions: Examples Employing Nuclear Magnetic Resonance *Nature* 1973;242:190-191. [p. 7]

Lee YK, Bollet M, Charles-Edwards G, Flower M A, Leach M O, McNair H, et al. Radiotherapy treatment planning of prostate cancer using magnetic resonance imaging alone *Radiother. Oncol.* 2003;66:203-216. [p. 4, 34, 75, 83]

Li XA, Reiffel L, Chu J, *et al.* Conformal photon-beam therapy with transverse magnetic fields: a Monte Carlo study. *Med Phys* 2001;28:127-133. [p. 97]

Mackie TR HT, Swerdloff S, Reckwerdt P, Deasy JO, Yang J, Paliwal B, Kinsella T Tomotherapy: a new concept for the delivery of dynamic conformal radiotherapy *Med. Phys.* 1993 20 1709-1719. [p. 2]

Mansfield P. Multi-planar image formation using NMR spin-echos. *J Phys C: Solid State Physics* 1977;10:L55-L58. [p. 7]

Mizowaki T, Nagata Y, Okajima K, et al. Reproducibility of geometric distortion in magnetic resonance imaging based on phantom studies. *Radiother & Oncol* 2000;57:237–242. [p. 35]

Moerland M, Beersma R, Bhagwandien R, Wijrdeman HK, Bakker CJG. Analysis and correction of geometric distortions in 1.5 T magnetic resonance images for use in radiotherapy treatment planning. *Phys Med Biol* 1995;40:1651-1664. [p. 35, 88]

Moerland M. Magnetic resonance imaging in radiotherapy treatment planning: PhD thesis, University of Utrecht, The Netherlands; 1996. [p. 70]

Morris M, Greiner R, Sander J, Murtha A, and Schmidt M. A Classification-based Glioma Diffusion Model Using MRI Data. Proc. Canadian Conference of Artificial Intelligence. Quebec City); 2006. [p. 44]

Murray B, Fallone G, Carlone M, Steciw S, Stanescu T, Rathee S. Designing a Linac to Operate Near an MRI. [Abstract]. *Radiother Oncol* 2007;84:S3. [p. 2, 116, 129]

Nederveen A, Lagendijk JJW, Hofman P. Feasibility of automatic marker detection with an a-Si flat-panel imager. *Phys. Med. Biol.* 2001;46. [p. 2]

Odeblad K, Bhar NB, Lindstrom G. Proton magnetic resonance of human red blood cells in heavy water exchange experiments. *Arch Biochem Biophys* 1956;63:221-225. [p. 7]

Purcell E, Torrey HC, Pound R. Resonance Absorption by Nuclear Magnetic Moments in a Solid. *Phys Rev* 1946;69:37-38. [p. 7]

Purdy J. Principals and Practice of Radiation Oncology. 3 ed: Lippincott-Raven; 1997. [p. 4, 82]

Raaijmakers AJ, Raaymakers BW, Lagendijk JJ. Integrating a MRI scanner with a 6 MV radiotherapy accelerator: dose increase at tissue-air interfaces in a lateral magnetic field due to returning electrons. *Phys Med Biol* 2005;50:1363-1376. [p. 2, 116, 117, 142]

Raaijmakers AJ, Raaymakers BW, Lagendijk JJ. Experimental verification of magnetic field dose effects for the MRI-accelerator. *Phys Med Biol* 2007;52:4283-4291. [p. 2, 116, 142]

Raaijmakers AJ, Raaymakers BW, van der Meer S, *et al.* Integrating a MRI scanner with a 6 MV radiotherapy accelerator: impact of the surface orientation on the entrance and exit dose due to the transverse magnetic field. *Phys Med Biol* 2007;52:929-939. [p. 2, 116, 117, 142]

Raaymakers BW, Raaijmakers AJ, Kotte AN, *et al.* Integrating a MRI scanner with a 6 MV radiotherapy accelerator: dose deposition in a transverse magnetic field. *Phys Med Biol* 2004;49:4109-4118. [p. 2, 116, 117, 142]

Ramsey C, Arwood D, Scaperoth D, Oliver AL. Clinical application of digitally-reconstructed radiographs generated from magnetic resonance imaging for intracranial lesions. *Int J Radiat Oncol Biol Phys* 1999;45:797-802. [p. 4, 86]

Ramsey C, Oliver AL. Magnetic resonance imaging based digitally reconstructed radiographs, virtual simulation, and three-dimensional treatment planning for brain neoplasms. *Med Phys* 1998;25. [p. 101]

Ramsey C, Cordrey IL, Spencer KM, Oliver AL. Dosimetric verification of two commercially available three-dimensional treatment planning systems using TG23 test package. *Med Phys* 1999;26:1188-1195. [p. 101]

Rasch C, Barillot I, Remeijer P, Tpuw A, van Herk M and Lebesque JV. Definition of the prostate in CT and MRI: a multi-observer study. *Int J Radiat Oncol Biol Phys* 1999;43:57-66. [p. 34]

Reiffel L, Li A, Chu J, *et al.* Control of photon beam dose profiles by localized transverse magnetic fields. *Phys Med Biol* 2000;45:N177-182. [p. 97]

Reinsberg S, Doran SJ, Charles-Edwards EM, Leach MO. A complete distortion correction for MR images: II. Rectification of static-field inhomogeneities by similarity-based profile mapping. *Phys Med Biol* 2005;50:2651-2661. [p. 4, 35]

Roach M, Faillace-Akazawa P, Malfatti C, Holland J and Hricak H. Prostate volumes defined by magnetic resonance imaging and computerized tomographic scans for 3-dimensional conformal radiotherapy. *Int J Radiat Oncol Biol Phys* 1996;35:1011-1018. [p. 34]

Ruchala K, Olivera GH, Schloesser EA, Mackie TR Megavoltage CT on a tomotherapy system. . *Phys. Med. Biol.* 1999 44 2597-2621. [p. 2]

Sailer S, Rosenman JG, Soltys M, et al. Improving treatment planning accuracy through multimodality imaging. *Int J Radiat Oncol Biol Phys* 1996;35:117-124. [p. 2, 4, 82]

Schad L, Lott S, Schmitt F, et al. Correction of spatial distortion in MR Imaging: A prerequisite for accurate stereotaxy. *J Comput Assist Tomo* 1987;11:499-505. [p. 70]

Schad L, Bluml S, Hawighorst H, Wenz F, Lorenz W. Radiosurgical treatment planning of brain metastases based on a fast, three-dimensional MR imaging technique. *Magn Reson Imaging* 1994;12:811-819. [p. 101]

Schmidt M. Automatic Brain Tumor Segmentation. Computing Science. Edmonton: University of Alberta; 2005. p. 161. [p. 44]

Salvat F, Fernández-Varea JM, Acosta E, *et al.* PENELOPE: A code system for Monte Carlo simulation of electron and photon transport. Issy-les-Moulineaux: OECD Nuclear Energy Agency; 2003. [p. 118]

Sheikh-Bagheri D, Rogers DW. Monte Carlo calculation of nine megavoltage photon beam spectra using the BEAM code. *Med Phys* 2002;29:391-402. [p. 122]

Sempau J. PENEASY, a structured main program for PENELOPE, freely available from http://www.upc.es/inte/downloads/penEasy.htm. 2006. [p. 118, 122]

Sempau J, Acosta E, Baro J, Fernández-Varea JM, Salvat F. An algorithm for Monte Carlo simulation of coupled electron-photon transport *Nucl. Instrm. Methods Phys. Res B* 1997;132:377-390. [p. 118]

Sempau J, Fernandez-Varea JM, Acosta E, Salvat F. Experimental benchmarks of the Monte Carlo code PENELOPE. *Nucl. Instrm. Methods Phys. Res B* 2003;207:107-123. [p. 118]

Sempau J. CLONEASY, a library of scripts, freely available from http://www.upc.edu/inte/en/descarregues.php (Barcelona, 2006). [p. 121]

Serago C, Chungbin SJ, Buskirk SJ, Ezzeli GA, Collie AC, Vora SA Initial experience with ultrasound localization for positioning prostate cancer patients for external beam radiotherapy *Int. J. Radiat. Oncol. Biol. Phys.* 2002 53 1130-1138. [p. 2]

Shirato H, et al Four-dimensional treatment planning and fluoroscopic real-time tumor tracking radiotherapy for moving tumor *Int. J. Radiat. Oncol. Biol. Phys.* 2000 48 435-442. [p. 2]

Shuman W, Griffin BR, Haynor DR, Johnson JS, Jones DC, Cromwell LD, Moss AA. MR imaging in radiation therapy planning. *Radiology* 1985;156:143-147. [p. 7]

Sled JG, Zijdenbos A P and Evans A C A nonparametric method for automatic correction of intensity nonuniformity in MRI data. *IEEE Trans. Med. Imag.* 1998;17:87-97. [p. 30, 44]

Stanescu T, Jans H, Fallone BG. Investigation of a 3D MR Distortion Correction Protocol. [Abstract]. *Med Phys* 2006;33:2658. [p. 4, 5, 35, 64, 71, 84]

Stanescu T, Syme A, Pervez N and Fallone B G. MRI-based treatment planning for radiotherapy of brain lesions. [Abstract]. *Med Phys* 2005;32:2033. [p. 4, 34, 70, 73, 75, 83]

Stanescu T, Jans H-S, Stavrev P and Fallone B G. 3T MR-based treatment planning for radiotherapy of brain lesions. *Radiol Oncol* 2006;40:125-132. [p. 4, 34, 70, 73, 75, 83, 85, 95, 101]

Stanescu T, Jans H-S, Stavrev P, Fallone BG. A Complete MR-Based Treatment Planning Procedure for Radiotherapy of Intracranial Lesions. [Abstract]. *Med Phys* 2006;33:2271. [p. 4, 34, 70, 73, 75, 83, 84]

Stanescu T, Jans H, Pervez N, Stavrev P, Fallone BG. Developments in MRI Simulation of Intracranial Lesions. [Abstract]. *Radiother Oncol* 2007;84:S18. [p. 4, 34, 70, 73, 75, 83]

Steciw S, Stanescu T, Carlone M, Fallone B. Magnetic Shielding of a Coupled MRI-Linac System. [Abstract]. *Med Phys* 2007;34:2623. [p. 2, 116, 129]

Stephen M, Jenkinson M, Woolrich MW, Beckmann CF, Behrens TEJ et al. Advances in functional and structural MR image analysis and implementation as FSL. *NeuroImage* 2004;23:208-219. [p. 88]

Stroom J, Heijmen BJ. Geometrical uncertainties, radiotherapy planning margins, and the ICRU-62 report. *Radiother Oncol.* 2002 64:75-83. [p. 2]

Styner M, Brechbuhler C, Szekely G and Gerig G. Parametric Estimate of Intensity Inhomogeneities Applied to MRI. IEEE Trans. Med. Imag. Vol 19; 2000. pp. 153-165. [p. 30, 44]

Sultanem K, Patrocinio H, Lambert C, Corns R, Leblanc R, *et al.* The use of hypofractionated intensity-modulated irradiation in the treatment of glioblastoma multiforme: preliminary results of a prospective trial. *Int J Radiat Oncol Biol Phys* 2004;58:247-252. [p. 34]

Sumanaweera TS, Glover G H, Binford T O and Adler J R. MR susceptibility misregistration correction. IEEE Trans. Med. Imag. Vol 12; 1993. pp. 251-259. [p. 35, 36, 84, 88]

Tanner S, Finnigan DJ, Khoo VS, Mayles P, Dearnaley DP and Leach MO. Radiotherapy planning of the pelvis using distortion corrected MR images: the removal of system distortions. *Phys Med Biol* 2000;45:2117-2132. [p. 34, 36]

Thorton A, Sandler MD, Ten Haken RK, McShan DL, Fraas BA, LaVigne ML, Yanke BR. The clinical utility of magnetic resonance imging in 3-dimensional treatment planning of brain neoplasms. *Int J Radiat Oncol Biol Phys* 1992;24:767-775. [p. 34, 82]

van Herk M. Errors and margins in radiotherapy *Semin. Radiat. Oncol.* 2006;14 52–64. [p. 2]

van Herk M, Remeijer P, Rasch C, Lebesque JV. The probability of correct target dosage: dose-population histograms for deriving treatment margins in radiotherapy. *Int J Radiat Oncol Biol Phys* 2000;47:1121-1135. [p. 2]

Yanez Y, Dempsey JF. Monte Carlo Simulations of Air Cavities in Phantoms Submerged in Magnetic Fields. *Med Phys* 2007;34:2590. [p. 2, 116]

Yin F, Gao Q, Xie H, Nelson D, Yu Y, et al. MR image-guided portal verification for brain treatment field. . *Int J Radiat Oncol Biol Phys* 1998;40:703-711. [p. 4, 86]

Young I, Cox IJ, Bryant DJ, Bydder GM. The benefits of increasing spatial resolution as a means of reducing artifacts due to field inhomogeneities. *Mag Res Imag* 1988;6:585-590. [p. 35]

www.centos.org. [p. 121]

www. comsol.com [p. 148]

www.imphyalloys.com. [p. 159]

www.open-mpi.org. [p. 121]

www.rocksclusters.org. [p. 121]

Wang D, Doddrell D M and Cowin G. A novel phantom and method for comprehensive 3-dimensional measurement and correction of geometric distortion in magnetic resonance imaging. *Mag. Res. Imag.* 2004;22:529-542. [p. 4, 5, 35, 36, 37, 38, 39, 43, 64, 73, 74, 84]

Wang D, Strugnell W, Cowin G, Doddrell D M, Slaughter R. Geometric distortion in clinical MRI systems Part 1: evaluation using a 3D phantom. *Mag Res Imag* 2004;22:1211-1221. [p. 4, 35, 36, 37, 38, 58, 64, 65, 75, 84, 97]

Wang D, Doddrell D M. Method for a detailed measurement of image intensity nonuniformity in magnetic resonance imaging. *Med. Phys.* 2005;32:952-960. [p. 44, 50, 61]

Zawadzki M. MR imaging of the brain. *Radiology* 1988;166:1-10. [p. 2, 4, 82]